



AFRL-RQ-WP-TR-2016-0043

**EXPERIMENTAL STUDY—HIGH ALTITUDE FORCED
CONVECTIVE COOLING OF ELECTROMECHANICAL
ACTUATION SYSTEMS**

Evan M. Racine

University of Dayton Research Institute

**JANUARY 2016
Interim Report**

Approved for public release; distribution unlimited.

See additional restrictions described on inside pages

**AIR FORCE RESEARCH LABORATORY
AEROSPACE SYSTEMS DIRECTORATE
WRIGHT-PATTERSON AIR FORCE BASE, OH 45433-7541
AIR FORCE MATERIEL COMMAND
UNITED STATES AIR FORCE**

NOTICE AND SIGNATURE PAGE

Using Government drawings, specifications, or other data included in this document for any purpose other than Government procurement does not in any way obligate the U.S. Government. The fact that the Government formulated or supplied the drawings, specifications, or other data does not license the holder or any other person or corporation; or convey any rights or permission to manufacture, use, or sell any patented invention that may relate to them.

This report was cleared for public release by the USAF 88th Air Base Wing (88 ABW) Public Affairs Office (PAO) and is available to the general public, including foreign nationals.

Copies may be obtained from the Defense Technical Information Center (DTIC)
(<http://www.dtic.mil>).

AFRL-RQ-WP-TR-2016-0043 HAS BEEN REVIEWED AND IS APPROVED FOR
PUBLICATION IN ACCORDANCE WITH ASSIGNED DISTRIBUTION STATEMENT.

*//Signature//

QUINN H. LELAND
Program Manager
Mechanical and Thermal Systems Branch
Power and Control Division

//Signature//

JOHN F. HOYING, Chief
Mechanical and Thermal Systems Branch
Power and Control Division

This report is published in the interest of scientific and technical information exchange and its publication does not constitute the Government's approval or disapproval of its ideas or findings.

*Disseminated copies will show “//Signature//” stamped or typed above the signature blocks.

REPORT DOCUMENTATION PAGE				Form Approved OMB No. 0704-0188	
<p>The public reporting burden for this collection of information is estimated to average 1 hour per response, including the time for reviewing instructions, searching existing data sources, gathering and maintaining the data needed, and completing and reviewing the collection of information. Send comments regarding this burden estimate or any other aspect of this collection of information, including suggestions for reducing this burden, to Department of Defense, Washington Headquarters Services, Directorate for Information Operations and Reports (0704-0188), 1215 Jefferson Davis Highway, Suite 1204, Arlington, VA 22202-4302. Respondents should be aware that notwithstanding any other provision of law, no person shall be subject to any penalty for failing to comply with a collection of information if it does not display a currently valid OMB control number. PLEASE DO NOT RETURN YOUR FORM TO THE ABOVE ADDRESS.</p>					
1. REPORT DATE (DD-MM-YY) January 2016		2. REPORT TYPE Interim		3. DATES COVERED (From - To) 07 February 2014 – 31 December 2015	
4. TITLE AND SUBTITLE EXPERIMENTAL STUDY—HIGH ALTITUDE FORCED CONVECTIVE COOLING OF ELECTROMECHANICAL ACTUATION SYSTEMS				5a. CONTRACT NUMBER In-house	
				5b. GRANT NUMBER	
				5c. PROGRAM ELEMENT NUMBER 62203F	
6. AUTHOR(S) Evan M. Racine				5d. PROJECT NUMBER 3145	
				5e. TASK NUMBER	
				5f. WORK UNIT NUMBER Q1F4	
7. PERFORMING ORGANIZATION NAME(S) AND ADDRESS(ES) By: University of Dayton Research Institute Energy Technology and Materials Division 300 College Park Dayton, OH 45469-0170 For: Mechanical and Thermal Systems Branch (AFRL/RQQM) Power and Control Division, Air Force Research Laboratory Aerospace Systems Directorate Wright-Patterson Air Force Base, OH 45433-7541 Air Force Materiel Command, United States Air Force				8. PERFORMING ORGANIZATION REPORT NUMBER AFRL-RQ-WP-TR-2016-0043	
9. SPONSORING/MONITORING AGENCY NAME(S) AND ADDRESS(ES) Air Force Research Laboratory Aerospace Systems Directorate Wright-Patterson Air Force Base, OH 45433-7541 Air Force Materiel Command United States Air Force				10. SPONSORING/MONITORING AGENCY ACRONYM(S) AFRL/RQQM	
				11. SPONSORING/MONITORING AGENCY REPORT NUMBER(S) AFRL-RQ-WP-TR-2016-0043	
12. DISTRIBUTION/AVAILABILITY STATEMENT Approved for public release; distribution unlimited.					
13. SUPPLEMENTARY NOTES PA Case Number: 88ABW-2015-5826; Clearance Date: 02 December 2015. This report is a student thesis, with oversight by AFRL project management, in fulfillment of a Masters degree.					
14. ABSTRACT The evaluation of the effects of altitude on forced air convective cooling is studied experimentally. The evolution of the more electric aircraft has led to the adoption of high power electronics for flight critical systems and the need to mitigate their thermal loads. Changes in altitude affect properties that govern heat transfer, such as air pressure, density, and temperature. Current methodology behind heat transfer prediction lacks a comprehensive experimental validation at altitudes above 16,000 feet, relevant to commercial and military aircraft. The convective heat transfer coefficient at altitudes from 0 to 52,000 feet above sea level at sea level room temperature (~24 °C) was measured through the use of a wind tunnel inside a vacuum chamber. Test results, with Reynolds number ranging from 500 to 14,000 and pressure from 0.1 atm to 1.0 atm, confirm that the Nusselt number and pressure loss coefficient are independent of altitude and can be determined from experimental measurement, numerical simulation, and suitable correlations obtained at sea level. Both quantities are functions of Reynolds number only. This experimental investigation will serve to provide a greater confidence for predictive methods of heat transfer at high altitude, which can lead to better optimized thermal management solutions for flight control electromechanical actuation systems.					
15. SUBJECT TERMS electromechanical actuator, EMA, flight control actuation, thermal management					
16. SECURITY CLASSIFICATION OF:			17. LIMITATION OF ABSTRACT: SAR	18. NUMBER OF PAGES 121	19a. NAME OF RESPONSIBLE PERSON (Monitor) Quinn H. Leland 19b. TELEPHONE NUMBER (Include Area Code) N/A
a. REPORT Unclassified	b. ABSTRACT Unclassified	c. THIS PAGE Unclassified			

TABLE OF CONTENTS

LIST OF FIGURES	iii
LIST OF TABLES	v
LIST OF SYMBOLS & ABBREVIATIONS	vi
ACKNOWLEDGEMENTS	viii
CHAPTER 1 INTRODUCTION	1
1.1 Electronics in Aviation	1
1.2 Research Concentration	2
1.3 Purpose.....	5
CHAPTER 2 BACKGROUND	6
2.1 Literature Review.....	6
2.2 Synopsis	9
CHAPTER 3 EXPERIMENT	11
3.1 Design Concept.....	11
3.2 Environmental Chamber	12
3.3 Wind Tunnel Hardware.....	12
3.3.1 Fan	13
3.3.2 Valve	14
3.3.3 Heater/Heat Sink.....	14
3.3.4 DAQ	16
3.4 Wind Tunnel Design	16
3.4.1 Design Integration.....	17
3.4.2 Detailed Design.....	20
3.4.3 Wind Tunnel Section Design	21
3.4.4 Pressure Loss	23
3.5 Test Matrix.....	27
3.6 Experiment Construction	28
3.6.1 Sensors: Types, Usage and Installation	30
3.6.2 Wiring, Power Distribution & Programming.....	36
3.7 Validation and Calibration.....	40
3.7.1 Pressure Sensors.....	40
3.7.2 Thermocouples.....	40
3.7.3 Duct Air Flow Calibration	40
3.7.4 Heater Power.....	43
3.7.5 Steady State Verification	44
3.8 Testing.....	48
CHAPTER 4 EXPERIMENTAL RESULTS AND DISCUSSION	49
4.1 Heat Transfer Coefficient	49
4.1.1 Convective Thermal Energy Calculation	49
4.1.2 Nusselt Number	54
4.1.3 Nusselt Number Flat Plate Correlation	55
4.1.4 Nusselt Number Internal Flow Correlation.....	57
4.2 Pressure Loss	59
4.2.1 Internal Flow Friction Factor Correlation.....	60
4.2.2 Friction Factor Simons Method	62

CHAPTER 5	CONCLUSION AND FUTURE WORK RECOMMENDATION	65
5.1	Conclusion	65
5.2	Future Work Recommendation	65
BIBLIOGRAPHY	67
APPENDICES	69
APPENDIX A	FAN SPEC SHEET	69
APPENDIX B	WIND TUNNEL MINOR LOSS CALCULATIONS	71
APPENDIX C	PRESSURE DROP EXAMPLE.....	78
APPENDIX D	WIRING DIAGRAM.....	79
APPENDIX E	PRESSURE SENSOR CALIBRATION INFO.....	80
APPENDIX F	THERMOCOUPLE CALIBRATION PROCEDURE	85
APPENDIX G	HEAT SINK TEMPERATURE SETTLING TIME.....	88
APPENDIX H	RESULTS UNCERTAINTY ANALYSIS	91

LIST OF FIGURES

Figure 1.1 Aircraft Electric Power Demands over Time [1]	1
Figure 1.2 Aircraft Avionics Heat Load Progression over Time [2]	2
Figure 1.3 Air Pressure, Density, Temperature and Speed of Sound Relative to Altitude. 4	
Figure 2.1 Temperature Rise per Heat Flux vs. Convective HTC [2].	6
Figure 2.2 Summary of Results from Belady [9].	8
Figure 3.1 Conceptual Design of Experimental Test Setup.	11
Figure 3.2 Tenney Versa 3 Environmental Chamber with Working Volume.	12
Figure 3.3 Fan Curve Provided by the Manufacturer of the Propimax 2L	13
Figure 3.4 Heat Sink Photograph (Left) and Profile Dimensions, in Inch (Right)	15
Figure 3.5 Thin Film Heaters Installed on the Base of Heat Sink.	15
Figure 3.6 Design Length Strategy for Duct Air Velocity Measurement [15]	17
Figure 3.7 Wind Tunnel Design, 180° Turn Concept.	19
Figure 3.8 Detailed CAD Model of Wind Tunnel Design.	20
Figure 3.9 Wind Tunnel Sectioned View with Dimensions, in Inch.	21
Figure 3.10 Features Used to Minimize Pressure Loss in Wind Tunnel.	22
Figure 3.11 Fan Curve and System Resistance at 1.0 atm.	24
Figure 3.12 Fan Curve and System Resistance at 0.7 atm.	25
Figure 3.13 Fan Curve and System Resistance at 0.5 atm.	25
Figure 3.14 Fan Curve and System Resistance at 0.2 atm.	26
Figure 3.15 Wind Tunnel inside Environmental Chamber.	29
Figure 3.16 3D Printed Parts within Wind Tunnel	30
Figure 3.17 Mounting Locations of the 4 Differential Sensors.	31
Figure 3.18 Location of Pressure Taps on Heat Sink Housing.	32
Figure 3.19 Heat Sink Base Thermocouple Placement in Inch	33
Figure 3.20 Thermocouple Placement at the Entrance of the Test Section	34
Figure 3.21 Thermocouple Placement at the Center of the Heat Sink.	34
Figure 3.22 Thermocouple Placement at the Exit of the Heat Sink, Section 21	35
Figure 3.23 Fan Thermocouple Placement	36
Figure 3.24 Wire Pass-Through Seal Design.	37
Figure 3.25 Air Flow Control Loop Operational Logic Diagram.	38
Figure 3.26 Wind Tunnel Control Diagram.	39
Figure 3.27 Developing Flow between Two Plates [21].	41
Figure 3.28. Location of Transverse Measurement Points within Duct Cross-Section.	41
Figure 3.29 Air Velocity Correction Curve	42
Figure 3.30 Wire Diagram for Shunt Current Measurement Calibration	43
Figure 3.31 Shunt Current Calibration Regression Curve	44
Figure 3.32 Temperature Measurements for Settling Time.	46
Figure 4.1 Thermal Energy Conduction Losses	50
Figure 4.2 Heat Sink Radiation Surfaces	53
Figure 4.3 Nusselt Number vs. Reynolds Number at Various Altitude Pressure	54
Figure 4.4 Comparison of the Nusselt Number of Flat Plate Correlation vs Test Data ...	56
Figure 4.5 Local Nusselt Number Thermal Development [18]	57
Figure 4.6 Comparison of the Average Nusselt Number and Internal Flow Correlations	59
Figure 4.7. Comparison of the Pressure Loss Coefficient at Different Pressure	60
Figure 4.8 Comparison of the Pressure Loss Coefficient: Measurement vs Correlation. .	62

Figure 4.9 Comparison of the Pressure Loss Coefficient for the Simons Method	64
Figure B. 1 Wind Tunnel Diffuser Section [19]	72
Figure B. 2 Wind Tunnel Contraction Section [19].....	73
Figure B. 3 Expanding Corner; Constant Diameter Corner; Expanding Corner	74
Figure B. 4 Concept Design, Expanding Corner with Turning Vanes.	74
Figure B. 5 Geometry of guide vanes to a 90° expanding corner [23]	75
Figure B. 6 Constant Diameter Corner Loss Coefficient Estimation [24].....	76
Figure B. 7 Flow Straighter Sizing [15].....	77
Figure F. 1 Thermocouple Test Setup.....	85
Figure F. 2 Thermocouple Calibration Results.....	86

LIST OF TABLES

Table 3-1 Critical Requirements for Duct Length	19
Table 3-2 Values for the Intersection Points of the Fan Curves and System Resistance .	26
Table 3-3 Preliminary Test Matrix for Desired Airflow Conditions	28
Table 3-4 Thermocouple Numbering.....	32
Table 3-5 Results from Linear Fit of Shunt Calibration	44
Table 3-6 Temperature Measurements for Settling Time.....	46
Table 3-7 Comparison of the Temperature Difference for Extended Time Testing.....	47
Table 4-1 Thermal Resistance Calculation for Housing Side.....	52
Table 4-2 Thermal Resistance Calculation for Housing Bottom.....	52
Table F - 1 Thermocouple Regression Analysis.....	87
Table H - 1 Measurement Uncertainty.....	92
Table H - 2 Experimental Results and Uncertainty	108

LIST OF SYMBOLS & ABBREVIATIONS

3D	Three Dimensional
1D	One Dimensional
AC	Alternating Current
AL	Aluminum
AMCA	Air Movement and Control Association
ASL	Above Mean Sea Level
AVG	Average
CAD	Computer Aided Design
COTS	Commercial Off-The-Shelf
cRIO	Compact Reconfigurable I/O Module
DAQ	Data Acquisition
DC	Direct Current
ECS	Environmental Control System
EMA	Electromechanical Actuator
EMAS	Electromechanical Actuator System
FPGA	Field-Programmable Gate Array
HTC	Heat Transfer Coefficient
I/O	Input/Output
inH ₂ O	Inches of Water (inches of H ₂ O)
INWC	Inches of Water Column (inches of H ₂ O)
LabVIEW	Laboratory Virtual Instrumentation Engineering Workbench
NASA	National Aeronautics and Space Administration
NI	National Instruments
PC	Polycarbonate
PCM	Phase Change Material
PID	Proportional, Integral, Derivative
PS	Power Supply
PSI	Pounds per Square Inch
PSIA	Pounds per Square Inch Absolute
RPM	Rotations per Minute
RT	Real-Time
RTD	Resistive Temperature Detector
RTV	Room Temperature Vulcanization
SD	Standard Deviation
sps	Samples per Second
TC	Thermocouple
TMS	Thermal Management System
VDC	Volts Direct Current
VI	Virtual Instrument
%FS	Percent of Full Scale
ΔT	Temperature Difference, K
A	Area, m^2
C, c	Constant
D_H	Hydraulic Diameter, in. or m
f	Friction Coefficient

h	Convective Heat Transfer Coefficient, W/m ² -K
h_c	Conductance, W/m ² -K
I	Electrical Current, Amps
k	Thermal Conductivity W/m-K
L	Length, in. or m
L^*	Characteristic Length (\sqrt{Area}), in. or m
N	Quantity (Number of)
Nu	Nusselt Number
P	Electrical Power, W
p	Pressure, Pa, psi, atm or inH ₂ O
Pr	Prandtl Number
Q	Thermal Energy, W
\mathcal{R}	Gas Constant
R_e	Electrical Resistance, Ω
Re	Reynolds Number
Re_D	Reynolds Number from Hydraulic Diameter
Re_L	Reynolds Number from Length
R_t	Thermal Resistance, K/W
U	Velocity, m/s
V	Electrical Voltage, V
ϵ	Efficiency
η	Pressure loss Coefficient
μ	Dynamic Viscosity, kg/m-s
ν	Kinematic Viscosity, m ² /s
ρ	Density, kg/m ³
σ	Stefan-Boltzmann Constant, Uncertainty

ACKNOWLEDGEMENTS

The completion of my master's thesis has required a lot of hard work. However, it would not have been possible without the support and guidance of advisors, coworkers, friends, and family. I would like to take the time to thank those individuals.

I would first like to thank my family for always supporting me with my pursuits in my professional and educational careers. Without their advice and support I would not have been able to reach goals that I have.

Next, I would like to thank my advisor Quinn Leland who provided me with the opportunity of a research assistantship through the Air Force Research Laboratory and whose valuable guidance led to the success of this project. I would like to thank Louis Chow from University of Central Florida. Without his technical expertise and guidance this project would not have been possible. I would also like to thank my advisor Jamie Ervin who originally referred me to the opportunity at the AFRL and who has been very helpful with the completion of this work.

I would also like to thank all the individuals from the UDRI, AFRL and UCF who contributed advise, support and guidance along the journey of this thesis; my supervisor Bang Tsao from the University of Dayton Research Institute, as well as my other colleagues from UDRI, Steve Fuchs, John Murphy and Street Barnett. I would like to thank my interns, Paul Fuchs and Zach Adamson who were instrumental with construction and testing of this experiment. My gratitude also goes to Yeong-Ren Lin from UCF who provided valuable insight into designing this experiment. I would also like to thank Justin Delmar and Mike Bruggeman from the AFRL who each uniquely contributed to help complete this experiment.

Lastly, I would like to thank the United States Air Force and AFRL who made this work possible through a complete funding of the project under the contract FA8650-12-D-2224-0002.

CHAPTER 1

INTRODUCTION

1.1 Electronics in Aviation

Since the 1930's aircraft of all varieties began adopting systems that required electrical power for their operation [1]. Over the decades, this trend has only increased. From avionics and flight control to environmental control, electronic systems have grown and evolved into more important and mission critical roles. As modern aircraft become more reliant on electronic systems, a greater burden is being placed on the electric power generation to operate these systems. The power demands are being met with larger and more powerful electrical generation systems, further enabling the capability of on board electronics. However, with higher power demands, the thermal load created by the sum of these systems has been increasing proportionately.

Figure 1.1 [1] and Figure 1.2 [2] show the increasing electrical demands and subsequent rise in the aircraft heat load. Traditionally the primary sink for thermal energy on an aircraft is the on board fuel. However, only a finite amount of energy can be stored this way and modern aircraft are quickly approaching this limit. Additionally, the incorporation of structural composite materials of low thermal conductivity and emissivity has created the adverse secondary effect of insulating the aircraft. Altogether, these effects have forced a greater burden on thermal management systems (TMS).

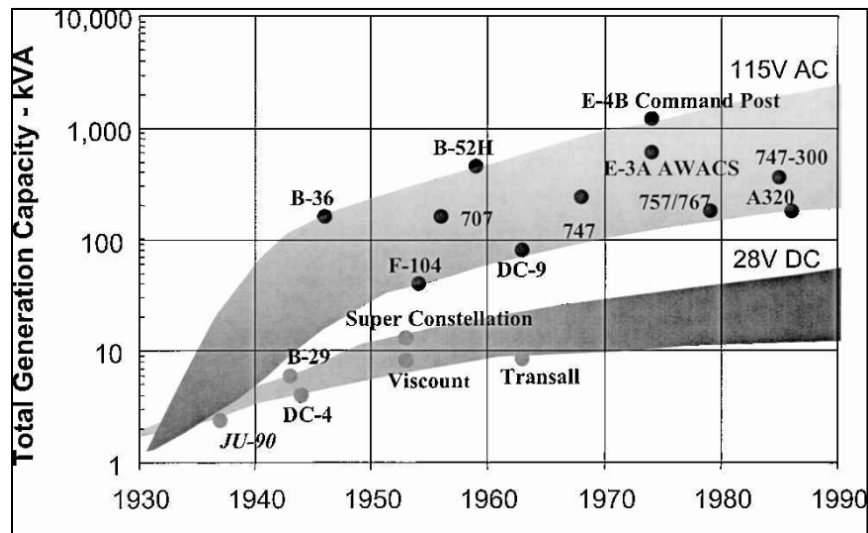


Figure 1.1 Aircraft Electric Power Demands over Time [1]

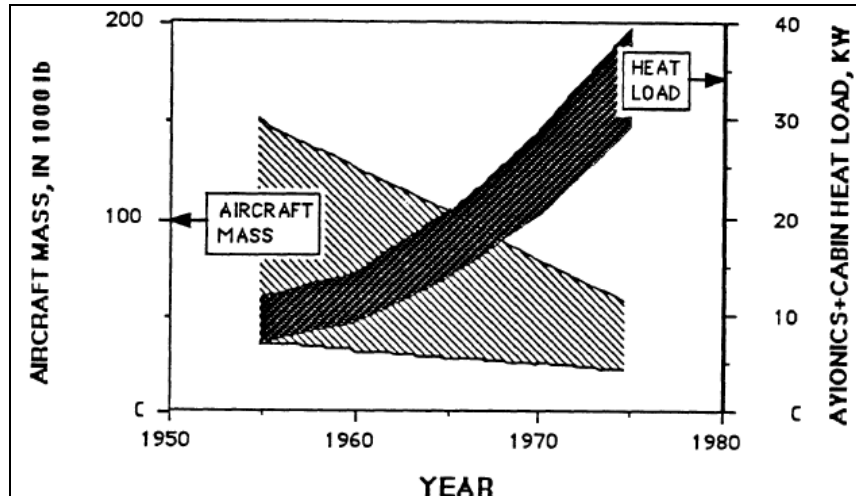


Figure 1.2 Aircraft Avionics Heat Load Progression over Time [2]

The majority of the TMS developed have mainly focused on moving and distributing the heat loads away from critical components. However, this approach is limited. Modern aircraft electronics are also continually becoming lighter and more compact, thus increasing the power density. This means that thermal management will need to be more efficient in removing large transient heat loads and need to be collocated with the heat source. “5th generation aircraft have 3-5 times the heat load of legacy platforms while being limited in their ability to reject heat to the environment.” [3]

1.2 Research Concentration

A relatively new challenge for thermal management that is emerging has to do with the presence of electromechanical actuation systems (EMAS) being developed for aircraft primary flight control surfaces. The emergence of EMAS has brought about measurable advantages in weight savings, maintainability, complexity, and efficiency. However, they are not without drawbacks. Prior solutions for flight control actuation used hydraulic actuators. One of the advantages these systems had over current proposed EMAS replacement was the presence of hydraulic fluid acting secondarily as a coolant. The removal of hydraulic actuation systems in favor of EMAS means the removal of its very effective thermal management process, thus creating a new challenge [4] [5] [6].

Some specific solutions considered for the thermal management of EMAS incorporate the following:

- Thermal energy storage (on aircraft)
 - Phase Change Material (PCM) for transient heat absorption
 - Heat pipe, loop heat pipe, or other high conductive materials to conduct the heat from PCM to airframe or fuel
- Thermal energy removal (to ambient)
 - Convection, air jet cooling

- Convection, liquid to air heat exchanger
- Convection, air cooling with fan

Each of these methods has advantages and disadvantages, whether it is performance, integration, or cost.

In this study, the suitability of forced convection with air will be examined. Forced convection is a very common and effective method used for thermal management, particularly in cooling electronic equipment. There exist multiple approaches to accomplish forced convection cooling using air. One common approach is to use an enhanced surface or heat exchanger to remove the thermal energy away from critical components and convect it to an airstream. The most common source of the air flow would be an electric fan due to its low cost, light weight, small size, and low energy consumption. However, on an aircraft there exist other sources, such as: the aircraft environmental control system (ECS) air, engine bypass air, or channeling external air passing over the aircraft surface (ram air). Although, all methods have considerable systematic differences, they all involve transmission of thermal energy to the atmosphere surrounding the aircraft. Therefore, an investigation into properties governing this process will be applicable to all similar solutions.

For the case of the electromechanical actuation systems for flight control, the electromechanical actuator (EMA) will be housed in what are known as wing bays, unpressurized enclosures that are isolated from the ECS air flow but exposed to changes in the atmospheric conditions. In other words, for most aircraft the internal conditions of components within a wing bay will be static air resembling the environmental conditions of the atmosphere for a given altitude. Physical characteristics of the atmosphere vary relative to altitude (e.g., temperature, pressure, humidity, vapor pressure, speed of sound, concentration of gases, etc.). These properties likely have a drastic effect on the performance of forced convective heat transfer when trying to dissipate thermal energy to the atmosphere.

Figure 1.3 [7] [8] shows the physical characteristics of atmospheric air for altitudes from sea level to 100 km. The right side of the chart shows the different layers of the atmosphere as well as representative altitudes of various man-made aircraft and natural occurring phenomena. Figure 1.3 also shows that a typical flight ceiling for commercial and military air breathing aircraft is about 40,000 feet (12km) above mean sea level (ASL).

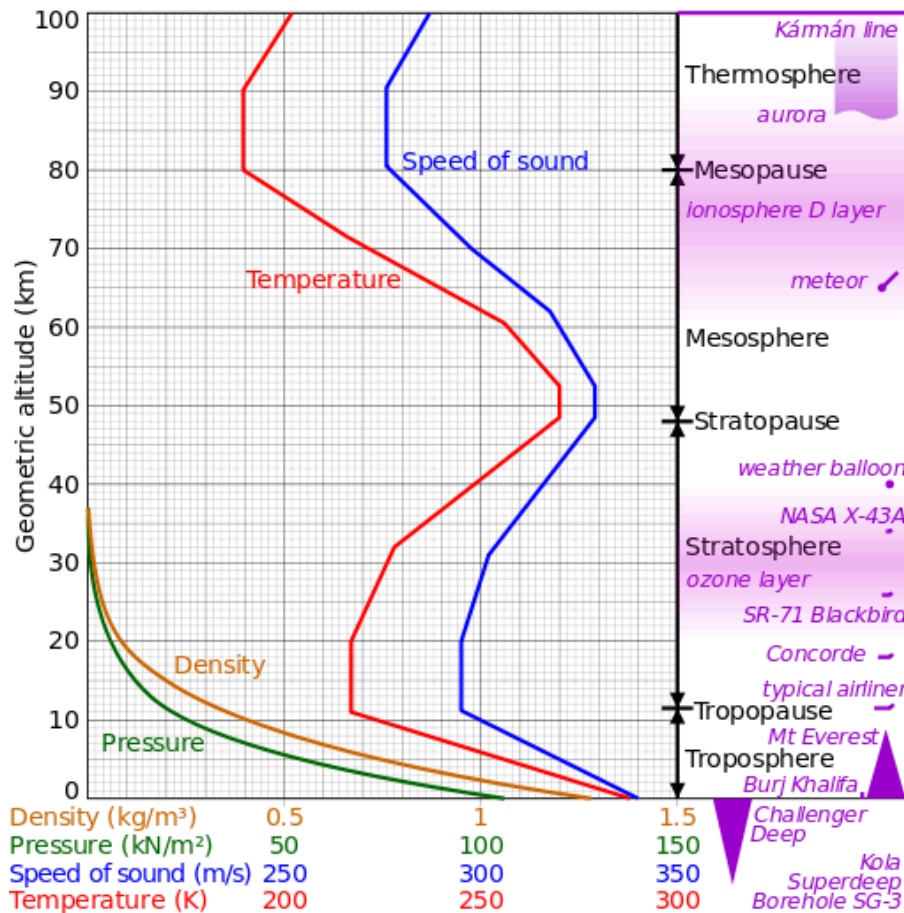


Figure 1.3 Air Pressure, Density, Temperature and Speed of Sound Relative to Altitude [7]
[8]

Of the four properties shown in Figure 1.3 (pressure, density, temperature, and speed of sound), three are interconnected through the ideal gas law, ($PV = nRT$) and can significantly influence heat transfer. Changes to ambient temperature will mostly affect the temperature gradient between the sources to the sink. The changes to this property can be studied and characterized through experimentation at sea level. However, this is not the case for changes to the pressure and density. Although, changes to density and pressure are well understood analytically, there lacks experimental data to support this understanding as it applies to predictive methods of cooling for EMAS. From sea level to 40,000 feet the pressure and density of the air decrease by roughly 80%. The effects this can have on the performance of convective heat transfer could be profound.

When designing forced convective heat transfer solutions for all varieties of systems engineers use several methods for predicting the performance of the designs. Through observation, theoretical analysis, and experimentation, certain relationships have been developed describing the processes of convective heat transfer. These relationships have been quantified as correlations. These correlations can be used to describe such characteristics as the heat transfer coefficient (HTC) and friction factor, which are both important theoretical properties when defining the processes of heat and mass transfer.

Correlations that would be relevant to heat transfer performance for electromechanical actuator (EMA) TMS have been developed, supported in theory, and observed experimentally. However, they have not been extensively vetted in atmospheric conditions experienced by commercial and tactical military aircraft.

1.3 Purpose

The purpose of this thesis was to experimentally find the forced convection heat transfer coefficient and pressure drop relationships in a low pressure environment under varying conditions of pressure and velocity, to study methods of heat transfer enhancement, and to validate experimentally existing heat transfer and pressure drop correlations relevant to EMAS cooling at low pressure.

CHAPTER 2 BACKGROUND

2.1 Literature Review

In order to begin planning the experimental investigation into the topic of forced convective heat transfer at high altitude, a comprehensive understanding of relevant publications must first be established. There has been a gap in published experimental evidence regarding high altitude (40,000 feet above mean sea level (ASL)), low Reynolds number convective heat transfer, relevant to the thermal management of electronic systems. However, that is not to say that there is no supporting literature related to this topic at altitudes greater than sea level.

The literature review on the works in this field begins in the late 1980's from an investigation into heat transfer process of electronics at high altitude. In 1989, Bar-Shalom published a thesis titled *Altitude Effects on Heat Transfer Processes in Aircraft Electronic Equipment Cooling* [2]. This work took an analytical approach to characterizing the changes in environment conditions and their impact on cooling electronics in wing bays. It also took steps to detail the contributing factors and issues for heat transfer processes throughout a range of altitude from 0 - 70,000 feet ASL and offered insight on how to optimize cooling for these conditions. One conclusion of this study was when considering only pressure changes, the heat transfer thermal resistance increases exponentially with increasing altitude. This is due to a reduced heat transfer coefficient (HTC) at low pressures. With a lower HTC, the temperature difference between the source and fluid becomes larger as a result of the higher thermal resistance. Figure 2.1 [2] shows the relationship that the decreasing convective HTC has with the temperature rise between the electronics and ambient, with changing altitude.

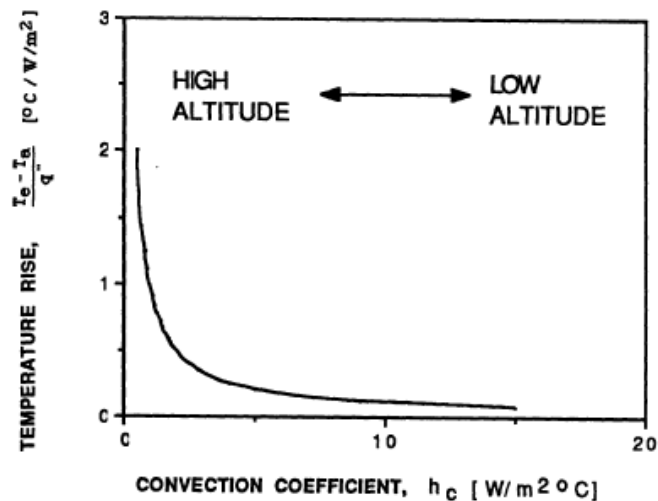


Figure 2.1 Temperature Rise per Heat Flux vs. Convective HTC [2].

With a lower HTC the electronics will have a higher operating temperature since it requires a higher temperature difference to remove the same amount of heat. This drives system requirements for electronics cooling, since having a higher temperature difference means that the electronics are operating closer to unsafe temperatures. This becomes a key element in aircraft electronic TMSs, which can minimize the working temperature of components at altitude by designing systems to have the largest possible HTC.

Another important point from Bar-Shalom's work was regarding the contribution of radiation to the thermal management process at high altitude. Before this study the practice was to ignore radiation heat transfer. However, with the diminished HTC at altitude, the temperature of the heat source or the electronics increases and the effect of radiation becomes a larger percentage of the overall heat transfer. Further, this thesis suggested ways to design optimal cooling methods, but it falls short with regard to experimental evidence to support its conclusions.

Belady [9] sought to provide an overview on the impact altitude has on the fan cooling of electronics. The majority of thermal management solutions for electronics favors the use of electronic fans to provide fluid motion. This is because they have low cost and weight, reasonable reliability, and are relatively efficient. Performance of the fan is also affected by changes in air pressure and density. Therefore, when studying fan cooling above mean sea level (ASL) this factor must be accounted for. Belady found that at 10,000 feet ASL a fan rotating at the same speed produces a decreased dynamic head that is proportional to the decrease in air density, while the power consumed by the fan is found to be 1/3 less. In other words, the ability of a constant volume axial fan to drive a pressure head decreases due to the air having a lower density. This exacerbate the effect on thermal management due to the influence density has on the heat transfer coefficient in both laminar and turbulent flow conditions. Another observation made by Belady is that from sea level to 10,000 feet ASL the temperature rise in the air exiting the heat sink increased by 50%. This is an indication of the heat sink surface temperature rising, as there are fewer air molecules to remove the heat, resulting in a higher average temperature of the air. This is a direct result of the negative impact low density air has on the heat transfer coefficient. Belady uses the following basic and well established correlations to obtain results. Equation 2-1 [9] and Equation 2-2 [9] are the Nusselt number correlations Belady used for both laminar and turbulent flow regimes.

Equation 2-1 [9]

$$Nu_{Laminar} = C_{hl}; \quad Re < 2,000$$

Equation 2-2 [9]

$$Nu_{Turbulent} = 0.023Re^{0.8}Pr^{0.4}; \quad Re > 10,000$$

where C_{hl} is a constant.

In summary Belady found:

- “For laminar flow, pressure drop is independent of altitude and is a linear function of volumetric flow. Thus, the system impedance curve is the same for all altitudes” [9].
- “For laminar flow, the heat transfer coefficient is independent of altitude and volumetric flow. It is constant for a given geometry as long as the flow is laminar. This implies that the temperature rise to the local air temperature is also constant” [9].
- “For turbulent flow, pressure drop is a function of altitude and the square of the volumetric flow. Thus, the system impedance curve decreases by the density ratio as the altitude increases” [9].
- “For turbulent flow, the heat transfer coefficient is a function of density and volumetric flow both to the 0.8 power for circular ducts. This implies that the local air temperature rise is inversely proportional to density and volumetric flow both to the 0.8 power” [9].

Belady also produced a table (See Figure 2.2) expressing the behavioral changes of the axial fan as well as the heat transfer over a heat sink in relation to changes in altitude, or density.

Description	Parameter	Relation
Fan Performance	Fan Air Flow	$\Delta P \propto \rho$
	Fan Power	$HP \propto \rho$
Heat Capacity	Temperature Rise	$\Delta T \propto 1/(\rho G)$
Laminar Flow	Pressure Drop	$\Delta P \propto G$
	Heat Transfer Coeff	$h = \text{constant}$
Turbulent Flow	Temperature Delta	$\Delta T = \text{constant}$
	Pressure Drop	$\Delta P \propto \rho G^2$
	Heat Transfer Coeff	$h \propto \rho^{0.8} G^{0.8}$
	Temperature Delta	$\Delta T \propto 1/\rho^{0.8} G^{0.8}$

Figure 2.2 Summary of Results from Belady [9]

Belady’s investigation supports the applicability of current methods used to predict the heat transfer coefficient and pressure drop at altitudes from sea level to 10,000 feet ASL. However, there is a significant difference between 10,000 and 40,000 feet ASL. The ambient air used in Belady’s experiment never fell below 67% of atmosphere while modern aircraft operate closer to 20% atmosphere and in some cases lower. This margin is too great to ignore.

In 1999, Wong [10] [11] conducted an experiment on the effects of altitude on electronics cooling performance. The difference from Belady’s study is that Wong managed to gather experimental data by simulating altitudes from 0 – 16,400 feet ASL (5

km). At 16,400 feet ASL the atmospheric pressure is 53% of that at sea level. This is closer to the 20% conditions, or 40,000 feet MLS, but still falls short. Wong's conclusions were meant to aid in the TMS design for specific electronics operating at high altitudes. However, there were still some good takeaways from this study that apply to the use of analytical methods for predicting heat transfer. The primary conclusions gave support for two methods of predicting heat transfer performance, the superposition principle for predicting the surface temperature of a flat plate heater array and the thermal wake function of a flat plate. This approach was better suited for the prediction of surface temperatures based on a reference temperature, rather than explicit prediction of the HTC. Although, it did offer some insight into how heat transfer is influenced by altitude. For instance, Wong confirmed that the steady state surface temperatures at higher altitudes have a much higher value than they would at sea level, given constant velocity air flows and that this effect is more prevalent at higher airspeeds. Overall, this experiment falls short in completing a direct comparison of the changes in the heat transfer coefficient due to altitude.

Xu [12] explored ability of using correction factors to predict forced convective heat transfer at high altitude, the non-dimensional pressure drop and thermal resistance. Xu created correction factors derived from non-dimensional heat transfer and fluid flow parameters (i.e. Reynolds number) to predict the change in performance of a complex processor cooling geometry at an altitude of 3,000 meters (9,800 feet) ASL. The advantage of this approach was that it produced a more general use method for approximating the HTC for any flat plate geometry and flow regime. The results of this experiment support the use of analytical methods for predicting heat transfer and pressure drop, to 0.7 atm (9,800 feet ASL).

One industrial report done by EPAC Software Inc. [13] explored fan cooling at altitudes higher than 16,400 feet ASL. They sought to improve their model for predicting the performance of an aircraft ECU at altitudes up to 80,000 feet ASL. The investigation was launched when EPAC found a large discrepancy in the predicted temperatures of the ECU coldplate at altitudes above 30,000 feet ASL. The method of predicting the temperature was based on a proprietary software setup for their specific application. However, the study revealed the problem to be primarily with the performance of the fan. It was found that the method for predicting dynamic pressure head of a fan cannot be used above 30,000 feet ASL due to a disconnection that happens where constant volumetric flow rate (VFR) is no longer proportional to rotational speed. Instead, a mass flow rate approach must be used. This study provides valuable insight into the field but also serves to raise more questions about the validity of some very standard methods of predicting fan cooling in high altitude conditions, such as the validity of fan impedance curves.

2.2 Synopsis

The results of the literature review uncovered a gap in experimental evidence supporting analytical methods and empirical correlations of predicting convective fan cooling performance relevant to the thermal management of EMAS, at altitudes above 16,000 feet ASL. Further, the review also conveyed the importance of having an accurate

and validated theoretical approach to predicting heat transfer in the low pressure environment. At altitudes up to and above 40,000 feet ASL the lower density air has a significant impact on the performance of both fan performance and the convective heat transfer cooling. This, in addition to the industry thrust to adopt more high power electronics for mission critical systems, drives the need to conduct further research into validating current methods of heat transfer prediction at high altitude. The implication of providing some insight into this research area would be to further advance the understanding of high altitude convective cooling systems. This could be in the form of validating the applicability of existing methods at higher altitude, offering a better analytical approach, such as a new or enhanced correlation, or providing insight for better optimized system elements, such as heat sink or fan design.

CHAPTER 3 EXPERIMENT

3.1 Design Concept

To study forced convective heat transfer at high altitude conditions an experiment needed to be constructed that allows for the control of properties of convective heat transfer (air velocity and temperature difference) as well as the environment in which it occurs (atmospheric pressure). It was determined that the best means to accomplish this was through the construction of an open loop wind tunnel, with a fan driving the flow at the beginning of the tunnel and a heater/heat sink at the end of the tunnel before the exit. A high speed fan was used to drive the airflow within the wind tunnel and allowing for a wide range of Reynolds number within the test section. Airflow was measured using a differential pressure sensor and Pitot tube within the duct channel. Lastly the wind tunnel was placed within an environmental chamber to simulate the conditions of high altitude. Figure 3.1 shows a conceptual diagram of the layout for the open loop wind tunnel.

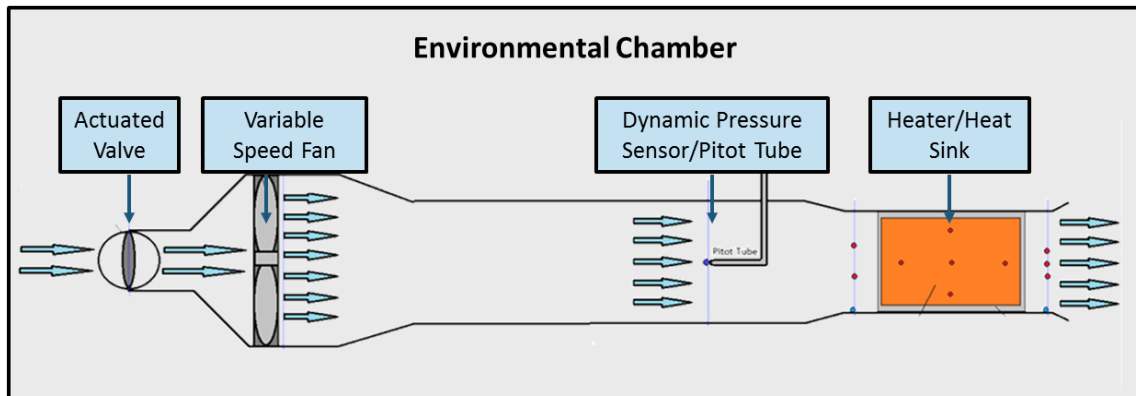


Figure 3.1 Conceptual Design of Experimental Test Setup

To give greater control over the flow, a ball valve was placed at the entrance of the wind tunnel to provide a means to restrict flow thus allowing for control of the velocity. The heat sink was attached to a heater that would provide thermal energy that was transferred to the fluid. Measurements for the accurate characterization of this process such as temperature, absolute, dynamic and static pressures and power dissipation were taken.

Since the experiment sought to study forced convection at high altitude, a means was obtained to lower the ambient pressure in which this open loop wind tunnel operates. The primary atmospheric difference concerning the forced convective heat transfer coefficient from sea level to 50,000 feet ASL is the density of air. Temperature is also a key difference within this altitude range, but it does not affect the HTC. Therefore, the objective would be to obtain a means to lower the air density through the control of ambient pressure. This was achieved by obtaining an environmental chamber. The chamber contains an airtight space that utilizes a vacuum pump to decrease the internal pressure, simulating atmospheric conditions at altitudes above sea level.

3.2 Environmental Chamber

For the purpose of simulating atmospheric conditions above sea level, a Tenney Versa 3 environmental chamber was obtained. The chamber, originally built in the 1950's, was designed to control pressure and temperature for a rectangular volume of 21" x 21" and 25" in height. Figure 3.2 shows the outside of the chamber as well as the sealed workspace available within.



Figure 3.2 Tenney Versa 3 Environmental Chamber (Left) with Working Volume (Right).

The chamber was recently equipped with an updated control unit for active control of chamber pressure and temperature. The pressure is reduced via a rotary vane vacuum pump powered by an electronic motor. The pump itself can achieve a vacuum of about 0.080 TORR (211,000 feet ASL). However, due to imperfect sealing of the chamber the maximum vacuum that was measured to be about 100 TORR and later 80 TORR (52,000 feet ASL) was achieved through the addition of a secondary vacuum pump. The heating and cooling of the air within the chamber is done with an electric coil heater and vapor-compression cycle refrigeration system. Although these systems were available, temperature control was not used for this experiment. The primary reason was negative effect that the refrigeration system had on the absolute pressure control, by causing (± 0.2 PSI) fluctuations during operation. Secondly, there was also little value in varying the chamber's temperature since the HTC measurement is independent of the temperature gradient between the heat sink and ambient air temperature.

3.3 Wind Tunnel Hardware

The four major components responsible for the execution of the experiment are the fan, valve, heater/heat sink, and data acquisition (DAQ) System. The design and use of all four will be discussed in detail within this section.

3.3.1 Fan

The Fan that was chosen is an AMETEK Rotron Propimax 2L 3715SF. This is a very high performance axial fan about 3.0 inches in diameter capable of spinning in excess of 25,000 RPM. This fan proves to be a good fit for the experiment because of its compact size and high volumetric flow rate. The fan is powered by a DC brushless motor that rotates a 2-blade cast aluminum rotor. The fan requires a DC voltage between 10-28 VDC to operate and will draw 1.3 Amps (at 28VDC) while driving air at 1.202 kg/m^3 . However, this power draw will decrease as the density of air being driven decreases [14]. The fan will not run at voltages lower than $\sim 10\text{VDC}$ as this appears to be a minimum threshold voltage needed to drive the motor and electronics. This also means that there is a minimum flow rate that the fan can reach when airflow is being controlled with fan voltage. This is the reason a control valve was also for controlling the airflow. For more information on the Propimax 2L fan, a data sheet is available in APPENDIX A.

A fan curve is a metric for evaluating the performance of any given fan against various loads. Figure 3.3 shows the fan curve for the Propimax 2L 3715SF as provided by the manufacturer. This shows for a given voltage input the fan will drive a certain volume of air of 0-60 liters per second against a static pressure load of 0-4 inches of water (inH₂O). Therefore, to determine the airflow that this fan will produce in a given system the pressure drop of this system must be determined.

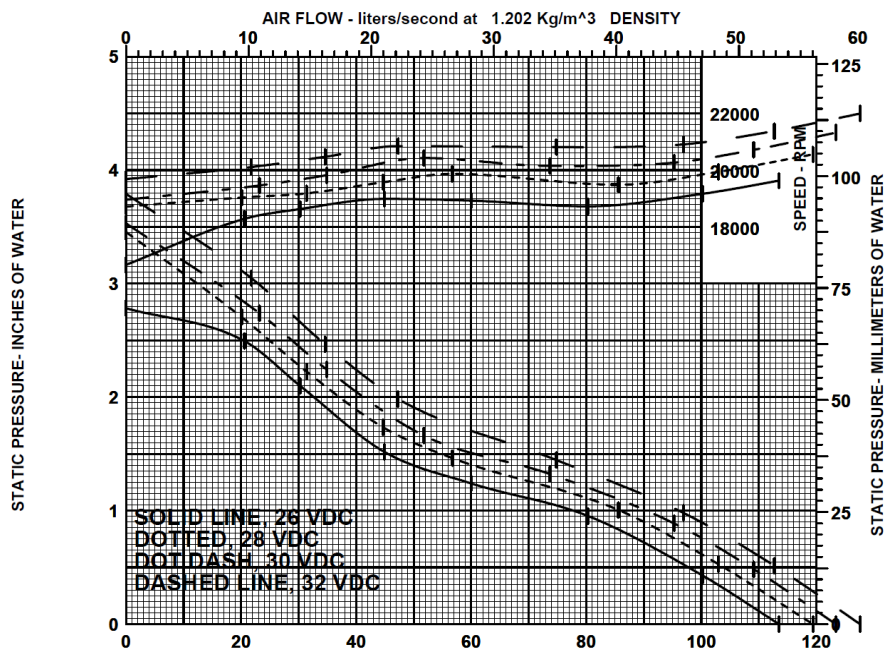


Figure 3.3 Fan Curve Provided by the Manufacturer of the Propimax 2L

The fan curve in Figure 3.3 shows the performance of the fan at an air density of 1.202 kg/m^3 . Since this experiment would operate at reduced densities of air, the amount of pressure the fan can drive would also be reduced. Therefore, in order to accurately characterize the fans capability at low densities, fan curves were needed for its operation

at reduced pressure. Work done by Lin [14], at the University of Central Florida, directly contributed to characterizing this fan at reduced pressures. Lin gathered experimental data on the performance of the Propimax 2L fan and constructed fan curves for pressures at 1.0 atm, 0.7 atm, 0.5 atm and 0.2 atm. The plots from this work can be seen in Section 3.4.4.

3.3.2 Valve

In this experiment a ball valve is used to control the airflow entering the open loop wind tunnel. The valve works as a sphere or ball with a cylindrical hole through it rotates. The cylindrical hole allows for the passage of fluid from one side of the valve to the other. As the valve rotates from 0-90° this cylindrical hole rotates into the side of the valve partially covering it and effectively changing the size of the hole that fluid can now pass from one side of the valve to the other. By decreasing this orifice size the impedance to the system is increased, thus decreasing the volumetric flow rate (VFR). This allows for active modulation of the airspeed with the valve.

Another requirement for this system is that it must be remotely operated. This is because the regulation of airflow will need to be done actively and the experiment will be completely contained inside the environmental chamber. Therefore, an electronically controlled valve must be used. The Plast-O-Matic 2-Way electronically actuated ball valve was selected for this purpose. There are several types of ball valve available for this product line. A ball valve was chosen that fit a 3.0 inch diameter pipe coupling and had 1.0 inch diameter inner orifice size. The actuator that controlled the valve was powered by 19 VDC and responded to an analog signal of 0-10 VDC for position control of 0° (closed) to 90° (fully open).

3.3.3 Heater/Heat Sink

The heater/heat sink would provide the source for the thermal energy generation as well as the geometry dissipating the thermal energy to the fluid stream. The purpose of this experiment required that the geometry used as the heat sink should be able to be characterized using widely accepted methods of correlation. Additionally, it should be a variation of an existing geometry type that is widely adopted within industry, so as to keep its applicability to what might be used to cool EMAS. Therefore, a parallel plate sink was chosen. This type of heat sink is very popular in forced air cooling of electronics because of its good performance and low cost. The other constraint on the geometry is the size. Larger geometries will limit the maximum airflow velocity over the heat sink, thus limiting the range of Reynolds number, as well as making the integration into the experiment more cumbersome given the finite amount of space within the environmental chamber. However, a smaller geometry is more adversely affected by error due to experimental measurement methods, such as thermocouples imbedded altering the thermal conduction and obstructions within the air stream such as thermocouple (TC) probes and a Pitot tube.

Figure 3.4 shows the heat sink that was chosen for the experiment. It was manufactured by Heat Sink U.S.A. It is a 4.0 inch long parallel plate extruded aluminum

heat sink. The material is 6063-T5 unfinished aluminum ($k = 209 \text{ W/m-K}$, $\epsilon = 0.04\text{-}0.07$). Its width is 1.813 in. and height 1.25 in. with a total of 6 fins. This geometry offered a good fit given the scale of the experiment.

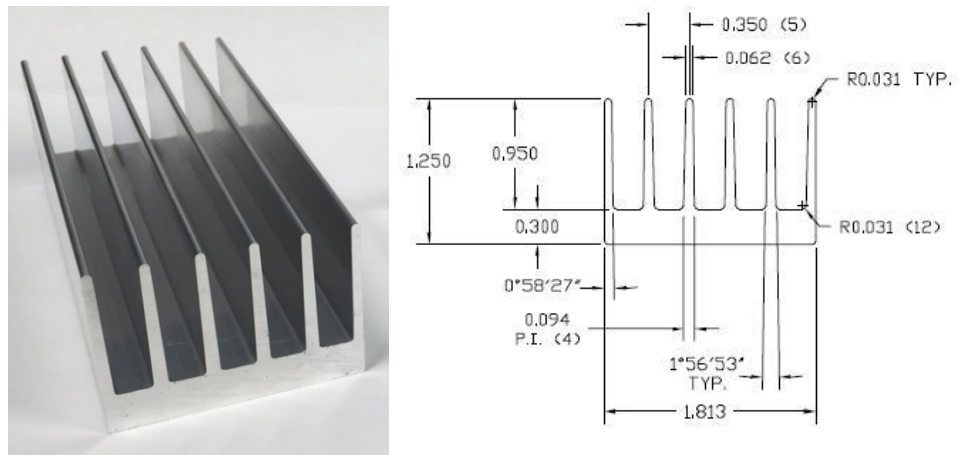


Figure 3.4 Heat Sink Photograph (Left) and Profile Dimensions, in Inch (Right)

A thin film resistive heater was permanently attached to the base of the heat sink. The type chosen was an etched foil sandwiched between two layers of Polyimide film. The entire element is 0.01 in. thick. This would allow for easy integration and attachment to the bottom of the heat sink, as seen in Figure 3.5. In order to have equal heating of the heat sink over the entire area of the base, the heating element must cover the entire 1.813 in. \times 4.0 in. surface of the base. This requires two identical heaters each 2.0 in. \times 2.0 in.

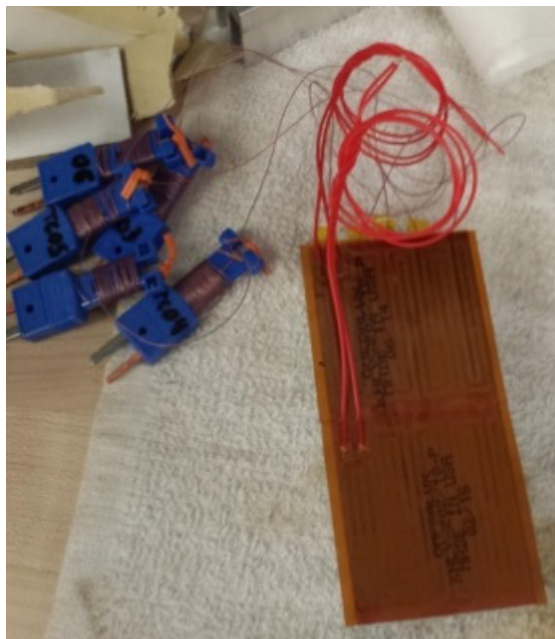


Figure 3.5 Thin Film Heaters Installed on the Base of Heat Sink.

The thin film heater was manufactured by Omega, KMLV-202/10-P. This item had a watt density of 10W/in^2 at 28 VDC and total power output of 40W each, yielding a heat input range of 0-80W. Also, this heater comes with pressure sensitive adhesive on the flat side of the element for ease of attachment to another flat surface. Ultimately the heaters will be wired in parallel so that they both have an equal amount of voltage dropped across their resistive element.

3.3.4 DAQ

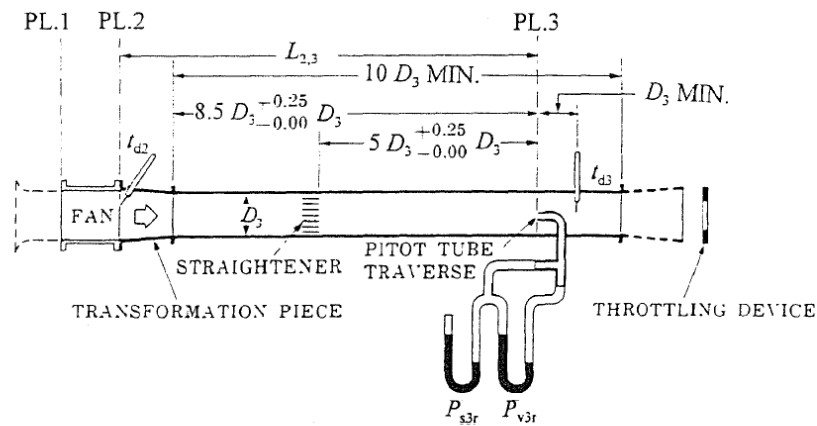
The last critical piece of hardware needed for the setup was the data acquisition system (DAQ). This item would serve as the primary means of control for the experiment as well as being responsible for logging all of the experimental data. The device chosen to do this is a National Instruments (NI) Compact Reconfigurable I/O Module (cRIO). The cRIO-9022 chassis offered the capability of both a real-time (RT) controller and field-programmable gate array (FPGA) module to collect data from up to 8 unique NI modules and transmit the information through Ethernet to a computer at up to 1000 Mb/s. For this experiment a total of 7 cRIO modules were utilized. The model numbers for these modules, their quantities, the mode it was operated in (RT/FPGA), and the specific function within the experiment are listed below.

- 4 × NI-9211 Thermocouple Cards (RT)
 - 16 × Input - Thermocouple measurements
- 1 × NI-9205 Analog Input (RT)
 - 4 × Input - Differential Pressure Sensors
 - 1 × Input - Absolute Pressure Sensor
 - 1 × Input - Shunt Resistor Voltage
- 1 × NI-9263 Analog Output (RT)
 - 1 × Output - Heater Voltage
 - 1 × Output - Fan Voltage
 - 1 × Output - Valve Position
 - 1 × Output - Power Supply Current Limit (5V Constant)
- 1 × NI-9411 Digital I/O (FPGA)
 - 1 × Input - Fan Encoder Pulse Count

3.4 Wind Tunnel Design

Ideally the wind tunnel should have no influence on the process of forced convection and should be completely removed as a variable within the experiment. In other words, the wind tunnel should deliver perfectly uniform, constant velocity air over the entire wetted area of the heat sink. In practice, this is never the case since no system is ideal. However, steps can be taken to minimize any adverse effects the wind tunnel has on the quality of the flow over the heat sink. To do this several guidelines that have been developed and proven were adopted for this experiment. Many of these guidelines are published as standards in AMCA: 210-99 [15]. This reference, along with some others, offers recommendations for duct settling lengths needed to create a uniform flow necessary for the reliable and accurate dynamic pressure measurements via a Pitot tube. Figure 3.6 shows how the minimum length requirements are used between critical

components within a duct to allow for the accurate air velocity measurement with a Pitot tube.



NOTES

1. Dotted lines on fan inlet indicate an inlet bell and one equivalent duct diameter which may be used for inlet duct simulation. The duct friction shall not be considered.
2. Dotted lines on the outlet indicate a diffuser cone which may be used to approach more nearly free delivery.

Figure 3.6 Design Length Strategy for Duct Air Velocity Measurement [15]

These length recommendations are based off of multiples of the ducts diameter or effective diameter, known as the hydraulic diameter (D_H). This allows for the standards to be scalable to any shape of duct (e.g., rectangular, square). The following guidelines [15] [16] for facilitating accurate airflow measurement were used:

- Located the Pitot tube section providing 5 or more duct diameters upstream and 1-1/2 or more diameters down stream of Pitot tube free of elbows, size changes or obstructions.
- Use a honeycomb type of flow straightener 5 duct diameters upstream of Pitot tube
- The distance between the fan and flow straightener should be no less than 3.5 duct diameters.
- Duct diameter should be at least 30 times the diameter of the Pitot tube.

3.4.1 Design Integration

Using the guidelines for airflow measurement as requirements it is possible to begin the development of putting physical dimensions to the wind tunnel design. The first step was to select the desired size of the duct, since many of the requirements for duct length are dependent on the hydraulic diameter of the duct. There are three factors driving this portion of the design; the heat sink geometry, the diameter of the fan and the allotted space within the environmental chamber.

The fan diameter is 3.0 inches, any duct size chosen should be less than or equal to this size. Having a duct size greater than this would limit the maximum air flow within the duct ultimately lowering the total dynamic pressure and making an accurate reading more difficult. Additionally, any duct size chosen should be similar to the overall profile size of the heat sink (1.813 in. \times 1.25 in.). The reason for this is that all of the air flow will be directed through the channels of the heat sink (no bypass air). This is to insure a more accurate approximation for air velocity over the heat sink surface, measured from the Pitot tube. Having no bypass air means an approximation would not need to be made of the actual average velocity through the heat sink channels. In a bypass air situation the air over the heat sink is slightly less than the average. This is due to added surface friction and boundary layer forces dropping a greater pressure across the finned section of the duct. Instead, with no bypass air, the average air velocity over the surface can easily be determined based on the change in duct cross-sectional area. The duct diameter should also closely emulate the size of the heat sink to minimize the size of any expansion or contractions that will need to happen as a result of a duct size change.

The last and most difficult constraint, to the design of the wind tunnel, was the size of useable space inside the environmental chamber. A measurement of this space shows the base of 21 in. by 21 in. and 25 in. in height. It is desirable that the duct be on a flat surface to allow for easy construction and integration of all other necessary components. Therefore, all of the length requirements much fit within a 21 in. \times 21 in. square on the inside floor of the environmental chamber. To maximize the one-dimensional length, the duct was oriented from one corner to the other along the diagonal of the square base. This gave a one-dimensional length of 29.7in. However, since the wind tunnel was three-dimensional the true duct length was less than this since it would impact the walls at the corners in the environmental chamber.

Dictated by the size of the heat sink, a 2.0 in. \times 2.0 in. square duct was chosen. Calculations of the minimum lengths governing the distance between certain components of the wind tunnel were then carried out based on the requirements for accurate flow measurement. Table 3-1 shows the computed values for the necessary section length of the duct based off multiples of the hydraulic diameter, D_H .

The hydraulic diameter is an attribute commonly used in describing duct geometry in non-circular ducts, such as in this case. It acts as an equivalent dimension simplifying the alternate duct shape to as if they were circular. This allows one to apply calculations normally reserved for circular flows to any geometry. In this case the duct in question was a 2.0 in. square duct, where the hydraulic diameter is represented as,

Equation 3-1

$$D_H = \frac{4ab}{2(a + b)}$$

Where a , is the height and b , is the width of the duct. Therefore, the hydraulic diameter for this duct is 2.0 inches.

Table 3-1 Critical Requirements for Duct Length

Length (in.)	Element
7.0	Fan to Honeycomb exit, Settling Distance $\sim 3.5 \times D_H$
1.0	Honeycomb Size (<i>not in total sum</i>)
10.0	Honeycomb to Pitot Tube, Settling Distance $\sim 5.0 \times D_H$
1.5	Pitot Tube Size
3.0	Pitot Tube to Heat Sink, Settling Distance $\sim 1.5 \times D_H$
4.0	Heat Sink Size
2.0	Exit Section $1.0 \times D_H$
27.5	TOTAL

From Table 3-1, it was determined that a duct length of 27.5 in. was needed to allow for accurate airflow measurement. However, this only accounts for the wind tunnel length after the fan, and not the fan (1.75 in.) or the control valve (7.75 in.). Ultimately, the wind tunnel would need to be 37 in. long in order to fit all the necessary elements of the experiment. This is 8 inches longer than the environmental chamber would allow, in a straight line. Decreasing the size of the duct (i.e. D_H) to just the height and width of the heat sink did help, but was only able to decrease the duct length by about 5.0 inches. Instead, a new design was adopted that did not require the wind tunnel to be in a straight line. Several design concepts were vetted that incorporated turns within the duct. Figure 3.7 shows a concept where the wind tunnel turns 180° back under itself.

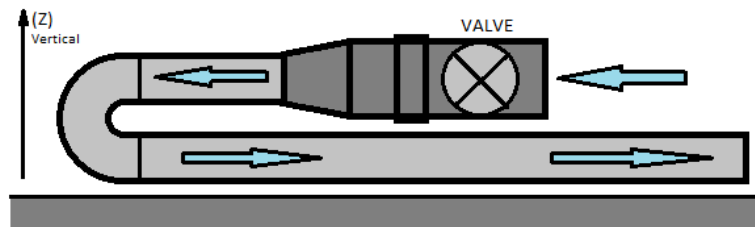


Figure 3.7 Wind Tunnel Design, 180° Turn Concept.

The valve, fan and settling length after the fan were all in the upper section of the wind tunnel and the honeycomb, settling distance for the flow measurement, Pitot tube,

heat sink and exit were in the lower section. This decreased the longest linear section of the wind tunnel to 20.5 in. which worked although it added some other components such as turns within the duct.

3.4.2 Detailed Design

In order to properly determine if this concept would work, a detailed design was developed and integrated into the allotted space of the environmental chamber, using a three dimensional (3D) CAD model. By taking and modeling the existing components (fan, valve, Pitot tube and heat sink) a wind tunnel was designed around these parts and their settling lengths. The duct size was selected to be a 2.0 in. square duct. Fitting the 20.5 in. test section into the environmental chamber proved to be a tighter fit than it did on paper. The model in Figure 3.8 shows how the integration of the wind tunnel into a 3-Dimensional space limited how close the ducting could be to the two opposing corners of the environmental chamber. This is because the incorporation of the turning sections (elbows) accounted for remaining of the allocated space.

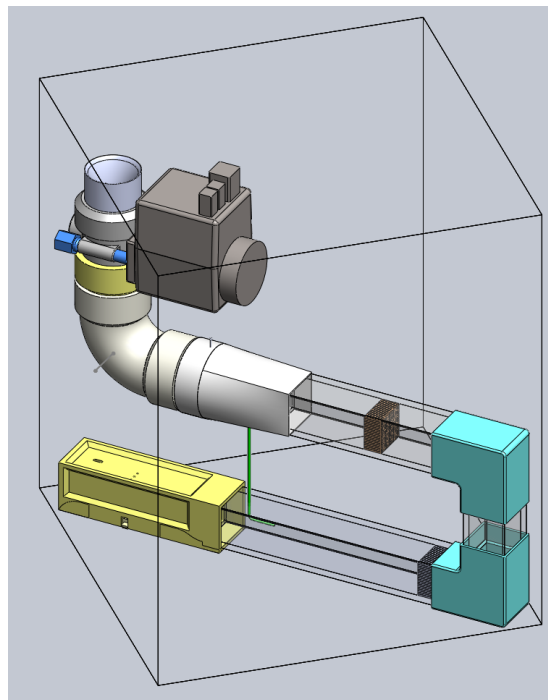


Figure 3.8 Detailed CAD Model of Wind Tunnel Design

Figure 3.9 shows the final configuration of the wind tunnel with the length dimensions displayed for the spacing between crucial sections.

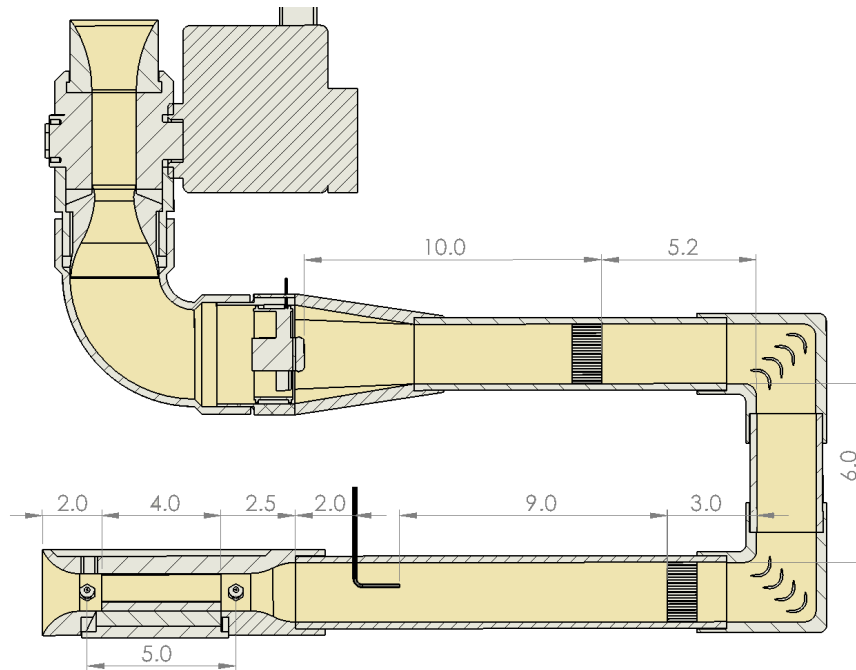


Figure 3.9 Wind Tunnel Sectioned View with Dimensions, in Inch.

It is worth noting that the 9 inches separating the honeycomb (Figure 3.10, Section 16) and inlet to the Pitot tube does not meet the minimum recommended settling distance of 10 in. Due to fitting other critical components near the heat sink the Pitot tube had to be moved up by 1 inch. The consequence of this was thought to be minimal given that the distance it is moved reduced the settling distance by 5% and the $5 \times D_H$ is an approximation of the necessary settling length.

3.4.3 Wind Tunnel Section Design

Critical to the functionality of the wind tunnel was its ability to maximize the airflow over the heat sink test section, thus allowing for the widest range of Reynolds numbers tested. To achieve this, the wind tunnel was designed to minimize the pressure drop experienced by the flow. The exercise of minimizing the pressure loss is a well-documented field that has a wide range of academic and industrial references. Figure 3.10 shows the elements adopted by this design in order to minimize the pressure loss within the wind tunnel.

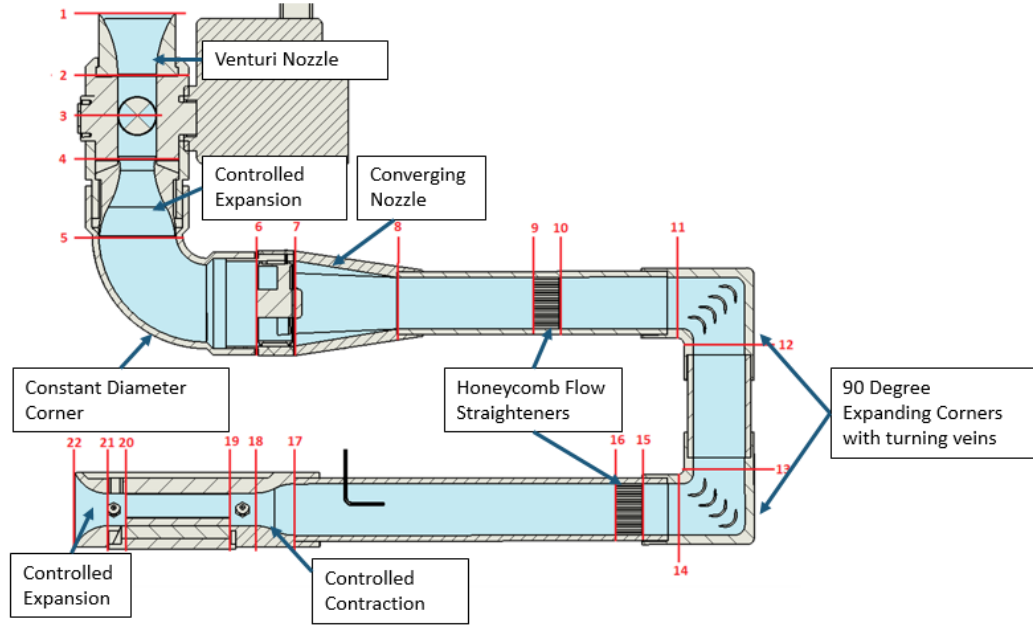


Figure 3.10 Features Used to Minimize Pressure Loss in Wind Tunnel.

The majority of the components are controlled contractions (nozzles) or expansions (diffusers) within the duct. The other two major elements are the two honeycomb flow straighteners and the two 90° expanding corners. The pressure losses within a pipe flow can be separated into two categories, the major and the minor losses. The total pressure loss or system resistance (p_{loss}) is found by a sum of both the major (p_{major}) and minor losses (p_{minor}), as seen by Equation 3-2.

Equation 3-2

$$p_{loss} = \sum p_{major} + \sum p_{minor}$$

The major loss, or head loss, in a pipe flow are due to friction with the moving fluid against the walls of the duct. These losses are dependent on the velocity of the flow (U_{∞}), the hydraulic diameter of the pipe (D_H , Equation 3-1), the length of the pipe (L), the density of the air (ρ), and the friction coefficient. The friction coefficient (f), for laminar flow, was estimated by the following equation.

Equation 3-3 [17]

$$f = \frac{64}{Re_D}; \quad Re_D \lesssim 3,000$$

For turbulent flow, the friction coefficient was found from the following equation.

Equation 3-4 [18]

$$f = 0.316 Re_D^{-1/4}; \quad 3,000 \lesssim Re_D \lesssim 2 \times 10^4$$

The Reynolds number (Re_D) of the flow is based on the hydraulic diameter within the duct element.

Equation 3-5

$$Re_D = \frac{D_H U_\infty \rho}{\mu}$$

The major losses in all sections of the duct were calculated through the use of Equation 3-6 [19].

Equation 3-6

$$p_{major\ loss} = f \left(\frac{L}{D_H} \right) \left(\frac{\rho U_\infty^2}{2} \right)$$

The minor losses are associated with changes in the cross-sectional area of the duct, changes in velocity or direction of airflow or obstructions in the air stream. For each case the non-dimensional change in pressure is referred to as the loss coefficient, η . The loss coefficient is related to the pressure drop through the use of the following equation.

Equation 3-7

$$p_{minor\ loss} = \eta \left(\frac{\rho U_\infty^2}{2} \right)$$

For this experiment, the minor losses were either from a cross-sectional area change or change in direction from a bend in the wind tunnel. The pressure loss from both of these cases is computed differently. A full record of the computations for determining the minor losses for every section within the wind tunnel is presented in APPENDIX B.

The final element that was considered when evaluating the total wind tunnel pressure loss was the heat sink. This was estimated through a method developed by Simons [20] for predicting the pressure drop across parallel plate heat sinks. This method and its uses are further detailed in Section 4.2.2 of this thesis.

3.4.4 Pressure Loss

After all the elements of the wind tunnel were designed and the computations for estimating their major and minor losses were determined, it was necessary to compute the total system loss, or system resistance. There were several reasons for computing the predicted system resistance before completing construction of the wind tunnel. The first reason was for the selection of the differential pressure transducers for measuring flow velocity and static pressure drop. These sensors were relatively expensive and it was useful to know the exact ones that were needed for the experiment rather than using a sensor that was out of range and needing to purchase more. The second reason was to

develop predictions for a comprehensive testing matrix. Knowing the capabilities of the wind tunnel (maximum volumetric flow rate) ahead of time would give insight to the expected airflow conditions over the heat sink. This would allow for testing parameters to be developed with the goal of maximizing the range of Reynolds number tested over the heat sink. Lastly, this information was used to validate the wind tunnel.

The process of calculating the total system pressure loss was fairly simple. The system pressure loss is a sum of all the major and minor losses for every section throughout the wind tunnel (Equation 3-2). This will yield the loss coefficients for each section. However the pressure loss is also dependent on the velocity of the flow, as seen in Equation 3-7. The velocity is derived from dynamic pressure (p_{Dy}), measured at the Pitot tube, shown in the following equation.

Equation 3-8

$$U_{\infty} = \sqrt{\frac{2p_{Dy}}{\rho}}$$

In order to find the pressure drop within the wind tunnel both the density of the air and velocity had to be known. This was achieved by plotting the wind tunnel system resistance against the fan curves [14] at various ambient pressures (i.e., air densities), shown in Figure 3.11, Figure 3.12, Figure 3.13, and Figure 3.14. The intersection of the system resistance and fan flow rate were found. This predicted the maximum flow rate of the system for a given fan RPM.

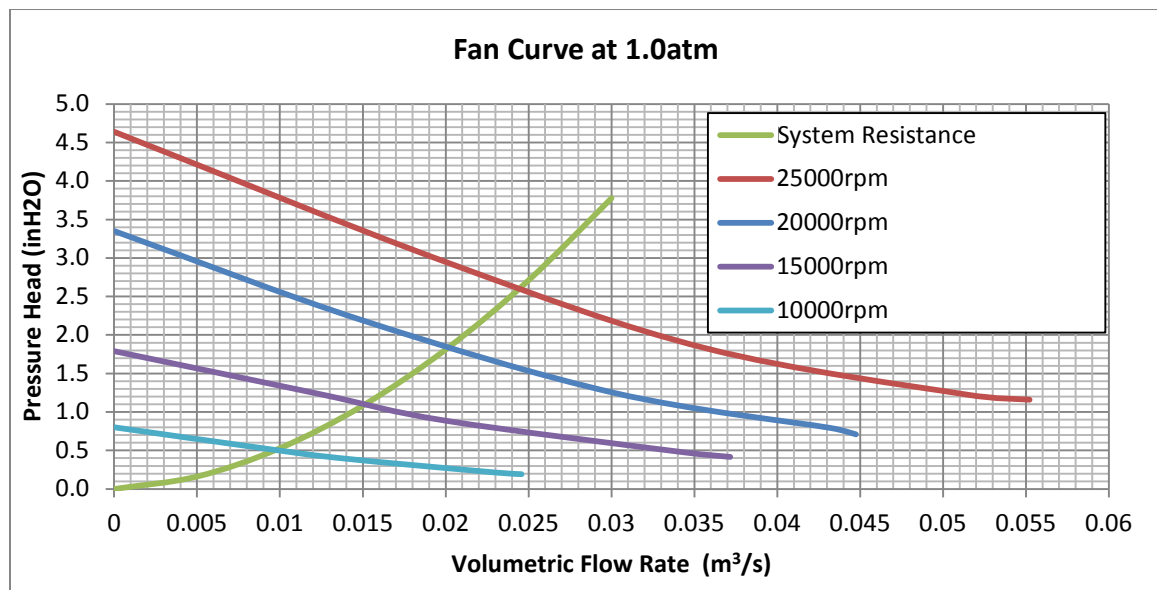


Figure 3.11 Fan Curve and System Resistance at 1.0 atm

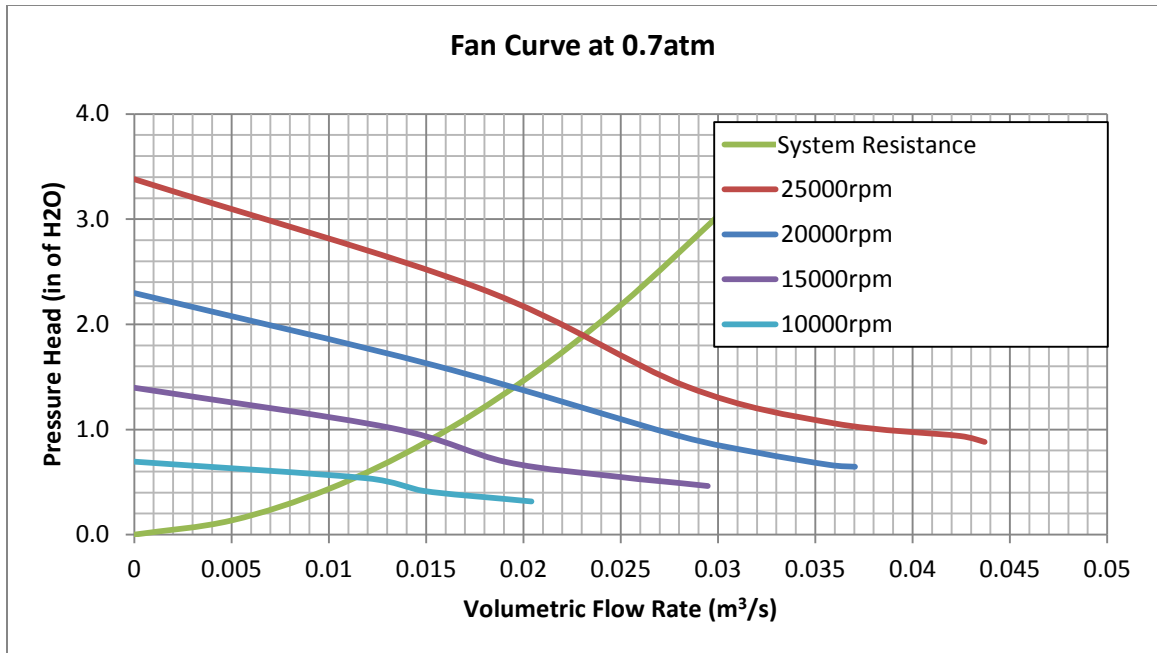


Figure 3.12 Fan Curve and System Resistance at 0.7 atm

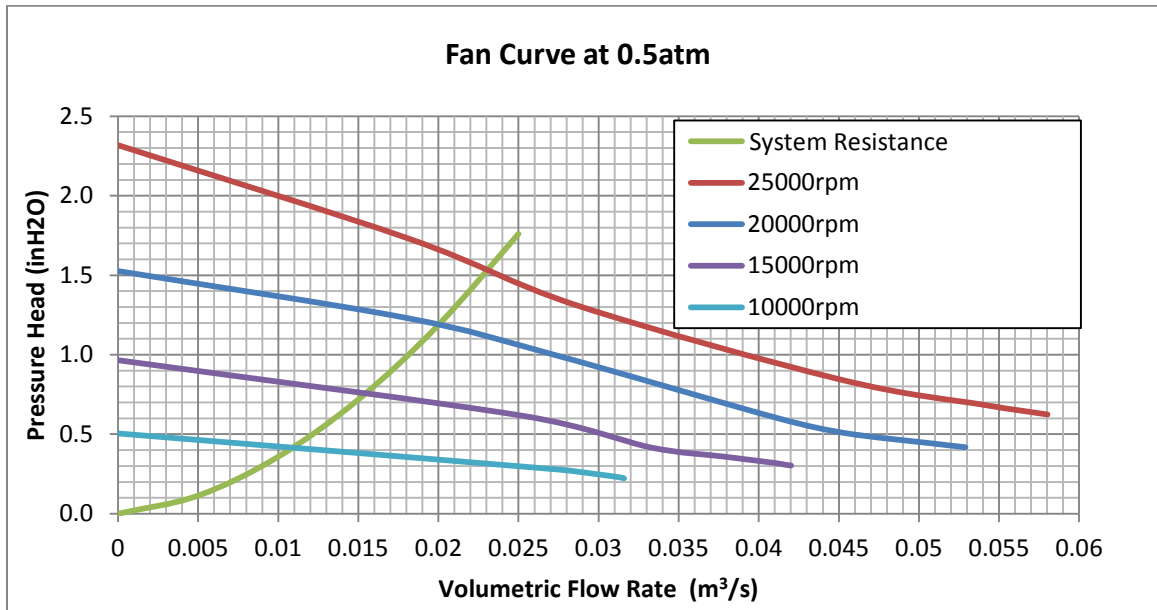


Figure 3.13 Fan Curve and System Resistance at 0.5 atm

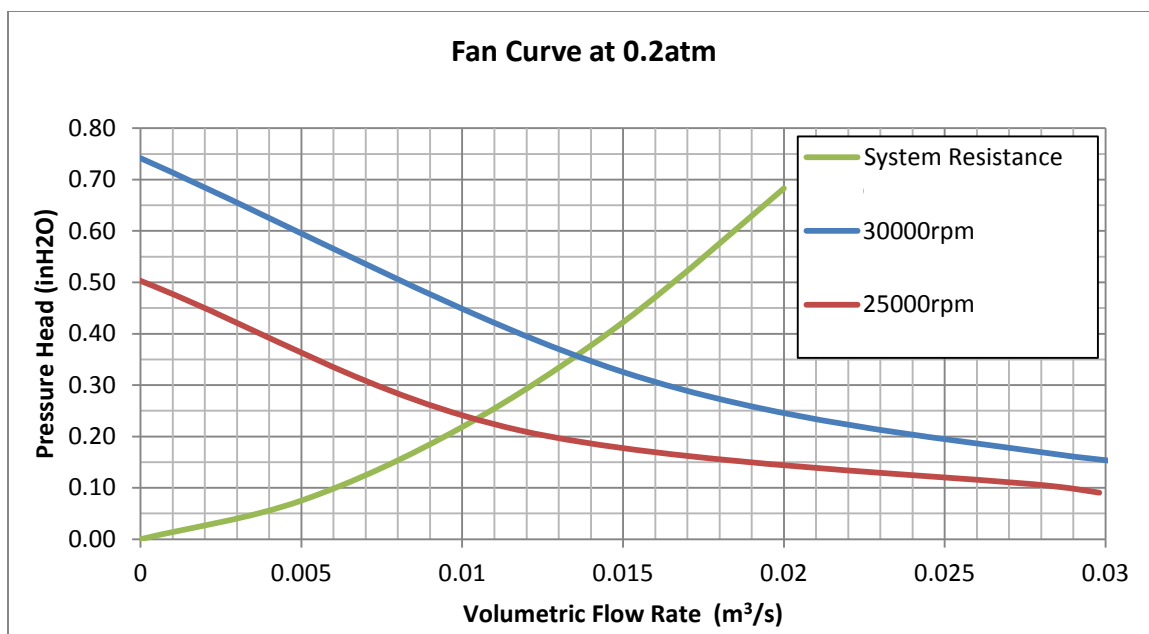


Figure 3.14 Fan Curve and System Resistance at 0.2 atm

The values found at the intersection point are shown in Table 3-2.

Table 3-2 Values for the Intersection Points of the Fan Curves and System Resistance

Pressure (atm)	Density (kg/m ³)	Fan Speed (RPM)	Flow Rate (m ³ /s)	Pressure Head (inH ₂ O)
1.00	1.202	25,000	0.024	2.59
0.70	0.918	25,000	0.023	1.89
0.50	0.699	25,000	0.023	1.52
0.20	0.326	25,000	0.011	0.24
0.20	0.326	30,000	0.014	0.36

From the intersection points of the fan curves, both the volumetric flow rate and pressure head were determined. Next, the local velocity at every point within the duct can be determined by dividing the volumetric flow rate by the cross-sectional area. A table displaying all the values for pressure loss as well as the flow conditions at every point within the duct for the case of running the fan at 25,000 RPM at 1.0 atm can be found in APPENDIX C. By knowing the velocity within the duct at the location of the Pitot tube and over the heat sink it was possible to accurately size the sensors used for the experiment.

3.5 Test Matrix

Test matrix was derived by finding the maximum airflow conditions within the duct and subdividing it into five 20% increments based on velocity. This was done for all cases where the maximum volumetric flow rate was determined using the fan curve. Then by linear interpolation of these points, estimations were made for the maximum airflow at the remaining conditions, (0.9, 0.8, 0.6, 0.4, 0.3, and 0.1 atm). Table 3-3 is the derived test matrix which gives estimation for the flow conditions such as velocity, Reynolds number, dynamic pressure, and static pressure throughout the entire range of parameters that this test was interested in. The values listed under 'Atmosphere and Altitude' were based on the 1976 Standard Atmosphere [7]. Since the experiment was not conducted at sea level the corresponding pressure for 823 feet ASL was used. The values for the dynamic pressure in the duct were used to size the differential pressure sensor for the air velocity measurement. The static pressure drop across the heat sink was also used to size which sensor will be appropriate for this measurement.

Table 3-3 Preliminary Test Matrix for Desired Airflow Conditions

		Atmosphere and Altitude					Duct Air Flow			Heat Sink Air Flow		
		Percent of Maximum airflow	Atmospheric Pressure (atm)	Density (kg/m3)	Altitude (feet)	Atmospheric Pressure (psi)	Kinematic Viscosity (m2/s)	Velocity (m/s)	Reynolds Number	Dynamic Pressure (in of H2O)	Velocity (m/s)	Reynolds number
97% Atmosphere	100%	0.97	1.196	823	14.26	1.52E-05	9.46	31719	0.2148	26.36	17481	1.3878
	80%	0.97	1.196	823	14.26	1.52E-05	7.57	25375	0.1375	21.09	13985	0.9317
	60%	0.97	1.196	823	14.26	1.52E-05	5.68	19031	0.0773	15.82	10489	0.5603
	40%	0.97	1.196	823	14.26	1.52E-05	3.78	12687	0.0344	10.54	6993	0.2766
	20%	0.97	1.196	823	14.26	1.52E-05	1.89	6344	0.0086	5.27	3496	0.0855
90% Atmosphere	100%	0.90	1.125	2885	13.23	1.61E-05	9.33	29426	0.1966	26.00	16221	1.2903
	80%	0.90	1.125	2885	13.23	1.61E-05	7.46	23541	0.1258	20.80	12977	0.8673
	60%	0.90	1.125	2885	13.23	1.61E-05	5.60	17656	0.0708	15.60	9732	0.5224
	40%	0.90	1.125	2885	13.23	1.61E-05	3.73	11770	0.0315	10.40	6488	0.2585
	20%	0.90	1.125	2885	13.23	1.61E-05	1.87	5885	0.0079	5.20	3244	0.0803
80% Atmosphere	100%	0.80	1.022	6045	11.76	1.77E-05	9.14	26192	0.1714	25.48	14442	1.1545
	80%	0.80	1.022	6045	11.76	1.77E-05	7.31	20954	0.1097	20.39	11553	0.7774
	60%	0.80	1.022	6045	11.76	1.77E-05	5.49	15715	0.0617	15.29	8665	0.4695
	40%	0.80	1.022	6045	11.76	1.77E-05	3.66	10477	0.0274	10.19	5777	0.2333
	20%	0.80	1.022	6045	11.76	1.77E-05	1.83	5238	0.0069	5.10	2888	0.0730
70% Atmosphere	100%	0.70	0.918	9540	10.29	1.97E-05	8.95	23032	0.1476	24.96	12703	1.0236
	80%	0.70	0.918	9540	10.29	1.97E-05	7.16	18425	0.0945	19.97	10162	0.6907
	60%	0.70	0.918	9540	10.29	1.97E-05	5.37	13819	0.0531	14.98	7622	0.4183
	40%	0.70	0.918	9540	10.29	1.97E-05	3.58	9213	0.0236	9.98	5081	0.2088
	20%	0.70	0.918	9540	10.29	1.97E-05	1.79	4606	0.0059	4.99	2541	0.0659
60% Atmosphere	100%	0.60	0.810	13470	8.82	2.24E-05	8.93	20283	0.1297	24.91	11186	0.9266
	80%	0.60	0.810	13470	8.82	2.24E-05	7.15	16226	0.0830	19.92	8949	0.6266
	60%	0.60	0.810	13470	8.82	2.24E-05	5.36	12170	0.0467	14.94	6712	0.3806
	40%	0.60	0.810	13470	8.82	2.24E-05	3.57	8113	0.0208	9.96	4475	0.1908
	20%	0.60	0.810	13470	8.82	2.24E-05	1.79	4057	0.0052	4.98	2237	0.0608
50% Atmosphere	100%	0.50	0.699	17970	7.35	2.59E-05	8.913	17460	0.1114	24.85	9629	0.8254
	80%	0.50	0.699	17970	7.35	2.59E-05	7.13	13968	0.0713	19.88	7703	0.5597
	60%	0.50	0.699	17970	7.35	2.59E-05	5.35	10476	0.0401	14.91	5777	0.3412
	40%	0.50	0.699	17970	7.35	2.59E-05	3.57	6984	0.0178	9.94	3852	0.1720
	20%	0.50	0.699	17970	7.35	2.59E-05	1.78	3492	0.0045	4.97	1926	0.0554
40% Atmosphere	100%	0.40	0.583	23265	5.88	3.11E-05	7.77	12698	0.0706	21.66	7003	0.5690
	80%	0.40	0.583	23265	5.88	3.11E-05	6.22	10158	0.0452	17.33	5603	0.3881
	60%	0.40	0.583	23265	5.88	3.11E-05	4.66	7619	0.0254	13.00	4202	0.2385
	40%	0.40	0.583	23265	5.88	3.11E-05	3.11	5079	0.0113	8.67	2801	0.1217
	20%	0.40	0.583	23265	5.88	3.11E-05	1.55	2540	0.0028	4.33	1401	0.0402
30% Atmosphere	100%	0.30	0.462	29775	4.41	3.92E-05	6.57	8515	0.0401	18.33	4697	0.3630
	80%	0.30	0.462	29775	4.41	3.92E-05	5.26	6812	0.0257	14.67	3758	0.2496
	60%	0.30	0.462	29775	4.41	3.92E-05	3.94	5109	0.0144	11.00	2818	0.1551
	40%	0.30	0.462	29775	4.41	3.92E-05	2.63	3406	0.0064	7.33	1879	0.0805
	20%	0.30	0.462	29775	4.41	3.92E-05	1.31	1703	0.0016	3.67	939	0.0275
20% Atmosphere	100%	0.20	0.326	38385	2.94	5.56E-05	5.231	4779	0.0179	14.59	2637	0.1972
	80%	0.20	0.326	38385	2.94	5.56E-05	4.18	3823	0.0115	11.67	2109	0.1374
	60%	0.20	0.326	38385	2.94	5.56E-05	3.14	2868	0.0064	8.75	1582	0.0870
	40%	0.20	0.326	38385	2.94	5.56E-05	2.09	1912	0.0029	5.84	1055	0.0465
	20%	0.20	0.326	38385	2.94	5.56E-05	1.05	956	0.0007	2.92	527	0.0168
10% Atmosphere	100%	0.1	0.163	52805	1.47	1.11E-04	3.62	1655	0.0043	10.11	914	0.0748
	80%	0.1	0.163	52805	1.47	1.11E-04	2.90	1324	0.0027	8.09	731	0.0537
	60%	0.1	0.163	52805	1.47	1.11E-04	2.17	993	0.0015	6.06	548	0.0354
	40%	0.1	0.163	52805	1.47	1.11E-04	1.45	662	0.0007	4.04	365	0.0200
	20%	0.1	0.163	52805	1.47	1.11E-04	0.72	331	0.0002	2.02	183	0.0079

3.6 Experiment Construction

The many unique sections of the duct were built using several methods. Figure 3.15 shows the entire experiment setup inside the environmental chamber.



Figure 3.15 Wind Tunnel inside Environmental Chamber.

A combination of commercial off-the-shelf (COTS) items, custom, and 3D printed parts was used for the build. The constant diameter corner and a friction fitting to attach it to the actuated valve were purchased. The clear acrylic straight square duct was built from a flat 0.22" thick sheet. The intricate components that could not be purchased or easily fabricated were made using 3D-Printing. A total of 7 parts were made using 3D printing, shown in red in Figure 3.16.

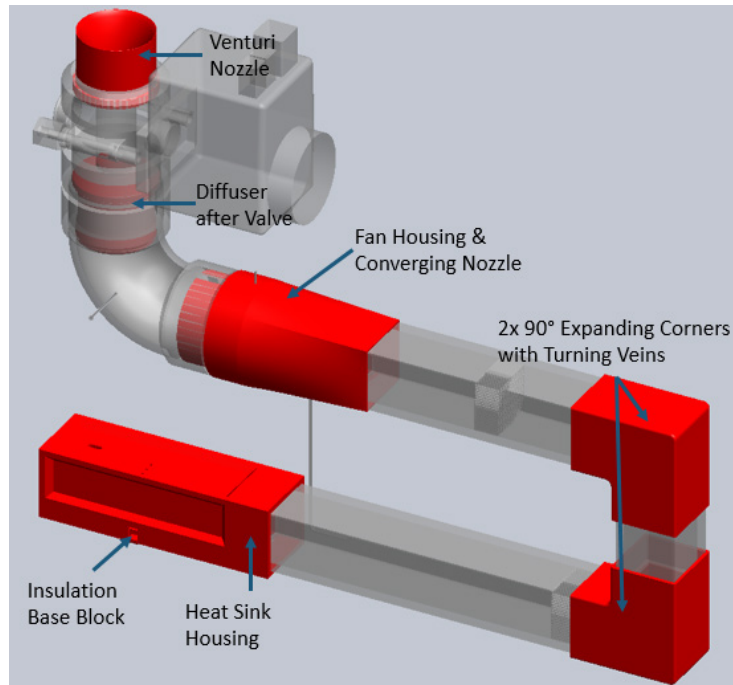


Figure 3.16 3D Printed Parts within Wind Tunnel

Of the 7 parts, 5 were made using ABS plastic with a tolerance estimated to ± 0.035 in. The other two remaining parts, the Heat Sink Housing and the Insulation Base Block, were made using polycarbonate plastic also with a tolerance of ± 0.035 in. The decision was made to use polycarbonate (PC) for these parts because of its higher working temperature. The glass temperature of PC is around 140°C . This is 20°C higher than the temperature rating of the heaters. This would ensure that heat sink will never get hot enough to permanently damage the housing. Additionally, all of the 3D printed parts that came in contact with the airstream were smoothed to minimize friction losses, with the exception of the two expanding corners. Sanding the inner surface of these parts was made overly difficult given the turning vanes obstructing the most of the surface.

3.6.1 Sensors: Types, Usage and Installation

The next challenge in the construction of the wind tunnel was the installation of all the sensors used to operate, control, and conduct measurement for the experiment. Three different pressure measurements are needed for this experiment; dynamic pressure using the Pitot tube, static pressure difference across the heat sink, and ambient pressure. For these three measurements five sensors are needed. Both the dynamic and static pressure drop measurements used two different differential pressure sensors, for a low and high range. Because this experiment covered such a wide range of pressure measurements, the uncertainty of these measurements was minimized by using two ranges for sensors. As seen in Table 3-3, the dynamic measurement could see a pressure range of $0.2 - 0.0007$ inH₂O and a static pressure range of $1.4 - 0.02$ inH₂O. For these two measurements Setra Model 264 Differential pressure transducers were chosen. The

ranges chosen for both measurements were 0-0.1 & 0-0.25 inH₂O for the dynamic measurement and 0-1.0 & 0-2.5 inH₂O for the static pressure measurement. Switching between either sensor was easily done prior to an experiment, based on the anticipated measurement range. The third pressure measurement needed was the absolute pressure within the environmental chamber. For this the Setra Model 552 absolute pressure sensor was used. It was capable for covering the entire range of pressures for the experiment, 0-15 PSIA. All five of these sensors required an excitation voltage of 9-30 VDC and output 0-5VDC for their full scale range. They were all mounted within the environmental chamber with the exception of the absolute sensor that was relocated to a fitting attached to the outside of the chamber. This was due to an unknown error with the sensor output that was observed when operating it inside the chamber. Figure 3.17 shows how the four differential sensors were mounted within the experimental setup inside the environmental chamber.



Figure 3.17 Mounting Locations of the 4 Differential Sensors.

The transition of changing from one sensor to the other was made by moving the vinyl tubing that connects to the Pitot tube or static pressure taps from one sensor to the other. The location of the measurement devices were also carefully placed. As discussed in Section 3.4 the location of the Pitot tube is placed 9.0 in. downstream of the honeycomb flow straightener at the center point of the duct. Figure 3.18 shows the mounting location for the two static pressure taps used to measure the difference in pressure before and after the heat sink.

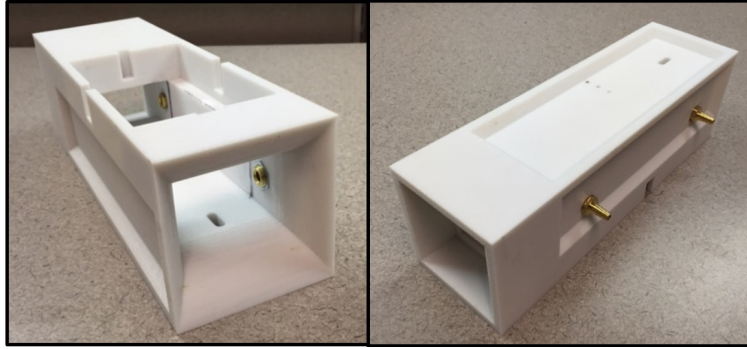


Figure 3.18 Location of Pressure Taps on Heat Sink Housing

A total of 16 Type-T thermocouples were used in this experiment. Table 3-4 lists all the thermocouple designations and their location within the experiment.

Table 3-4 Thermocouple Numbering

TC NUMBER	MEASUREMENT LOCATION
TC01	AIR AT INLET 1
TC02	AIR AT INLET 2
TC03	HEAT SINK BASE 1
TC04	HEAT SINK BASE 2
TC05	HEAT SINK BASE 3
TC06	HEAT SINK BASE 4
TC07	HEAT SINK BASE 5
TC08	HEAT SINK TIP 1
TC09	HEAT SINK TIP 2
TC10	HEAT SINK TIP 3
TC11	AIR AT EXIT 1
TC12	AIR AT EXIT 2
TC13	HOUSING EXTERNAL 1
TC14	FAN
TC15	HOUSING EXTERNAL 2
TC16	AIR AT EXIT 3

A total of 5 thermocouples are used for the measurement of the temperature of the heat sink base. The thermocouples are placed at the five locations shown in Figure 3.19, with TC03 being at the upstream most location and TC06 being closest to the exit of the air leaving the heat sink.

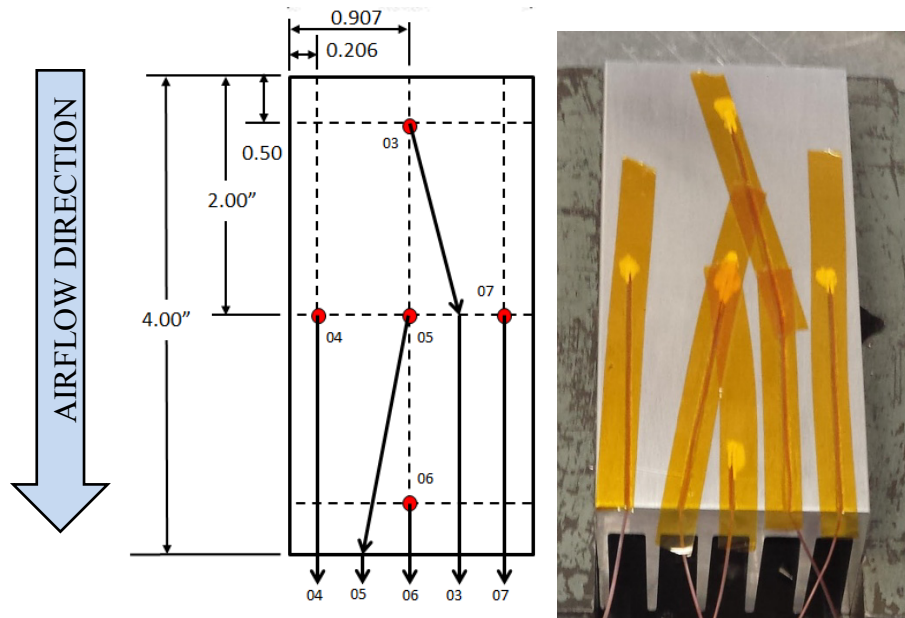


Figure 3.19 Heat Sink Base Thermocouple Placement in Inch

These 5 measurements were used in the direct calculation for the thermal resistance, which was used to find the experimental heat transfer coefficient. They were also used to observe the symmetry and/or uniformity of the heat source. If any irregular or unexpected pattern was observed it would be a concern. To ensure the quality of these measurements, steps were taken to eliminate measurement error. The thermocouples are located on the base of the heat sink just above the interface point between the heater and heat sink. To avoid any contact that the thermocouple tips would have with the heater, tiny holes were drilled at each placement location. Thin channels were then cut for the thermocouple wire to be run to the rear of the duct so that when the heater was installed there was a flat surface to surface contact between heater and the aluminum base. Lastly, thermal grease was used to fill the holes at the thermocouple tips and Kapton tape was used to cover the interface and create a barrier between heater and thermocouple, and to eliminate air pockets that may have existed. This method of attachment was also used in other surface thermocouple placement (e.g., the tips of the heat sink, the fan, and sides and bottom of the housing).

Figure 3.20 shows the relative location of the two thermocouples used for measuring the temperature of the air entering the test section prior to encountering the heat sink.

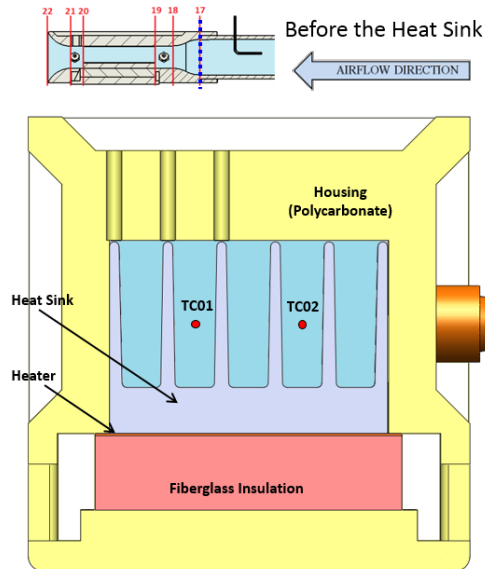


Figure 3.20 Thermocouple Placement at the Entrance of the Test Section, Shown as Section 17

Those two stainless steel thermocouple probes were placed at the inlet to the heat sink housing, roughly 1.5 inches upstream of the heat sink. The air within the environmental chamber was kept at a very uniform temperature by means of an internal fan agitating the air. Because of this, very little temperature variation is expected of the air entering the heat sink inlet and only two thermocouples were thought needed for this measurement.

Figure 3.21 shows a cross-section for the test section at the midpoint for the heat sink, 2.0 inches from the front and rear.

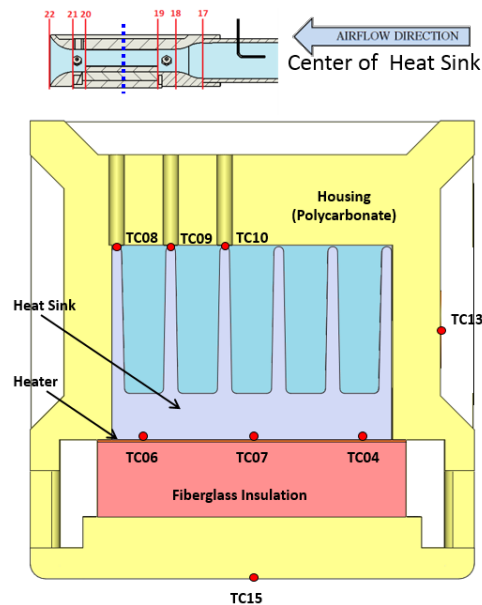


Figure 3.21 Thermocouple Placement at the Center of the Heat Sink

A total of 8 thermocouples are placed at this location. Of these, the three heat sink base thermocouples have been discussed. The other three placed at the tip of the heat sink fins, designated as TC08, TC09, and TC10, were used to give an inclination on the heat sink fin efficiently. Three were chosen to observe any variation in temperature across the tips. Unfortunately, one of these thermocouples was damaged during installation (TC08) and repairing it was considered untenable given its relatively low importance and high potential for damaging other thermocouples during the process. The last two thermocouples, TC13 and TC15, were later added to the experiment. Their purpose was to measure the housing temperature at the sides and base. This information was used to determine the thermal losses by conduction into the housing.

The last crucial measurement within the heat sink was the air at the exit of heat sink. This measurement, like the heat sink fin tip measurement, was not absolutely critical to the experiment but was found to be useful in post experimental analysis. The placement for these thermocouples is shown in Figure 3.22.

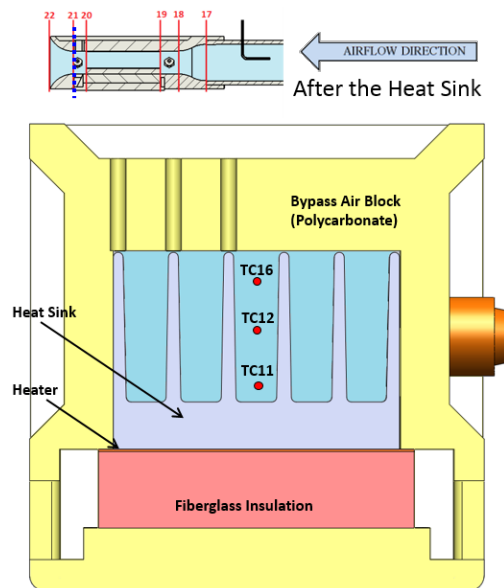


Figure 3.22 Thermocouple Placement at the Exit of the Heat Sink, Section 21

Obtaining a measurement for the average air temperature at exit was challenging. This was because the air temperature was likely not uniform, due to surface temperature variation, thermal boundary layer growth and asymmetric mixing of the air. For these reasons, it was determined that three thermocouples centered at the lower, middle and upper third of a single channel would give the best results for the average temperature of air leaving the center channel of heat sink.

Lastly, a thermocouple (TC14) was placed on the stator hub of the fan used to drive the air within the wind tunnel (Figure 3.23). This measurement was needed for the safe operation of the experiment. In some cases the fan was run beyond its spec power limits for extended periods of time. It became necessary to monitor the temperature of the fan and implement safety stops within the software to avoid thermal failure and permanent degradation of the motor.



Figure 3.23 Fan Thermocouple Placement

The last parameter needing recording for this experiment is the power dissipated by the heater. This was done by measuring the current flow to the heater via a shunt resistor. A shunt resistor is a highly stable and dependable method for measuring current for a constant DC voltage. By using a small electrical resistance (0.0197Ω) in the circuit and measuring the voltage drop across the resistor the current can be found. Equation 3-9 was used to determine the current by measuring the voltage drop across a known resistance.

Equation 3-9

$$I_{Heater} = \frac{V_{drop}}{R_{e,Shunt}}$$

The power to the heater is therefore $I_{Heater}^2 R_{e,Heater}$, where $R_{e,Heater}$ is the heater electrical resistance.

3.6.2 Wiring, Power Distribution & Programming

After all the instrumentation was selected and placed properly within the wind tunnel it became time for the final wiring of all sensors to the DAQ, distributing power to the necessary components, and programing the remote operation and data acquisition of the experiment. The wiring and methodology for power and signal commands are discussed here briefly. More details are available in the form of a wiring diagram in APPENDIX D. The approach taken when wiring many components with multiple power sources to a single data collection source was to allow all sources to act as isolated power sources with a single common ground terminated to earth at the DAQ. A grounding bus was made to do this. This was advantageous for a number of reasons. The primary was to

eliminate any ground loops. Secondly, this ensured that all measurements have the same common ground voltage. This guarantees that there was no electrical measurement offset errors.

The equipment used to power the electronics was as follows. For the heater and fan, two BK Precision series 1685B switch-mode power supplies were used. The power supplies were controlled by a 0-5 VDC source corresponding to a 0-60VDC, 5amp max output. The output will be controlled by the NI (cRIO). This allowed for active control of the fan and the power to the heater. All other electronics with the exception of the cRIO were powered by a common source, a laptop switching power supply outputting 19.5 volts, 3.0 amp maximum. This provided all 5 pressure transducers with the necessary excitation voltage, power for the shunt isolated amplifier, and the operating power for the actuated valve. The cRIO was powered by a benchtop DC power supply.

Since all of these components were being operated remotely within the vacuum chamber, wiring needed to pass into the chamber through a small circular hole on the side while maintaining an airtight seal. For this, a custom seal was designed. The seal was made of a 1/4" aluminum plate with holes cut for the 5 wire bundles that passed through. This was more advantageous than one large hole as less room temperature vulcanization (RTV) silicone was needed to fill the air gap between aluminum and wire insulation. Figure 3.24 shows the design, attachment, and sealing of the wire pass-through plate.

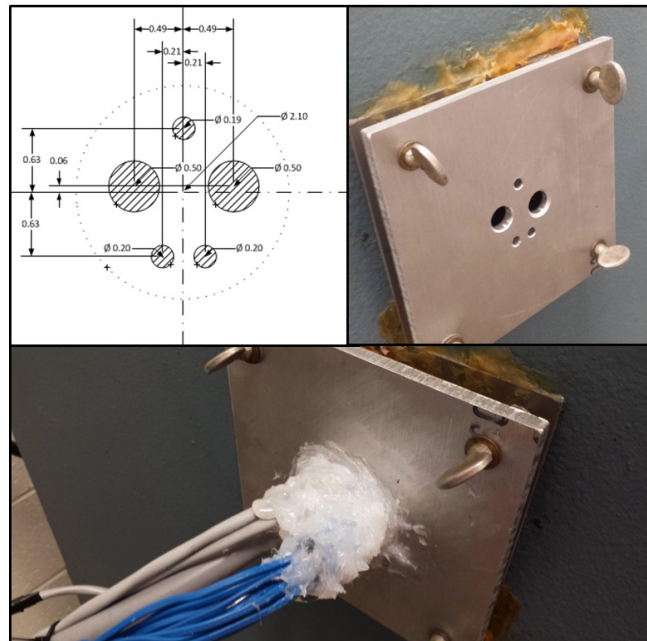


Figure 3.24 Wire Pass-Through Seal Design

The last step in the functionality of the experiment was the software programming for control and data acquisition. For this, NI LabVIEW 2014 was used. The software allowed for the creation of a customized virtual instrument (VI) for the NI cRIO chassis and modules to execute desired commands based on various settings and inputs. The goal

of this programming was the remote operation of experimental commands for airflow and heater power as well as recording of data. The program was given a target for airflow (dynamic pressure) and heater power (voltage drop across the shunt), and control loops within the VI manipulated the fan speed (voltage to the fan), valve position (0-10VDC signal voltage) and voltage to the heater (0-60V).

The original methodology for controlling airflow was to run the fan at a high speed and use only the valve to regulate airflow. However, this concept was abandoned to avoid running the fan in high fatigue conditions for longer than required periods of time. Instead, the following logic, shown in Figure 3.25, was used to achieve the desired air flow within the wind tunnel.

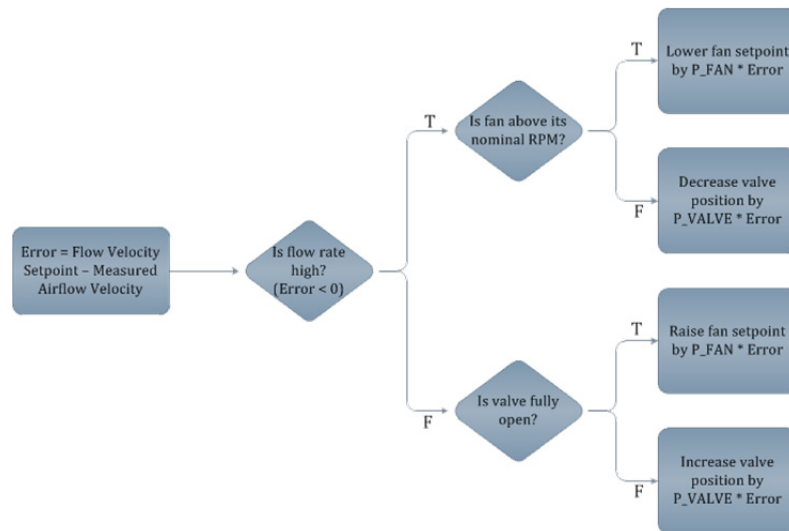


Figure 3.25 Air Flow Control Loop Operational Logic Diagram

In summary, this control scheme had two operating modes. The control loops for both of these operating modes as well as the hardware involved are shown in Figure 3.26.

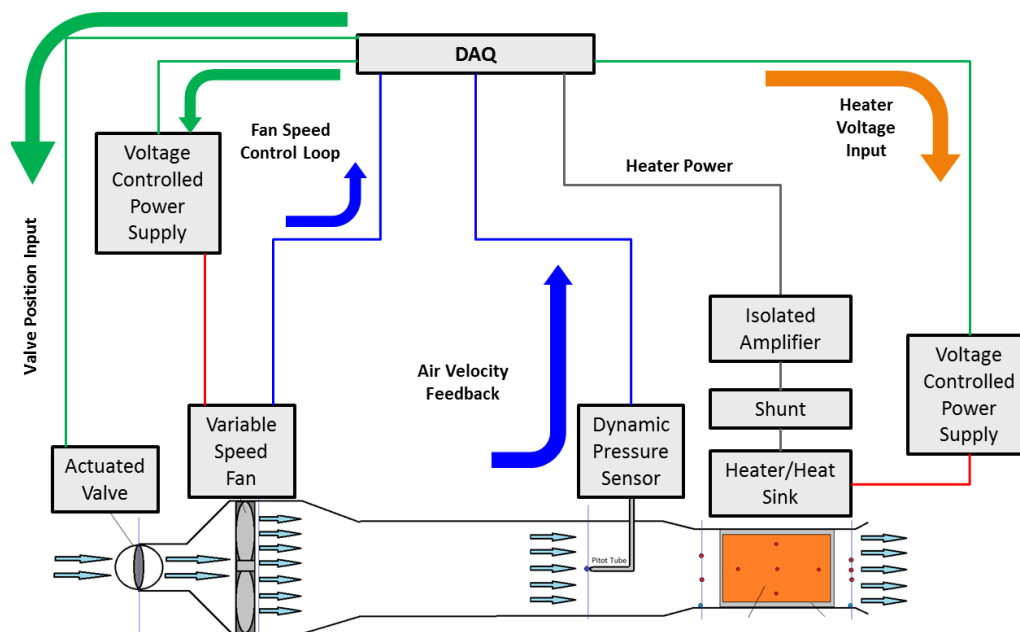


Figure 3.26 Wind Tunnel Control Diagram

The starting mode or default mode (valve control) used the valve to regulate airflow. The fan was run at 16,000 RPM, and the valve would open from the closed position, increasing the airflow. If this control scheme was able to reach the airflow set point then the program would actively regulate it to make sure it stays on target. This was needed since the fan required an active PID loop to keep it at constant speed, as it would lose efficiency when the temperature increased. The other control scheme (fan control) was activated when the valve reached the fully open position and the airflow target was not yet met. When this condition took place, the outer control loop would alter the fan speed set point, increasing it, until the target was achieved.

During any operation, the LabVIEW VI also had safety measures in place. If the temperature of the heat sink reached 120°C, the program cut power and cooled it down. Also, if the fan temperature reached 50°C, its voltage was decreased to a safe range and the valve was fully open for cooling.

In addition to controlling the airflow and heater power, the LabVIEW VI was also tasked with data collection. For the purpose of this experiment, it was necessary to take measurements in a steady state condition where the temperatures of the heat sink and airflow were no longer changing under constant testing conditions. The approach to achieve this was to have the data logging be initiated by a trigger that monitors the rate of change for certain inputs that were desired to be steady (i.e. the heater base temperature TC05) and the flow velocity (p_{DYC}). This was accomplished by measuring the standard deviation averaged over the last 100 points over 10 seconds (100 samples/10 sps = 10 seconds). When the standard deviation fell below a target value, data recording was started. The program would record 10 seconds of data at 10 sps. After this was done, it would then cool the heat sink to 40 °C before executing its next test. It would do this for

as many testing conditions were input and then shut down. More information on determining what targets were adequate to achieve steady state is in section, 3.7.5.

3.7 Validation and Calibration

Before testing could begin, it was necessary to calibrate all the instrumentation used in the experiment as well as characterizing certain aspects of the test setup in order to ensure accurate operation of the wind tunnel that will yield reproducible results.

3.7.1 Pressure Sensors

A total of five sensors were used in this experiment: two for dynamic pressure, two for static pressure drop, and one for absolute pressure. All five sensors were purchased from Setra and were calibrated by the manufacturer. The results of the calibration are in APPENDIX E. The results of the calibration were used to generate linear regression equations for each of the pressure transducers. These equations were used to correct the voltage output from the sensor to the true pressure on the sensor diaphragm, within the LabVIEW VI. Also, the standard error of the regression equations was documented and used in the uncertainty analysis for the experiment (APPENDIX H).

3.7.2 Thermocouples

The thermocouples are Type-T probes purchased from Omega. They were calibrated by a resistive temperature detector (RTD) in a silicone oil bath. The calibration was performed in the range of temperature 0 – 150 °C. The details of this calibration are in APPENDIX F. The results of the calibration were used to generate linear regression equations for each of the 16 thermocouples. These equations were used to correct the thermocouple reading within the LabVIEW VI to the true temperature. This correction was made during the data recording process. The standard error of the regression equations was documented and used in the uncertainty analysis for the experiment (APPENDIX H).

3.7.3 Duct Air Flow Calibration

When using one Pitot tube for velocity measurement, it is important to make sure that the measured pressure at the Pitot tube location could be used to accurately represent the average dynamic pressure within the entire duct cross-section. If the Pitot tube is placed in the center of the duct, the measured velocity will be higher than the actual average velocity due to boundary layer effect on the velocity profile. Figure 3.27 shows that a boundary layer begins to form decreasing the velocity at the edges and increasing the velocity at the center. In the experiment, only the velocity at the center of the duct will be measured, it is important to establish a relationship between the centerline velocity and the average velocity over the experimental range of Reynolds number.

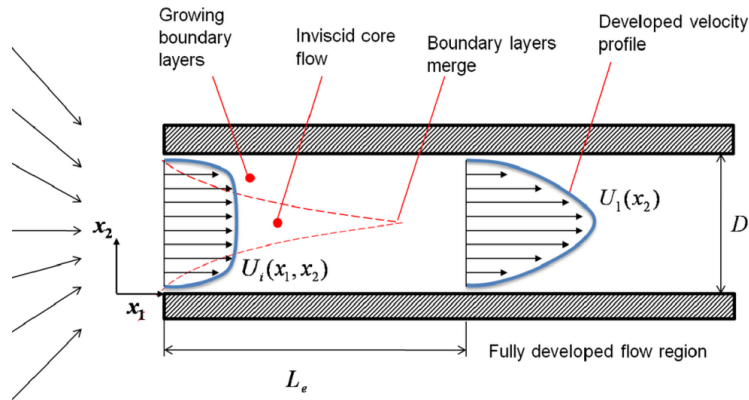


Figure 3.27 Developing Flow between Two Plates [21].

By generating a constant flow within the duct and moving the Pitot tube to different locations and recording the dynamic pressure, it is possible to know the velocity profile for that particular flow condition, thus the average velocity as well as the centerline velocity. To do this a 9 point, 3×3 , grid pattern was chosen. Figure 3.28 shows the location, in green dots, for the Pitot tube transverse measurement.

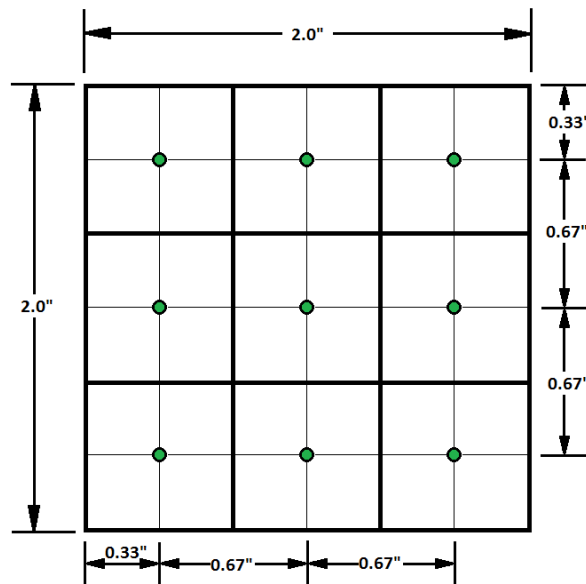


Figure 3.28. Location of Transverse Measurement Points within Duct Cross-Section

The next difficulty was how to conduct this measurement for all the flow conditions possible throughout this experiment (i.e. Reynolds number range). The experiment greatly varied in velocity and air pressure throughout testing, both of which affect the dynamic pressure reading. To mimic the changes to testing conditions for the transverse measurement using the vacuum chamber was not possible, on account of the fact that relocating the Pitot tube after each measurement would require the constant

opening and closing of the chamber door, making this process too time consuming. Instead, what was decided was to create a velocity profile for the entire range of Reynolds numbers used in the experiment. This was accomplished by conducting the calibration outside the chamber at ambient pressure for 823 feet ASL and only varying the velocity within the duct to achieve the desired Reynolds number. One adverse consequence of running this test at ambient pressure was that the velocity had to be very low in order to achieve the lower Reynolds numbers, much lower than if they were reached at higher altitude conditions. Because of this the test was limited by the ‘calibration limit’ of the dynamic pressure sensors. This limit was found to be near $Re \approx 1,500$ for the 0-0.1 inH₂O sensor. This was not ideal since the experiment would involve Reynolds numbers lower than 1,500. However, the test was still able to capture the transition from developing to fully developed flow. Since enough information was taken within the developing region above 1,500, a strong characterization for that region was developed and extrapolated to cover lower Reynolds number scenarios. The duct velocity corrections are shown in Figure 3.29.

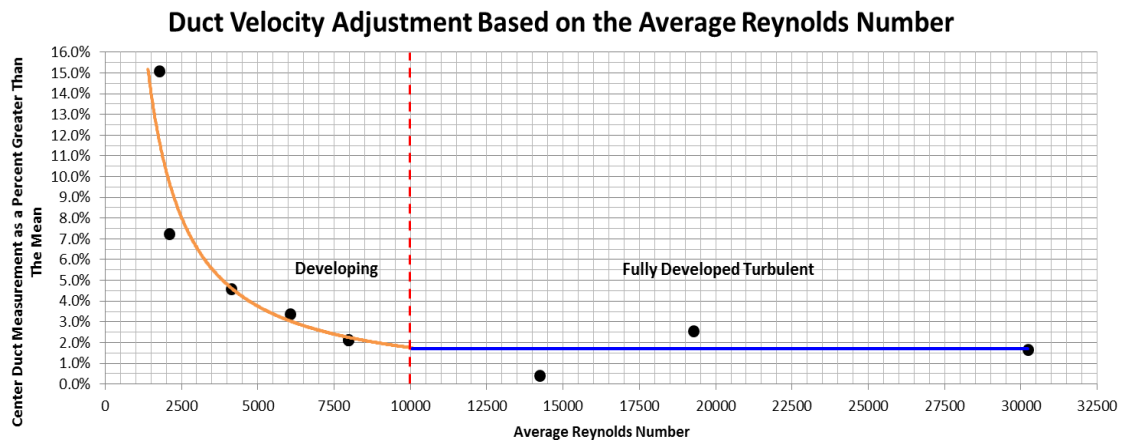


Figure 3.29 Air Velocity Correction Curve

This plot was created by measuring how much greater the center point Pitot tube measurement was than the average flow and plotting it as a function of the Reynolds number. This velocity correction curve was useful in understanding the condition of the flow within the duct for any given Reynolds number. More importantly it also quantifies the difference in the measurement taken by the Pitot tube at the center of the duct and the average velocity of the airflow. From Figure 3.29 two distinct curves immerge. The dotted red line at $Re = 10,000$ divides the developing flow curve and fully developed turbulent flow curve. The developing region was represented by a power curve best fit to the five measurements. The fully developed turbulent flow was represented by a zero slope line since boundary layer growth was minimized due to turbulence. The corrections in Figure 3.29 were used to derive the relationship between Reynolds number at the center point ($Re_{Duct,CP}$) and the average Reynolds number ($Re_{Duct,Avg}$), as shown in Equation 3-10 (developing) and Equation 3-11 (fully developed turbulent).

Equation 3-10

$$Re_{Duct,Avg} = \frac{Re_{Duct,CP} - 221.69}{0.99}; \quad Re_{Duct,CP} < 10,000$$

Equation 3-11

$$Re_{Duct,Avg} = \frac{Re_{Duct,CP} - 42.65}{1.02}; \quad Re_{Duct,CP} \geq 10,000$$

Equation 3-10 is mathematical correction for the center point Reynolds number to the true average, below $Re = 10,000$, for developing flow, and Equation 3-11 is the correction for the Reynolds numbers above 10,000 in turbulent fully developed flow. The corrections were used to correct the dynamic pressure measurements after each test.

3.7.4 Heater Power

The next calibration necessary for the operation of the experiment was for the measurement of power dissipation. This experiment uses two resistive thin film heaters. It was possible to measure the thermal energy by directly measuring the electrical energy dissipated through the resistors. The way to measure the power to the heater was to measure its resistance and record the current in the circuit for the heater. Its total resistance is measured to be $9.76 \, \Omega$. The current was measured using a calibrated shunt resistor, $0.0197 \, \Omega$. By measuring the voltage across the shunt, the total current flowing through the circuit was found. Since this current will be equal for all components within the closed circuit the power can be found from $P = I^2 R_e$. Doing a calibration of the entire circuit, from the shunt through the isolated amplifier and to the cRIO was the most accurate way to characterize this measurement. Figure 3.30 shows the circuit diagram for the calibration setup.

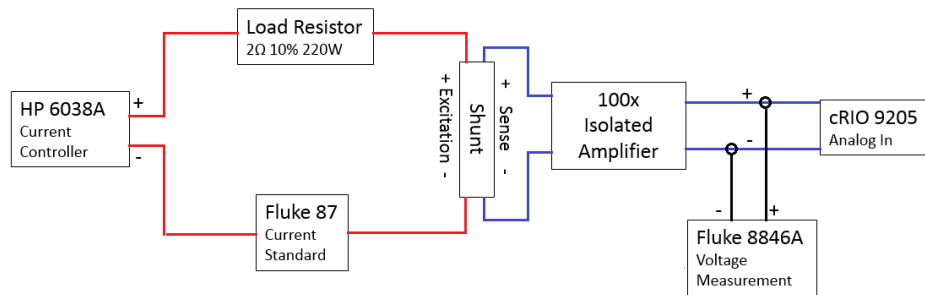


Figure 3.30 Wire Diagram for Shunt Current Measurement Calibration

The red wire circuit is the simulated power to the heater. A load resistor was used rather than the actual heater. A current controlled power supply provided the power and for reference, a Fluke 87 multimeter was used to monitor current. The blue wire was the current sensing circuit. It detected the voltage drop across the shunt and amplified it by a

factor of 100 before it was recorded by the cRIO. A Fluke 8846A multimeter was used to measure the voltage differential being recorded by the cRIO. By comparing the reading from the multimeter and the cRIO reading a correction was made within the LabVIEW VI so that it reflected the actual current of the load circuit. Figure 3.31 shows the results from this calibration.

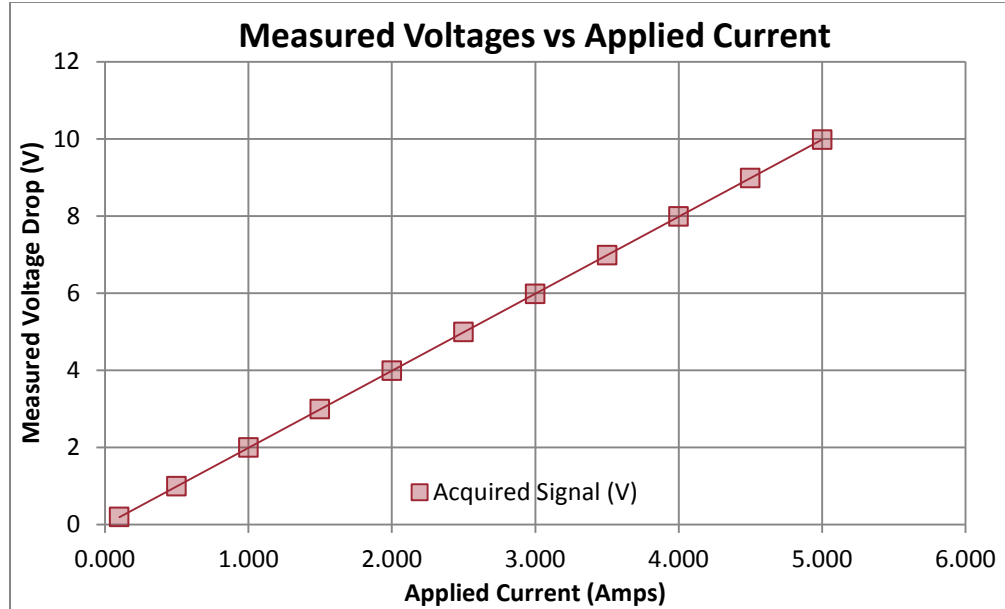


Figure 3.31 Shunt Current Calibration Regression Curve

A linear regression was performed to develop an equation of best fit, within the LabVIEW VI, that would translate the acquired voltage at the cRIO into current to the heater. Table 3-5 displays the results of the linear regression that was used within the LabVIEW VI, as well as the standard error that is used in the uncertainty analysis (APPENDIX H).

Table 3-5 Results from Linear Fit of Shunt Calibration

Curve Fit From Shunt Current Calibration	
Slope (Amps/VDC)	0.500542
Intercept (Amps)	0.003375
Standard Deviation (Amps)	0.001534
Standard Error (\pm Amps)	0.003065

3.7.5 Steady State Verification

A method was development to verify that a steady state condition has been achieved during the experiment and then to trigger data logging. As stated in section 3.6.2, the LabVIEW VI would calculate the standard deviation of the last 100 samples taken over 10 seconds for both air velocity and heat sink temperature. The calculation for

the running standard deviation is an equivalent metric to the rate of change of a measurement. If the SD of air velocity and heat sink temperature fell below a threshold then both could be considered steady state. The heat sink temperature steady state measurement used TC05. The air velocity steady state measurement used the dynamic pressure taken at the Pitot tube. Both standard deviation measurements were used to quantify the steady state condition of the system so that the program could repeatedly self-determine when to log data.

The next step was to determine what target standard deviation would be appropriate to signify that the system has reached steady state. If the target was too large, then data logging would be triggered before the system had truly reached steady state. If it was too small, the program may not trigger at all. To find the correct values for the target standard deviation, the following process was used. It began by selecting reasonable targets for the dynamic pressure and temperature, (Heater SD Target: 0.02, Dynamic Pressure SD Target: 0.0002). Four tests were run with these parameters and the results are shown in APPENDIX G. Two were run at 0.2 atm with high and low velocity and two were run at 0.8 atm with high and low velocity. This process was thought to give a good range representing the envelope of all testing conditions. The observations from these tests found that the standard deviation of the airflow needs to be relaxed for low altitude conditions (Target: 0.00025) and can be lowered for high altitude conditions (Target: 0.00015). This was due to the use of two different differential pressure sensors for the dynamic pressure measurement. Overall the airflow was able to reach and hold steady state significantly quicker than the heater temperature. In addition to this the heat sink temperature still appeared to have a slight slope during data recording. Therefore, further investigation into the heat sink temperature settling time is needed. To investigate this further it was necessary to study all of the thermocouple readings and determine their steadiness relative to the TC05 measurement. Figure 3.32 shows the results from an entire test run at 0.2 atm, with 0.0029 inH₂O dynamic Pressure, 40 W to the heater and having targets of: Heater SD Target = 0.015 °C; Flow SD Target = 0.00015 inH₂O. These conditions were the most extreme when considering settling time to reach steady state.

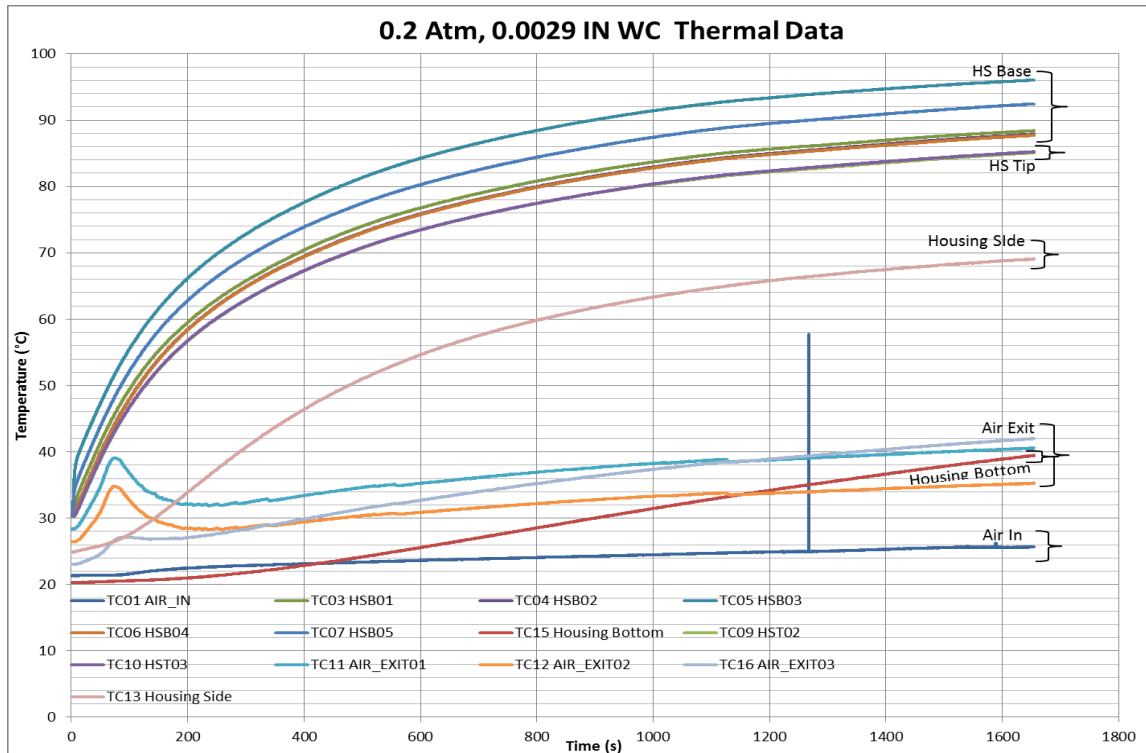


Figure 3.32 Temperature Measurements for Settling Time

The test runs from the initial start to when the target standard deviations are met and the data is logged. Table 3-6 displays the results from the logged data, showing the 100 point average, standard deviation and the slope.

Table 3-6 Temperature Measurements for Settling Time

	TC01 AIR_IN	TC02 AIR_IN	TC03 HSB01	TC04 HSB02	TC05 HSB03	TC06 HSB04	TC07 HSB05	TC15 Bottom	TC09 HST02	TC10 HST03	TC11 AIR_EXIT01	TC12 AIR_EXIT02	TC16 AIR_EXIT03	TC13 Side
AVG (°C)	25.67	25.69	88.44	87.92	96.07	87.75	92.49	39.54	85.14	85.27	40.65	35.32	42.06	69.11
STD DEV(°C)	0.0167	0.0164	0.0167	0.0187	0.0159	0.0220	0.0211	0.0369	0.0263	0.0261	0.0862	0.0707	0.0523	0.0232
Slope (°C/sec)	0.0015	0.0023	0.0033	0.0047	0.0037	0.0056	0.0061	0.0120	0.0079	0.0072	0.0254	0.0210	0.0162	0.0068

The slope was important in determining if the temperature of the heat sink was still increasing or had leveled off. A zero slope means it had reached steady state. As stated previously, because of noise, achieving a zero slope is not feasible. Therefore, it was desirable for the slope be as small as possible.

Table 3-6 shows that at every instance the slope was positive. This includes the air entering the heat sink. This means that the temperatures of the heat sink and ambient air were still rising. The explanation for this is that the environmental chamber was very close to an isolated system; therefore any thermal energy tends to remain within the chamber. Hence the temperature increases. The impact of this was that the slope of TC05

would never reach zero during a test. However, the slope of TC05 would approach zero relative to the increase in ambient temperature, which could also be considered steady state. The difference in the rate of change between TC05 and the air at inlet will be denoted as $\Delta\theta$. So, it was desirable to select the best target standard deviation that would yield a minimum $\Delta\theta$ and could be reasonably met. From Table 3-6, the difference in slope from the inlet air (average of TC01 and TC02) and TC05 was $\Delta\theta = 0.0018\text{ }^{\circ}\text{C}/\text{sec}$. So to verify that having a Heater SD Target of $0.015\text{ }^{\circ}\text{C}$ would be sufficient one final test was run with extended time to observe what, if any, improvements could be made to $\Delta\theta$. Three more tests were run to investigate how the temperature difference, of the heat sink base (TC05) and inlet air (TC01 & TC02), changes over a period of time after the target standard deviations have been met. Each test was run for about 200% of its normal settling time given the Heater SD Target of $0.015\text{ }^{\circ}\text{C}$. The results (APPENDIX G) from the extended time tests were compared with data from previous tests which used the conventional triggering method (Table 3-7)

In the far-right column is the recorded temperature difference for each test. By averaging the standard runs and subtracting it from the extended time run, a value for the increase in temperature difference over the extended test was found. For the two 0.8 atm tests, the difference is negligible. In the case of the 0.2 atm test the difference was somewhat significant. However, when viewed in the context of the additional time needed to observe this increase, the true impact on the experiment was minimal, $\sim 0.10\text{ }^{\circ}\text{C}/\text{min}$. Therefore, it was concluded that target standard deviation of $0.015\text{ }^{\circ}\text{C}$ for TC05 was satisfactory to use to allow the heat sink to reach steady state conditions.

Table 3-7 Comparison of the Temperature Difference for Extended Time Testing

Heater SD Target ($^{\circ}\text{C}$) - or - Additional Time after SD Target was met (min)	Pressure (atm)	Flow %	Mean Absolute Pressure (PSI)	Mean Dynamic Pressure (inH2O)	Mean Heater Power (inH2O)	Mean Delta T ($^{\circ}\text{C}$)
0.015	0.8	80%	11.55	0.10970	60.05	25.98
0.015	0.8	80%	11.47	0.10980	59.89	25.76
0.015	0.8	80%	11.49	0.10962	59.84	26.18
(Extended by 3:25)	0.8	80%	11.50	0.10986	59.83	25.94
Increase in Delta T over Extended test:						-0.03
0.015	0.8	40%	11.57	0.02707	59.86	38.91
0.015	0.8	40%	11.49	0.02777	59.70	37.54
0.015	0.8	40%	11.49	0.02722	59.66	38.74
(Extended by 6:40)	0.8	40%	11.50	0.02782	59.64	39.70
Increase in Delta T over Extended test:						1.30
0.015	0.2	40%	2.90	0.00281	39.44	68.52
0.015	0.2	40%	2.95	0.00295	39.40	66.28
(Extended by 27:20)	0.2	40%	2.89	0.00269	39.39	70.25
Increase in Delta T over Extended test:						2.85

By running the tests for additional time after the heater target was met, the amount of additional temperature rise could be observed. Since the results show that the temperature rise was negligible, it was determined that $SD < 0.015\text{ }^{\circ}\text{C}$ was a good target to signify heat sink had reached steady state.

3.8 Testing

The experiments were carried out closely following the test matrix outlined in section 3.5. Testing consisted of first verifying the experiment functionality and then sealing the chamber and taking it to the desired vacuum (i.e., altitude). Once the desired pressure was reached and observed to be stable (the chamber was not airtight and required a pump to be running at all times) testing began. At any given pressure, a total of 4-5 tests were done at varying heater power and flow velocity. Heater power inputs were mostly chosen conservatively to limit high temperatures. Velocities were chosen to cover a complete range of Reynolds numbers for each pressure condition. This was done by using the maximum velocity and incrementally reducing it by 20% for each subsequent test. In practice, this plan worked relatively well. However, some changes were made for specific velocities of some measurements. In some cases the maximum velocity was dictated by the fan speed. It was too strenuous for it to maintain high speeds, necessary for the target maximum of the test matrix, for long periods of time during some of the higher chamber pressures. This issue was thought to be caused by the added resistance at the exit of the wind tunnel created by its proximity to the walls of the environmental chamber. For this reason, the issue was not observed during the airflow validation process. The added resistance meant the fan would have to run at speeds higher than 25,000 RPM to hit its target velocity. Thus, the velocity targets for some cases were adjusted.

CHAPTER 4

EXPERIMENTAL RESULTS AND DISCUSSION

The experiment focused on the heat sink pressure drop, heat transfer coefficient, and predictions of these measurements. The predictions were derived from standard correlations. Additionally, the validity of these predictions was supported by accounting for heat loss through a thermal energy balance and experimental error through an uncertainty analysis. A discussion of the results is provided in this chapter.

4.1 Heat Transfer Coefficient

The primary measurement for this experiment was the heat transfer coefficient. The heat transfer coefficient for this heat sink was determined from the following relationship.

Equation 4-1

$$h_{avg} = \frac{Q_{Conv}}{A_{base}\Delta T_{base}}$$

where Q_{Conv} is the thermal energy transferred from the heat sink to the air, A_{base} is the area of the heat sink base, and ΔT_{base} is the temperature difference between the heat sink and air. However, it is more useful to study the HTC in its non-dimensional form, the Nusselt number, Nu (Equation 4-2). Presenting the heat transfer with the Nusselt number would make the results comparable to existing Nusselt number correlations.

Equation 4-2

$$Nu_{avg} = h_{avg} \frac{L^*}{k_{fluid}}$$

The Nusselt number is the average heat transfer coefficient multiplied by the characteristic length of the heat sink base (L^*) over the thermal conductivity of the fluid (k_{fluid}). The thermal conductivity was found using known thermo-physical properties of air. For simplicity, the heat sink was assumed to be at uniform temperature. To estimate this temperature, an average of five heat sink base measurements (TC03, TC04, TC05, TC06 & TC07) was averaged with an average of the heat sink fin tip temperatures, (TC09 & TC10). The estimate for the fluid temperature was found by taking an average of the two inlet air thermocouples (TC01 & TC02). The calculation for Q_{Conv} required a thermal energy balance.

4.1.1 Convective Thermal Energy Calculation

A thermal energy balance was used to calculate thermal energy imparted to the fluid through convection, by subtracting losses through conduction (Q_{Cond}) and radiation

(Q_{Rad}) from the electric power input to the heater. This began with the measurement for electrical power dissipation by the heater, (P_{Heater}). At steady state conditions, the electrical power to the heater was equal to the total thermal energy dissipated by the heat sink. Thermal energy was dissipated by the heat sink through convection, conduction, and radiation. Therefore, knowing the amount of energy transmitted to the fluid required estimates for the losses in energy through conduction and radiation. Equation 4-3 represents the energy balance and gives the convected thermal energy.

Equation 4-3

$$Q_{Conv} = P_{Heater} - (Q_{Cond} + Q_{Rad})$$

To find the losses due to conduction, an evaluation of the heat sink test section was performed. Figure 4.1 diagrams the primary surface to surface contact of the heat sink and heater to the polycarbonate housing. These areas were along the bottom through the fiberglass insulation and on the two sides of the heat sink.

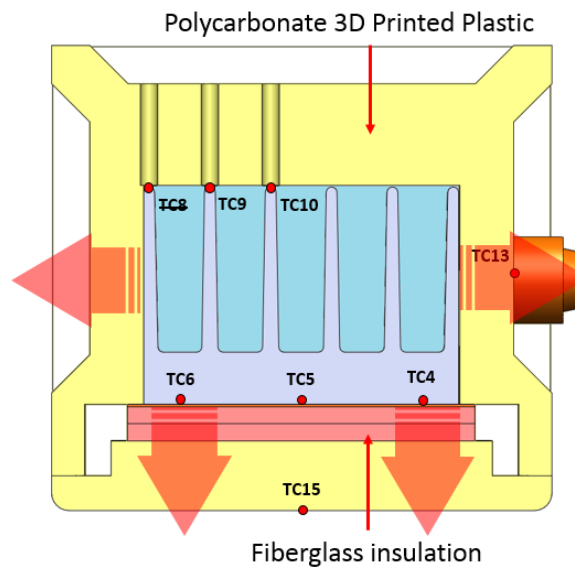


Figure 4.1 Thermal Energy Conduction Losses

The conductive thermal energy loss was estimated using one dimensional (1D) conduction. Equation 4-4 is the formula for estimating the 1D conduction losses from the heat sink into the housing. Measurements for the ΔT_{Side_HS} and ΔT_{Bottom_HS} were found using different averages for thermocouples near the surface in question. ΔT_{Bottom_HS} was from the difference of $T_{avg,Base}$ & TC15. The $T_{avg,Base}$ is simply the average of the five thermocouples imbedded in the base of the heat sink (TC03, TC04, TC05, TC06 & TC07). ΔT_{Side_HS} was the difference between $T_{avg_HS_Side}$ and TC13. The $T_{avg_HS_Side}$ was found using an average of the measurements of the two base side thermocouples (TC04 & TC06). This was then averaged with an average of the two thermocouple tip measurements (TC09 & TC10). The following equation was then formulated for Q_{cond} .

Equation 4-4

$$Q_{cond} = 2 \frac{\Delta T_{Side_HS}}{R_{t,Housing_Side}} + \frac{\Delta T_{Bottom_HS}}{R_{t,Housing_Bottom}}$$

Because of a limitation of available thermocouples only two TCs were used for the external temperature measurements. For the sides, TC13 was placed at the center of the conduction area. Because of symmetry the same temperature was expected to be on the alternate side of the heat sink. The same methodology was used for the bottom, by placing TC15 in the center of the base conduction area (Figure 4.1). Next, the thermal resistances for the bottom and sides will need to be computed.

Equation 4-5 and Equation 4-6 were used to calculate the thermal resistances of the housing side and bottom. The resistances were both sums of the material conduction resistance and conduction interface resistance.

Equation 4-5

$$R_{t,Housing_Side} = \frac{L_{Side}}{k_{PC}A_{HS_Side}} + \frac{1}{2h_{c,Side}A_{HS_Side}}$$

Equation 4-6

$$R_{t,Housing_Bottom} = 2 \frac{L_{FF}}{k_{FF}A_{HS_Bottom}} + \frac{L_{Bottom}}{k_{PC}A_{HS_Bottom}} + 3 \frac{1}{2h_{c,Bottom}A_{HS_Bottom}}$$

where L_{Side} is the thickness of the housing, k_{PC} is the thermal conductivity of the polycarbonate, and A_{HS_Side} is the contact area of the heat sink side to the housing. For the bottom of the heat sink, L_{FF} is the thickness of the Fiberfrax insulation, L_{Bottom} is the thickness bottom of the housing, A_{HS_Bottom} is the contact area for the bottom of the heat sink, and k_{FF} is the thermal conductivity of the Fiberfrax. To estimate the interface resistance a value for the interface conductance was needed. Of the interface between the aluminum heat sink and polycarbonate housing an aluminum to aluminum conductance [18] value was used for $h_{c,Side}$. Of the interface between the Kapton heater to Fiberfrax, Fiberfrax to Fiberfrax, and Fiberfrax to polycarbonate a single value of a ceramic to ceramic interface conductance [18] was used for $h_{c,Bottom}$.

Table 4-1 and Table 4-2 show the variables and results of the thermal resistance calculations. The housing side had a resistance of 5.98 ± 1.60 (m²K/W) and the housing bottom was found to be 72.36 ± 12.26 (m²K/W). The uncertainty of both calculations comes from variability of the values in Table 4-1 and Table 4-2 and was found using the methods detailed in APPENDIX H.

Table 4-1 Thermal Resistance Calculation for Housing Side

Material	Resistance Type	Thermal Conductivity (W/m-K)	Length (m)	Area (m ²)	Interface Conductance (W/m ² K)	Resistance (K/W)
		k	L	A _{HS_Side}	h _{c,Side}	R _t
Aluminum (AL)	Conduction	209	N/A	0.003		N/A
AL/PC	Interface			0.003	7100	0.02
Polycarbonate (PC)	Conduction	0.205	0.00787	0.003		5.95
Total Resistance (K/W), R _{t,Housing_Side}						5.98

Table 4-2 Thermal Resistance Calculation for Housing Bottom

Material	Resistance Type	Thermal Conductivity (W/m-K)	Length (m)	Area (m ²)	Conductance (W/m ² K)	Resistance (K/W)
		k	L	A _{HS_Bottom}	h _{c,Bottom}	R _t
Aluminum (AL)	Conduction	209	N/A	0.005		N/A
Al/Fiberfrax	Interface			0.005	1750	0.12
Fiberfrax (FF)	Conduction	0.0462	0.00635	0.005		29.38
Fiberfrax /Fiberfrax	Interface			0.005	1750	0.12
Fiberfrax (FF)	Conduction	0.0462	0.00635	0.005		29.38
Fiberfrax /PC	Interface			0.005	1750	0.12
Polycarbonate (PC)	Conduction	0.205	0.01270	0.005		13.24
Total Resistance (K/W), R _{t,Housing_Bottom}						72.36

The next loss contribution considered was the losses due to radiation, Q_{Rad} . As mentioned in Section 2.1, at high altitudes, radiation should not be ignored. The analysis of radiation heat transfer was carried out by dividing the surface of heat sink into two different parts, which could be easily computed. The first part of radiation exchange was the front and rear profiles of the heat sink (left side of Figure 4.2) with the ambient. The second part was surface to surface exchange from the area within the heat sink channels to the ceiling of the housing (right side of Figure 4.2).

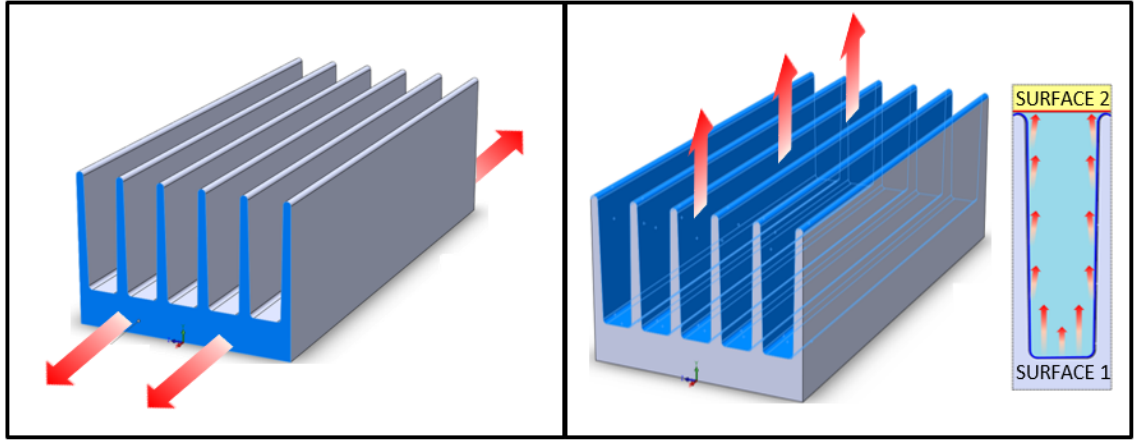


Figure 4.2 Heat Sink Radiation Surfaces

The radiation from the front and rear profiles was considered to be a radiation emitted to a blackbody (i.e., 100% absorption by the environment), since there was sufficient distance to any objects, reflection would be minimal. Equation 4-7 is for radiation thermal energy emission from the front and rear profiles.

Equation 4-7

$$Q_{r,p} = 2A_p\sigma\epsilon(T_s^4 - T_{amb}^4)$$

Here, A_p is one of the transmitting surface area, σ is Stefan-Boltzmann Constant (5.6704×10^{-8}), ϵ is the emissivity of unfinished aluminum (0.04-0.07) [18], T_s is the heat sink average surface temperature and T_{amb} is the temperature of the ambient environment. T_{amb} was estimated using the inlet air temperature measurement.

Figure 4.2 (right) shows the emitting area of the heat sink channels. This calculation was slightly more complex than that of the profile radiation. Because of the proximity of the channels to the ceiling of the housing this needed treated as a radiation exchange between two surfaces. To simplify the calculation, the exchange from one heat sink channel surface was evaluated and then multiplied by the five channels to get the total exchange. Equation 4-8 is for radiation exchange between two surfaces.

Equation 4-8

$$Q_{1-2} = \frac{\sigma(T_1^4 - T_2^4)}{\frac{1 - \epsilon_1}{\epsilon_1 A_1} + \frac{1}{A_1 F_{1-2}} + \frac{1 - \epsilon_2}{\epsilon_2 A_2}}$$

The subscript 1 denotes a property of the aluminum heat sink single channel and the subscript 2 denotes the properties of the polycarbonate housing viewed by the channel. Here, the heat sink surface temperature, T_1 , has already been computed. The housing temperature was estimated by an average of the inlet air (TC01 & TC02) and the exit air temperature (TC11, TC 12 & TC16). In the denominator of Equation 4-8, there

are three terms representing the radiation resistance. The areas A_1 & A_2 were measured using the CAD model of the heat sink. The emissivity of the polycarbonate was estimated to be 0.84. The view factor of surface 1 to 2, A_1F_{1-2} , was simplified. Working backwards, the view factor from the flat surface of the housing to the aluminum channel (F_{2-1}) only sees the aluminum and therefore 100% of its radiation is transmitted to the aluminum (i.e., $F_{2-1} = 1$). Because of the relationship, $A_1F_{1-2} = A_2F_{2-1}$, A_1F_{1-2} was simplified to be represented as A_2 . Therefore, the resistance simplifies to Equation 4-9.

Equation 4-9

$$R_s = \frac{1 - \varepsilon_1}{\varepsilon_1 A_1} + \frac{1}{A_2} + \frac{1 - \varepsilon_2}{\varepsilon_2 A_2}$$

Throughout the entire experiment, the losses from any given test averaged $\sim 2.18 \pm 0.96$ W. This varied with altitude as well, with more losses at higher altitude and less at lower altitude.

4.1.2 Nusselt Number

After calculating the convective heat transfer from the heater to the passing fluid the Nusselt number, as a function of Reynolds number, could be found through Equation 4-2. Figure 4.3 shows the experimental results. Error bars were added based on the uncertainty of measurements. For details of how the uncertainty was calculated refer to APPENDIX H.

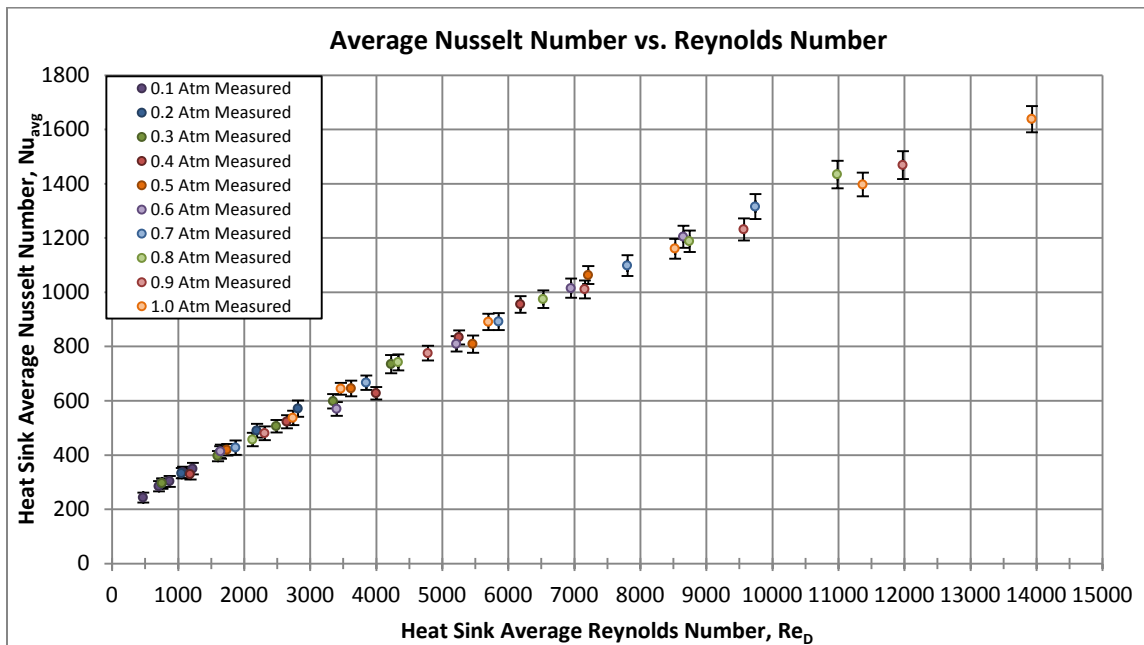


Figure 4.3 Measured Nusselt Number vs. Reynolds Number at Various Altitude Pressure

Figure 4.3 shows each individual test taken for different atmospheric pressures denoted by the different colors in the legend. It is clear that although multiple tests were run at various pressures, ranging from 1.0 - 0.1 atm, the Nusselt number for each pressure falls within a single curve. Therefore, the conclusion can be made that the Nusselt number is independent of fluid pressure or density, and it is only a function of Reynolds number.

4.1.3 Nusselt Number Flat Plate Correlation

It was useful to evaluate accepted methods for predicting the Nusselt Number and compare them against the measurements taken. The first comparison was done on flat plate laminar flow correlation. Predicting a heat sink's performance based on this correlation is a widely accepted practice in industry.

Equation 4-10 [18]

$$Nu_L = 0.664Re_L^{1/2}Pr^{1/3}; \quad \text{Laminar, Average, } T_f, 0.6 \lesssim Pr \lesssim 50$$

This correlation is for the average Nusselt number of a flat plate with parallel laminar flow. The Reynolds number (Re_L) is based on the length scale of the flat plate. To extend this correlation to a parallel plate heat sink surface with heat transfer enhancement feature, an efficiency (ϵ_0) was applied to the thermal resistance of the heat sink surface, to represent the surface enhancement.

Equation 4-11

$$R_{t,HS} = \frac{1}{\epsilon_0 A_{base} h_L}$$

Therefore, the correlation for the enhanced surface becomes:

Equation 4-12

$$Nu_{avg} = Nu_L \epsilon_0 \left(\frac{A_{wet}}{W_{HS} L^*} \right)$$

where A_{wet} is the total area of the heat sink surface in contact with the air flow and W_{HS} is the length of the heat sink along the direction of the flow. The efficiency ϵ_0 was determined from a correlation for predicting the surface efficiency of a fin array [18] shown in the following equation.

Equation 4-13 [18]

$$\epsilon_0 = 1 - \frac{NA_{fin}}{A_{wet}} (1 - \epsilon_f)$$

where A_{fin} is the area of a single fin, N is the number of fins, and ϵ_f is the efficiency of a single fin. ϵ_f is estimated by the following equation.

Equation 4-14 [18]

$$\epsilon_f = \frac{\tanh mL_c}{mL_c}$$

where mL_c is a correlation for estimating the temperature distribution within the heat sink cross section ($A_{HS_Profile}$).

Equation 4-15 [18]

$$mL_c = \left(\frac{2h_{AL}}{k_{AL}A_{HS_Profile}} \right)^{1/2} L_c^{3/2}$$

This helps tailor the correlation for different surface enhancements. Figure 4.4 is Equation 4-12 against the experimental data. It is clear that this predictive method falls short of characterizing the experimental observations. There are several reasons for this. The first being disagreement of the actual intent of this correlation and the experimental setup.

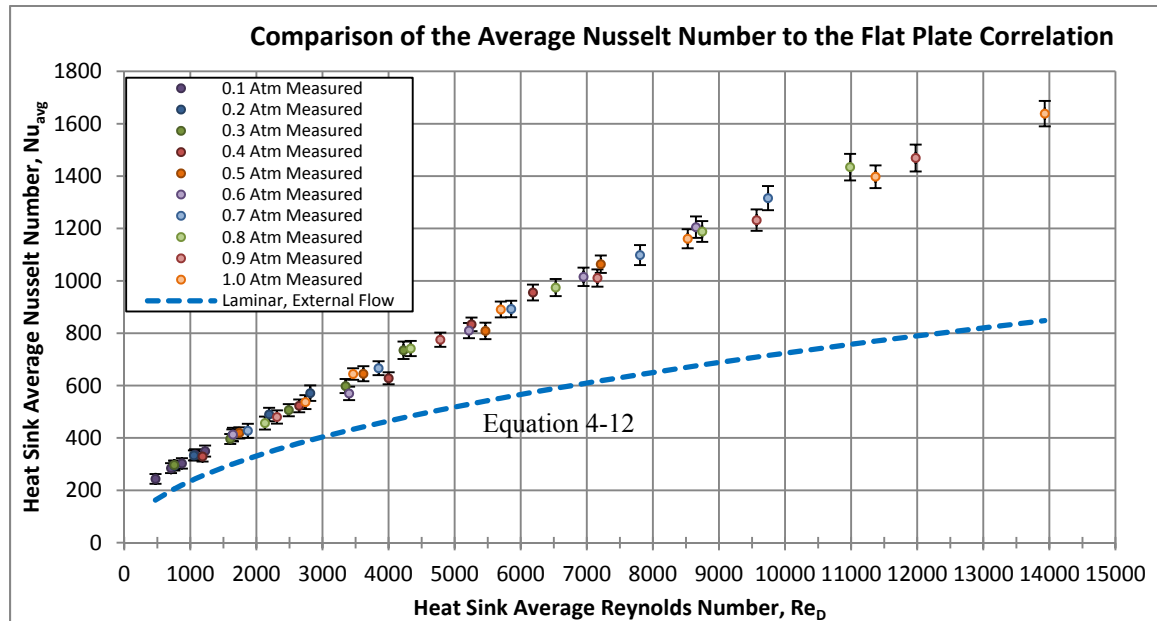


Figure 4.4 Comparison of the Average Nusselt Number of Flat Plate Correlation vs. Test Data

The application of this correlation is really meant for a heat sink within a free flowing fluid. The experiment, by design, did not allow free flow over the heat sink but instead forces the fluid through the HS channels, eliminating any bypass air. In a free stream a large portion of the air passing by the heat sink will take the path of least resistance passing over the heat sink geometry. Although this correlation is not applicable to this setup it does offer insight into the performance difference between external flow forced convection and confined no bypass, or internal flow.

It is clear from the comparison of this correlation to the observed test results in Figure 4.4 that the channeled flow shown as test data has much higher heat transfer performance than external flow shown in the correlation curve. This is because for a bypass air TMS the air will take the path of least resistance and tend to pass over the heat sink rather than through the channels. Another observation is that higher Reynolds number flow will have a higher percentage of bypassed air resulting in larger difference in Nusselt number.

4.1.4 Nusselt Number Internal Flow Correlation

The next method of prediction was internal flow correlation which is more applicable to the experiments. Several correlations exist for describing the heat transfer between the channel wall and the fluid flowing through it and the appropriate form depends on the Reynolds number of the flow within the channel.

If the flow is laminar, then its Reynolds number (Re_D) is below 2,300. In the instance of laminar flow, special care must be taken to account for the thermal boundary layer growth as a result of heat transfer at the surface of the heat sink, decreasing the HTC. Figure 4.5 shows dependency of the local Nusselt number to thermodynamically developing laminar flow.

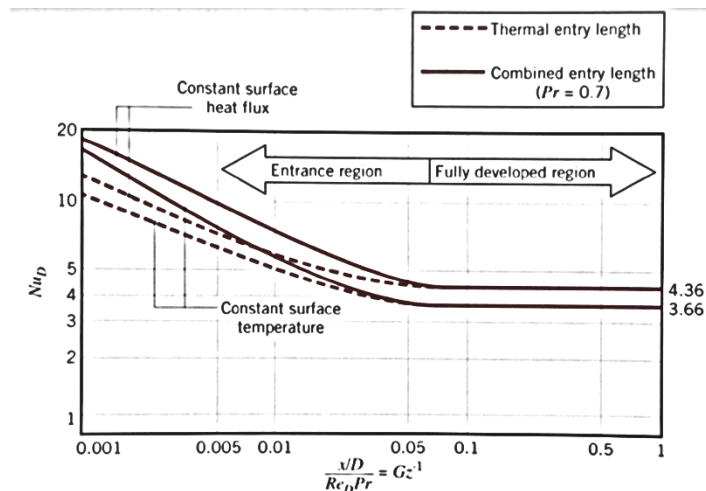


Figure 4.5 Local Nusselt Number Thermal Development [18]

At the thermal entry region of a flow within a channel the Nusselt number can be 4-5 times higher than it is after it has become fully developed. The length of the thermal developing region is a function of the Reynolds number, Prandtl number and, diameter ($\frac{x}{D_H} = \frac{Re Pr}{20}$). In addition to the thermal boundary layer, there also exists a hydrodynamic boundary layer. The length of the hydrodynamic entry region is a function of the Reynolds number, and diameter ($\frac{x}{D_H} = \frac{Re}{20}$). The hydrodynamic boundary layer propagates from the channel walls and grows larger within the duct cross-section, for

laminar flow. This further decreases HTC by slowing down the motion of the fluid at the channel surface. Both the thermal and hydrodynamic boundary layers were developing within the channels but their impact on the overall heat transfer was less at lower Reynolds number due to the decrease length of the developing region. The correlation detailed in Equation 4-16 [18] is for internal laminar flow with a combined entry region both thermal and hydrodynamic developing.

Equation 4-16 [18]

$$Nu_D = 1.86 \left(\frac{Re_D Pr}{L/D_H} \right)^{1/3} \left(\frac{\mu}{\mu_s} \right)^{0.14}; \quad Re_D = \frac{D_H \cdot U_\infty}{\nu} < 2,300$$

For flow that was not laminar ($Re > 4,000$) a turbulent correlation was needed. For a fully developed turbulent flow within a channel the presence of a thermal boundary layer has less of impact on the heat transfer than with laminar flow. This is due to the decreased size of the boundary layer for a fully developed turbulent flow. The boundary layer is confined to the area at the surface of the duct walls. However, just like with laminar flow, at the entry region of the heat sink the fluid is not hydrodynamically fully developed. The length of the hydrodynamic entry region is a function of the hydraulic diameter only ($\frac{x}{D_H} \approx 10$). With $\frac{x}{D_H} = 9.5$ the flow through the channels never reached fully developed turbulent during this experiment. Unfortunately, correlations for predicting the Nusselt number within the entry region of a developing turbulent flow are not as prevalent. In the absence of the desired correlation, the Nusselt number for a fully developed turbulent flow was used. The correlation expressed in Equation 4-17 is a well-supported correlation for the average Nusselt number of turbulent, fully developed flow.

Equation 4-17 [18]

$$Nu_D = 0.023 Re^{4/5} Pr^{0.3}; \quad Re_D \geq 10,000$$

Figure 4.6 is a comparison of the measured average Nusselt number with that of correlative predictions for the Nusselt number in internal laminar flow having combined entry region (Equation 4-16 [18]) and in fully developed internal turbulent flow (Equation 4-17 [18]).

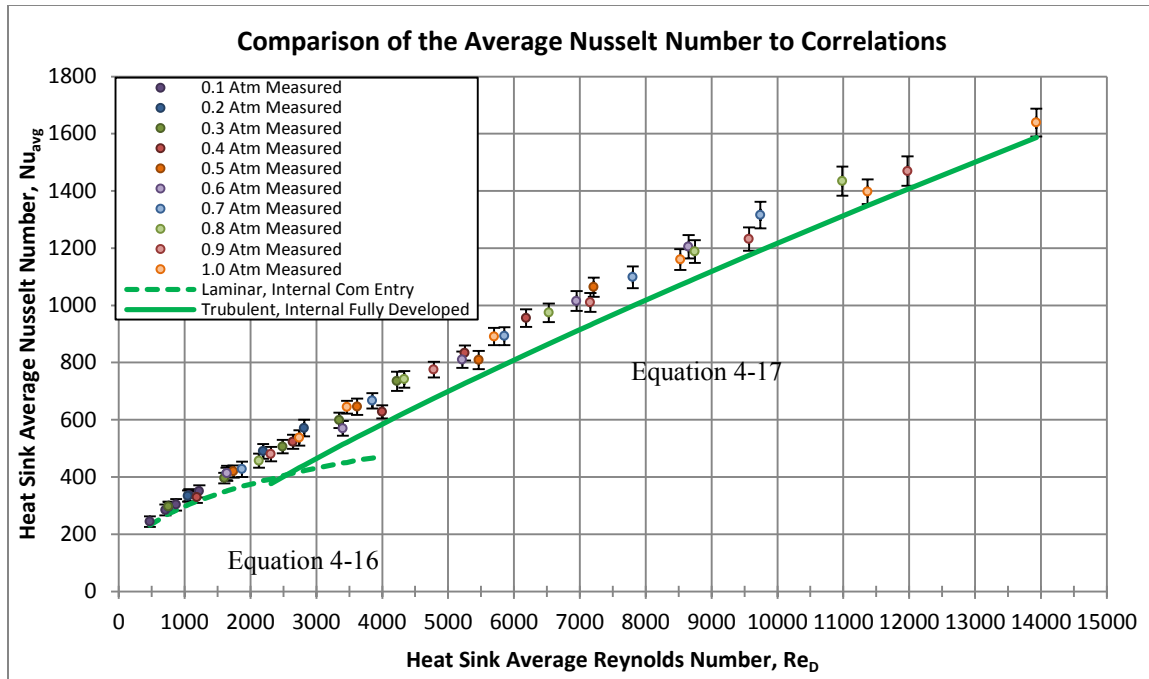


Figure 4.6 Comparison of the Average Nusselt Number and Internal Flow Correlations

Figure 4.6 shows that Equation 4-17 [18] has better agreement with the measured data than that of Equation 4-16, for their applicable range. Equation 4-17 follows the measured values reasonably well with exception of Reynolds number below 10,000, as expected. Below Reynolds number 1,500 Equation 4-16 describes the measurements well.

4.2 Pressure Loss

The next focus of the results and discussion is the pressure loss over the heat sink. Theoretically the pressure loss is related to HTC and may be used to describe the performance of a heat sink. However, knowledge of the pressure loss can be used to size both heat sink and fan.

For this experiment the measurement of the pressure loss was made directly, by two static pressure taps before and after the heat sink and a single differential pressure sensor. It is useful to study this measurement using the non-dimensional pressure loss coefficient η . This is done by dividing the static pressure loss by the average fluid momentum term, $\frac{1}{2}\rho U_{HS}^2$.

Equation 4-18

$$\eta = \frac{\Delta P_{Stc}}{\left(\frac{1}{2}\rho U_{HS}^2\right)}$$

Figure 4.7 shows the independence of the pressure loss coefficient and density when plotted against Reynolds number. An uncertainty analysis was conducted and error bars were added to Figure 4.7. The error of this measurement is relatively small except for at low Reynolds numbers. A more complete description of the uncertainty analysis is in APPENDIX H.

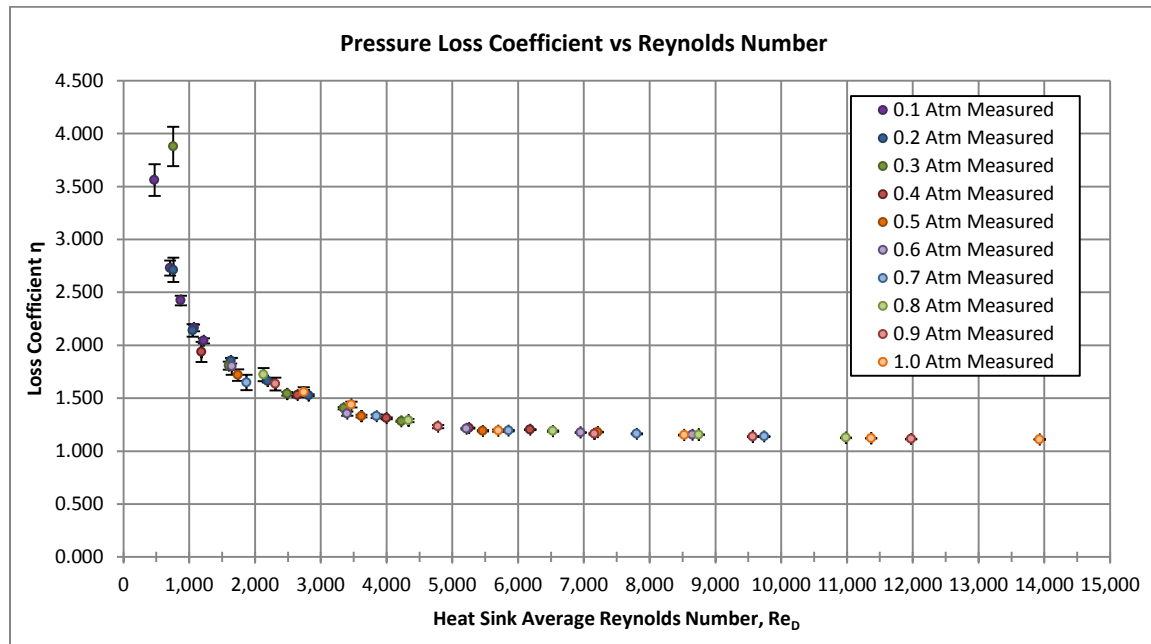


Figure 4.7. Comparison of the Pressure Loss Coefficient at Different Pressure

It is useful to compare the measured results with correlations for the pressure loss coefficient.

4.2.1 Internal Flow Friction Factor Correlation

The typical approach to predicting the pressure loss over a given geometry, such as this, is to use a correlation that has been established to describe the loss given the course of the airflow and mode of pressure loss. For instance there are two types of losses taking place that contribute to the total static pressure loss across the heat sink, the major and minor losses. The minor losses are from changes to the cross-sectional area of the flow, such as enlargements or contractions. In the case of the heat sink, there was a minor loss for the abrupt contraction in cross-sectional area at the entrance to the heat sink, shown in Equation 4-19 and a loss associated with the rapid expansion in cross-sectional area at the exit of the heat sink, shown in Equation 4-20.

Equation 4-19

$$\text{Sudden Contraction; } \eta_{Minor} = 0.42 \left(1 - \frac{D_1^2}{D_2^2} \right)^1 = 0.221$$

Equation 4-20

$$\text{Sudden Expansion; } \eta_{Minor} = \left(1 - \frac{D_1^2}{D_2^2}\right)^2 = 0.276$$

The minor loss coefficient from the sudden contraction, Equation 4-19, and sudden expansion, Equation 4-20, is entirely geometry dependent and therefore will remain constant throughout the entire range of air velocity tested.

Unlike the minor losses, the major losses are dependent on the velocity of the flow. Correlations for predicting the major loss is shown in Equation 4-21 where the friction factor, f , is Reynolds number dependent.

Equation 4-21

$$\eta_{Major} = f \frac{L}{D_{Hy}}$$

Two correlations for the friction factor were chosen. Both are well established correlations. Equation 4-22 [18] [17] is for laminar fully developed flow and Equation 4-23 [18] is for fully developed turbulent flow.

Equation 4-22 [18] [17]

$$f = \frac{64}{Re_D}; \quad Re_D < 3,000$$

Equation 4-23 [18]

$$f = 0.316 Re_D^{-1/4}; \quad 2,300 \lesssim Re_D \lesssim 20,000$$

A comparison of these two correlations to the measured results is presented in Figure 4.8.

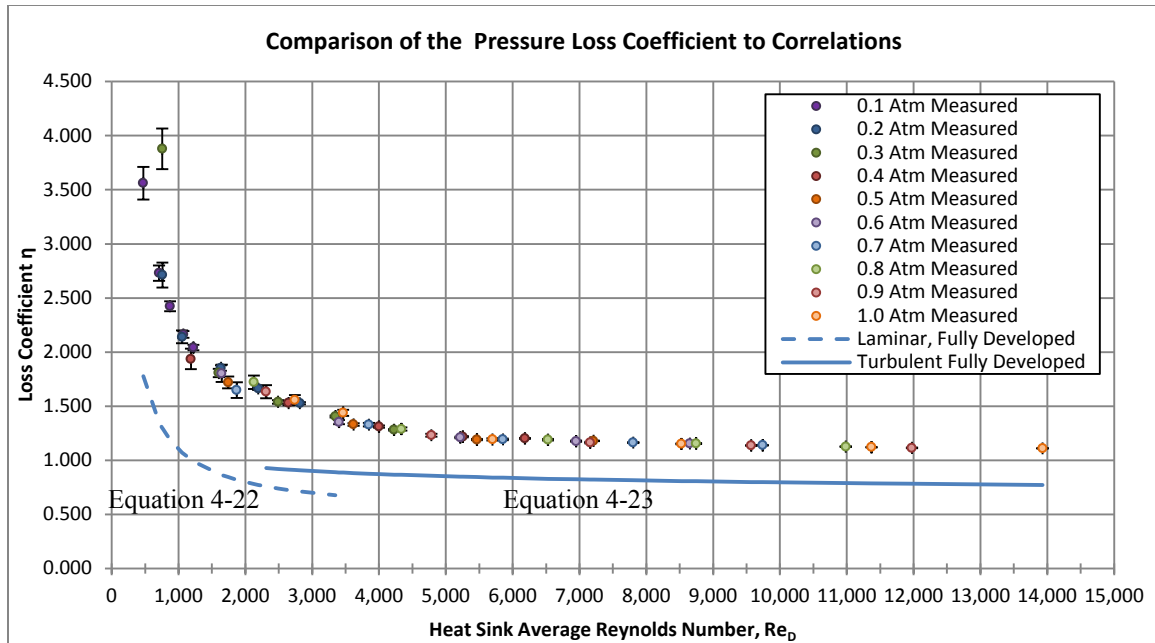


Figure 4.8 Comparison of the Pressure Loss Coefficient: Measurement vs Correlation

The most obvious observation from this chart is the apparent failure of the fully developed laminar flow correlation to predict the loss coefficient. The disagreement here is profound enough to be considered unusable for this application. There are two possible contributions for the disagreements observed: the major loss correlation under-predicts the loss coefficient or the approximations for the minor losses under-predict the losses. Since the minor loss prediction method remains constant throughout all cases, an under-prediction of this would simply mean a negative offset of the curve. This could be the case since the curve for the measured losses in the laminar region fit the same arc as the correlation. Another explanation for this can be found when comparing the intended use of the minor loss approximation to the case of this experiment. The intent of the approximation is meant for the simpler situation of a circular pipe of certain diameter suddenly experiencing a change in that diameter. It does not necessarily account for complex geometry within the flow path (i.e., heat sink). The other explanation for the disagreement would be the correlation for the friction factor. This possibility is explored further in the next section, where an enhanced method of adapting the friction factor for a parallel plate heat sink is explored.

4.2.2 Friction Factor Simons Method

A paper by Simons [20], details an analytical method for predicting the pressure drop across a parallel plate heat sink. The method is similar to the previously outlined procedure of summing the major and minor losses. The computation for the minor losses is identical to the process in Section 4.2.1. The only difference is how the major loss is found. Therefore, by exploring Simons method a better understanding was achieved on the shortcomings of the previous predictive methods. In other words, answer to the question, is the issue with the minor or major loss prediction, would be found.

Simons method takes an already existing friction factor correlation, like the one detailed by Equation 4-22, and uses it to build an ‘apparent friction factor,’ f_{app} for the entire heat sink major loss, shown in Equation 4-24.

Equation 4-24

$$f_{app} = \frac{\left[\left(\frac{3.44}{\sqrt{L^*}} \right)^2 + (f_{fit} \times Re_D)^2 \right]^{1/2}}{Re_D}; \quad Re_D \lesssim 2,300(est)$$

The apparent friction factor uses the characteristic length of the heat sink (L^*), the average Reynolds number through the channel, and a friction factor fitted (f_{fit}) to a fifth order polynomial, shown in Equation 4-25. Note that the equation is only applicable in the hydrodynamically developing laminar flow. The upper limit for Re_D in Equation 4-24 was estimated based on the experimental data within the paper.

Equation 4-25

$$f_{fit} = \frac{24 - 32.5f + 46.7f^2 - 40.8f^3 + 23f^4 - 6.1f^5}{Re_D}$$

The apparent friction factor is related to the total pressure loss coefficient through the following equation.

Equation 4-26

$$\eta_{Total} = \sum \eta_{Minor} + 4f_{app} \frac{L}{D_H}$$

Figure 4.9 is the comparison of Simons correlation against experimental measurement. It is observed that the Simons method for the major losses in a parallel plate heat sink yield much better results than using the correlations of Equation 4-22 and Equation 4-23.

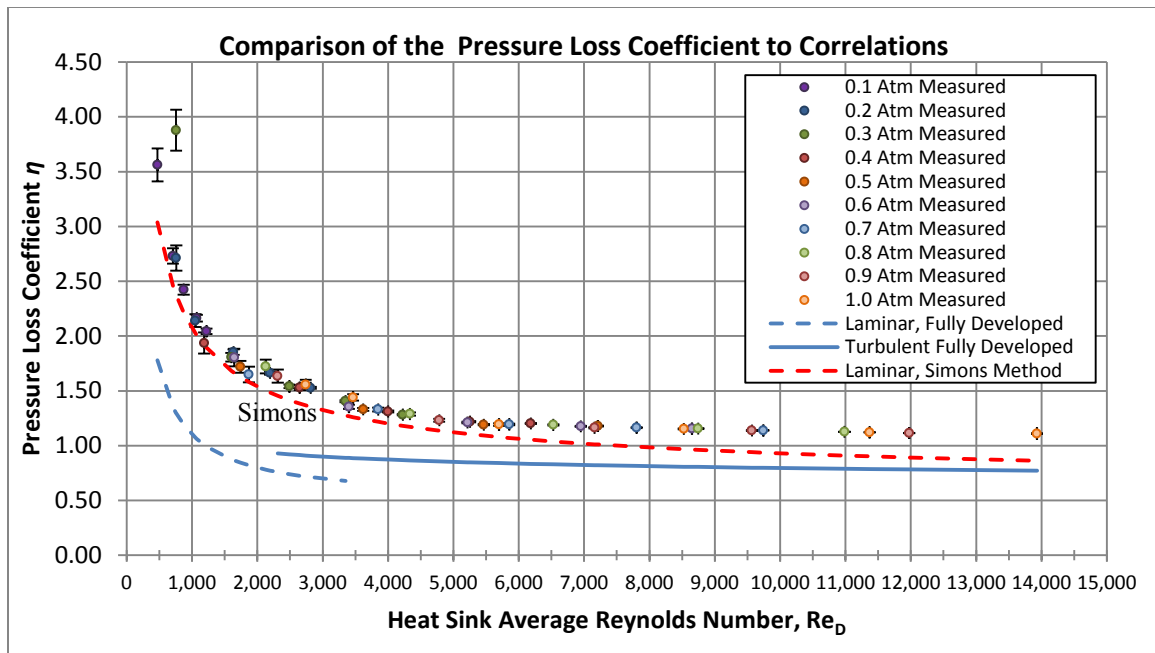


Figure 4.9 Comparison of the Pressure Loss Coefficient for the Simons Method

Figure 4.9 offers insight to explaining the disagreement with other predictive methods. Since all three methods use the same calculation for the minor losses, and the Simons method is able to accurately predict the measured results, then the disagreement must be due to the major loss calculation and therefore the friction factor. This further supports the conclusion that correlations for a fully developed flow, laminar or turbulent, cannot be used to describe accurately losses for a hydrodynamically developing entry region.

Another observation from Figure 4.9 is that although the Simons method, developed only for hydrodynamically developing laminar flow, works well to predict the loss coefficient above $Re_D = 2,300$. In Figure 4.9 the curve for the Simons method prediction was extended to a Reynolds number range beyond its defined applicability. This was done to illustrate the advantage the method has over the fully developed turbulent friction factor correlation (Equation 4-23) as well as the fully developed laminar correlation (Equation 4-22).

CHAPTER 5

CONCLUSION AND FUTURE WORK RECOMMENDATION

5.1 Conclusion

There are several important conclusions from this thesis. The findings from the literature review highlighted the importance of fully understanding the forced convective heat transfer coefficient at high altitudes. This thesis proposed a method to experimentally measure the Nusselt number and pressure loss coefficient by constructing a wind tunnel to operate within an altitude chamber.

The results confirm that, for altitudes from sea level to 52,000 feet, the Nusselt number and pressure loss coefficient can be determined from experimental measurement, numerical simulation and suitable correlations obtained at sea level. Both quantities are functions of Reynolds number only. Although these results were not unexpected, they now serve to validate predictive methods of heat transfer.

In addition to measuring the Nusselt number and pressure loss coefficient at high altitude, an effort was made to evaluate basic methods of predicting these properties, through correlation. There were several key findings from this investigation. The first was the entrance effect enhanced heat transfer but increased pressure drop at the same time. For both measurements the correlations under-predicted the observed data. The primary reason was due to the fact that the flow within the heat sink channels went through a thermally and hydrodynamically developing regime, while the correlations assume a fully developed flow. Additionally, there are no useful correlations that can accurately predict the Nusselt number in the transition region from laminar to turbulent flow. Within the range of Reynolds numbers tested (500-14,000) the flow exists in both laminar and turbulent regimes. This is of interest to the design of an EMAS thermal management system using forced convection, as it would likely experience this transition within the flight envelope. Lastly, the traditional laminar flow correlation for the friction factor under predicts the pressure loss for this experiment whereas the Simons method is more accurate because of the entrance effect and complex geometry. The Simons method is also more accurate in predicting the pressure drop for Reynolds numbers greater than 2,300. However, this is not a general use method and only applies parallel plate heat sinks with no bypass air.

Finally, it was clear that directing the air stream through only the channels of the heat sink, eliminating bypass flow, had significant higher heat transfer over an external flow situation. Based performance difference observed between the data and flat plate correlation, a recommendation can be made that for any future aircraft TMS use a no bypass solution.

5.2 Future Work Recommendation

The setup chosen for this experiment was meant to closely emulate an aircraft EMAS cooling system. Therefore, any pitfalls uncovered to this method of cooling would directly relate to problems for an aircraft system. Additionally, this approach provides a good catalyst to direct future work within the field.

The first recommendation to come from this research would be the development of a better correlation that takes into account the entrance effect. For any TMS of this type the airflow will go through both a thermal and hydrodynamic developing state. In order for a correlation to be useful, in predicting performance, it needs to take this effect into account.

Another recommendation would be to focus research on the development of optimized thermal management solution for the range of Reynolds numbers across the flight envelope. Further research can be conducted to verify if any methods for heat transfer surface enhancement are equally effective across the flight envelope.

BIBLIOGRAPHY

- [1] A. K. Hyder, "A Century of Aerospace Electrical Power Technology," *JOURNAL OF PROPULSION AND POWER*, vol. 19, no. 6, pp. 1155-1179, November - December 2003.
- [2] D. Bar-Shalom, "Altitude Effects on Heat Transfer Processes In Aircraft Electronic Equipment Cooling," Massachusetts Institute of Technology, 1989.
- [3] FedBizOps.Gov, "Integrated Vehicle Energy Technology (INVENT) Development Program for the 6th Generation Energy Optimized Aircraft (EOA)," June 2009. [Online]. Available: <https://www.fbo.gov>.
- [4] J. Rosero, J. Ortega, E. Albada and L. Romeral, "Moving Towards a More Electric Aircraft," *IEEE A&E Systems Magazine*, pp. 3-9, 2007.
- [5] S. C. Jensen, "Flight Test Experience with an Electromechanical Actuator on The F-18 Systems Research Aircraft," NASA Dryden Flight Research Center, Edwards, CA, 1998.
- [6] I. Moir and A. Seabridge, Aircraft Systems; Mechanical, Electrical and Avionics subsystems integration, West Sussex, England: Wiley, 2008.
- [7] NASA, "U.S. Standard Atmosphere (NASA-TM-X-74335)," U.S. Government Printing Office, Washington, D.C., 1976.
- [8] Wikipedia, "U.S. Standard Atmosphere," [Online]. Available: https://en.wikipedia.org/wiki/U.S._Standard_Atmosphere. [Accessed 15 October 2015].
- [9] C. L. Belady, "Design Considerations for Air Cooling Electronic Systems in High

- Altitude Conditions," *TRANSACTIONS ON COMPONENTS, PACKAGING, AND MANUFACTURING TECHNOLOGY-PART A*, vol. 19, no. 4, DECEMBER 1996.
- [10] H. Wong, "Experimental Investigation of Air Cooling Electronics at High Altitudes," Arizona State University, 1999.
- [11] H. Wong and R. E. Peck, "Experimental Evaluation of Air-Cooling Electronics at High Altitudes," *Journal of Electronic Packaging*, vol. 123, pp. 356-365, December 2001.
- [12] G. Xu, "Thermal Performance Prediction for High Power Processors at High Altitude," in *2004 ASME International Mechanical Engineering Congress and Exposition*, Orlando, FL, 2005.
- [13] EPAC Software Inc., "COLDPLATE Report, Fan Cooling at High Altitude," [Online]. Available: EPAC-INC.com. [Accessed Jan 2014].
- [14] Y.-R. Lin, W. Wu and L. C. Chow, "Fan Performance Characteristics at Various Rotational Speeds and Ambient Pressures," *SAE Technical Paper 2014-01-2219*, no. doi:10.4271/2014-01-2219, 2014.
- [15] AMCA - Air Movement and Control Association, AMCA 210: Laboratory Methods of Testing Fans for Aerodynamic Performance Ratings, Air Movement and Control Association International, Inc and American Society of Heating, Refrigeration and Air Conditioning Engineering, Inc, 2000.
- [16] Dwyer Instruments, "AirVelocityIntroduction," Dwyer Instruments, [Online]. Available: <http://www.dwyer-inst.com/Products/AirVelocityIntroduction.cfm>. [Accessed 20 August 2015].

- [17] J. A. Roberson and C. T. Crowe, Engineering Fluid Mechanics, Third ed., Boston, Massachusetts: Houghton Mifflin Company, 1985.
- [18] F. P. Incropera and D. P. DeWitt, Fundamentals of Heat and Mass Transfer, 5th ed., Hoboken, NJ: John Wiley & Sons, 2002.
- [19] M. A. Gonzalez Hernandez, A. I. Moreno Lopez, A. A. Jarzabek, J. M. Perales Perales, Y. Wu and S. Xiaoxiao, "Design Methodology for a Quick and Low Cost Wind Tunnel," InTech, 2013.
- [20] R. E. Simons, "Estimating Parallel Plate-Fin Heat Sink Thermal Resistance," *Electronics Cooling*, vol. 9, no. 1, pp. 8-9, 2003.
- [21] Alsirajmamun, "File:IF2 me.png," [Online]. Available: https://upload.wikimedia.org/wikiversity/en/0/00/IF2_me.png. [Accessed 26 October 2015].
- [22] American Society of Heating, Refrigeration, and Air-Conditioning Engineers, Inc (ASHRAE), 2009 ASHRAE Handbook – Fundamentals, American Society of Heating, Refrigeration, and Air-Conditioning Engineers, Inc, 2009.
- [23] B. & J. A. V. Lindgren, "Design and Evaluation of a Low-Speed Wind-Tunnel with Expanding Corners," Technical Reports from Royal Institute of Technology Department of Mechanics, SE-100 44 Stockholm, Sweden, 2002.
- [24] Biscarri Simulation, "openALYA tutorials 1.0," 21 2 2015. [Online]. Available: http://www.biscarri.cat/openALYA_tutorials/case_elbow.html. [Accessed 29 September 2015].
- [25] L. B. C. a. M. J. Cattafesta, "Fundamentals of Wind-Tunnel Design," in

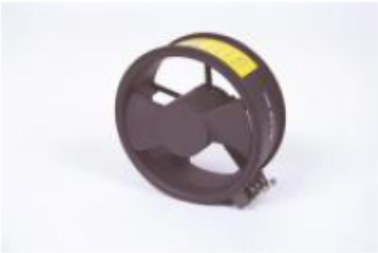
APPENDIX A
FAN SPEC SHEET



Tubeaxial Fans - Propimax 2L 3715SF

MADE IN THE USA

Part Number	011858000
Unit Description	PX2L_028MCDL,S,3715SF
Airflow (CFM)	119
Pressure Shutoff (IWG)	3.29
Line Voltage (DC)	28
Phase/Frequency (Hz)	N/A
Capacitor (µF)	N/A
Power (Watts)	35.672
Run Current (Amps)	1.30
Locked Rotor (Amps)	0
RPM	19,500
Weight (lbs/kg)	0.6 / 0.2
DBA at 3 feet	75
Max Ambient Temp (°C)	85



Description

The Propimax 2 brushless DC fan is an axially compact tubeaxial fan and is equipped with an aerodynamic venturi configured case. Utilizing the unique Rotron inverted motor construction the axial length of the fan is limited to the minimum measurement required by the highly efficient 2-blade propeller, and the internal or external drive electronics.

Accessories:

- Low Speed Warning Detector
- Air Flow Switch
- Finger Guard

Construction

The venturi case and propeller are cast aluminum. Rotron's unique inverted motor rotorprop impeller stainless steel shaft runs on two high-precision (ABEC 5), double-shielded, stainless steel ball bearings with an integral lubricant reservoir to give longer maintenance-free life. Brushless DC drive electronics circuitry is mounted in an external module.

Environmental Resistance Guide

Designed to meet MIL-STD-810C

Altitude	Method 500.1, pr I
Acceleration	Method 513.2
Vibration	Method 514.2
Shock	Method 516.2
Salt Fog	Method 509.1
Rain	Method 506.1
Fungus	Method 508.1
Humidity	Method 507.1, pr I, II, III
Explos. Atm.	Method 511.1, pr I

For specifics, please contact the factory.

Life Expectancy

Contact AMETEK Rotron for specific ratings. Rotron rates life expectancy in hours L10 or MTBF at a given ambient temperature. This is the time at which 90%, for L10, and 50%, for MTBF, of an available test lot are still operating.

Woodstock, N.Y. USA (P) 845-679-2401 (F) - 845-679-1870 (email) milinquiry@ametek.com

NOTES:

EST. NEW LAB REF. FAN
E2900-7201. THIS TEST 26 VDC.
P/N 011850000, S/N: 108092223

Date: 3-23-09

Bench: N3P-20-1

Flow: L ☐ R ☐

RPM 19669

Line Amps 1.18

Locked Amps ---

Watts ---

MOTOR

Series 3715SF

Type ECDC

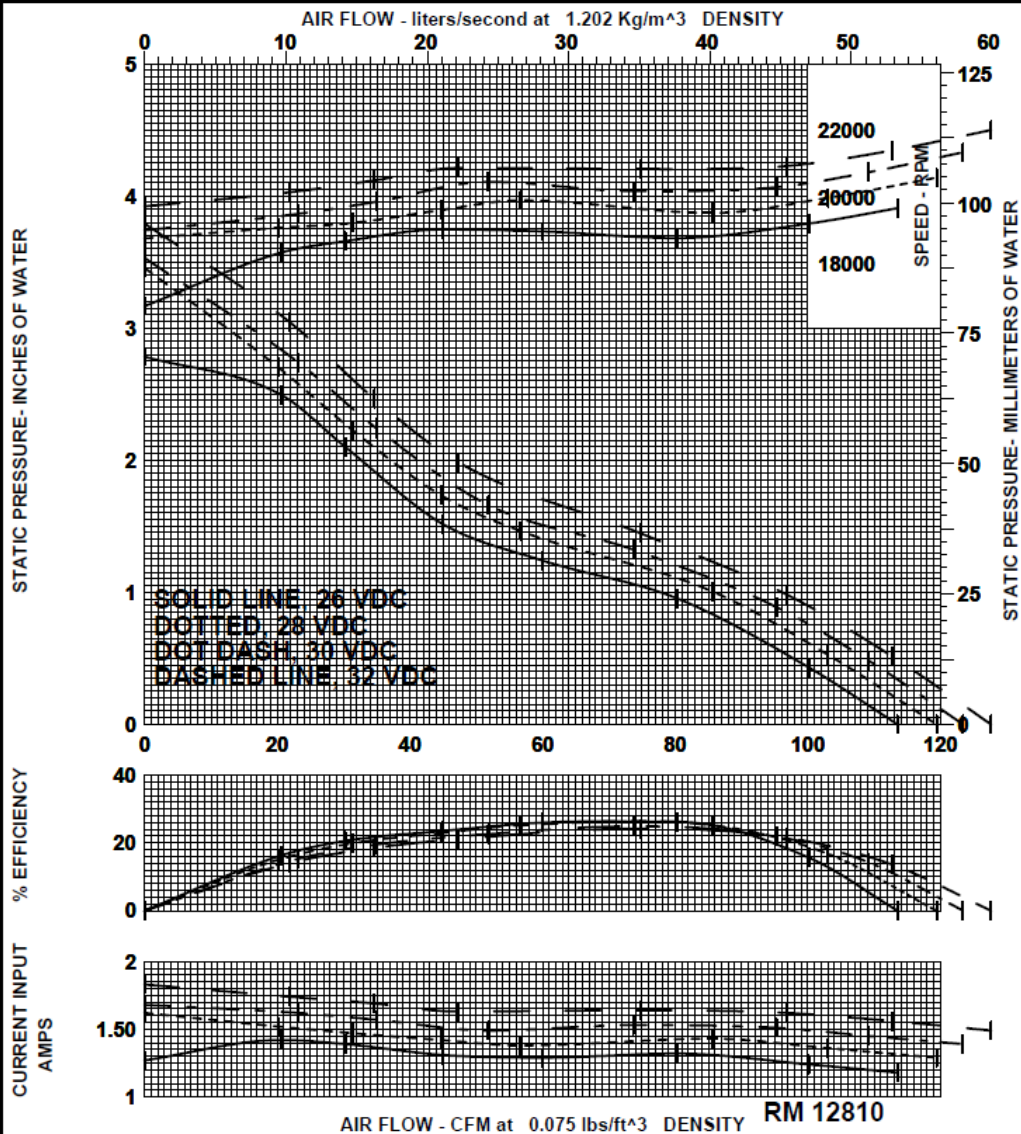
Volts 26

Wave DC

Phase DC

Hertz ---

MFD ---



APPENDIX B

WIND TUNNEL MINOR LOSS CALCULATIONS

The losses from changes in cross-sectional area of the duct were looked at first. This instance has two situations that result in a cross-sectional area change; increase or decrease. The increase in cross-sectional area is known as an expansion and a decrease in cross-sectional area is known as a contraction. The minor losses for these are computed differently where the magnitude of loss is dependent on the rate (contraction ratio: N & expansion/contraction angles α and β) at which the change develops. If the rate is high enough to be considered an almost instantaneous change in cross-sectional area then the pressure losses associated with the abrupt change would be at a maximum. Wind tunnel design avoids these high pressure loss situations. However, in some cases this could not be avoided, therefore it was necessary to calculate their contributing loss. But first it was necessary to understand the other contributing factors to the minor losses.

Equation B - 1 [19]

$$p_{minor\ loss} = \eta \left(\frac{\rho U_{\infty}^2}{2} \right)$$

For each case where a minor loss occurred, $p_{minor\ loss}$ (Equation B - 1) was used. This value is dependent on the flow velocity U_{∞} and the loss coefficient η . In the instance of an abrupt change in duct cross-sectional area the loss coefficient can be found for either a sudden enlargement (Equation B - 2) or sudden contraction (Equation B - 3).

Equation B - 2 [19]

$$\eta = \left(1 - \frac{D_1^2}{D_2^2} \right)^2$$

Equation B - 3 [19]

$$\eta = 0.5 \left(1 - \frac{D_1^2}{D_2^2} \right)^1$$

For these two equations D represents the diameter, or hydraulic diameter in the case of a non-circular pipe. The subscripts 1 & 2 represent the diameter of the pipe before and after the cross-sectional area change.

For situations involving gradual change, the equation for estimating the loss coefficient is somewhat more complex. For the cases of a controlled enlargement, Equation B - 4 was used and for a controlled contraction Equation B - 5 was used.

Equation B - 4

$$\eta = 4.0 \times \tan \frac{\alpha}{2} \times \sqrt[4]{\tan \frac{\alpha}{2}} \left(1 - \frac{A_1}{A_2} \right)^2 + \eta_f$$

Equation B - 5

$$\eta = \left\{ \frac{\lambda}{16 \sin \frac{\alpha}{2}} \right\} \left(1 - \frac{1}{N^2} \right) - \left\{ \frac{\lambda}{16 \sin \frac{\beta}{2}} \right\} \left(1 - \frac{1}{N^2} \right)$$

The loss coefficient is affected by the contraction ratio or expansion angle [19]. Figure B. 1 shows the dimensions of a controlled expansion.

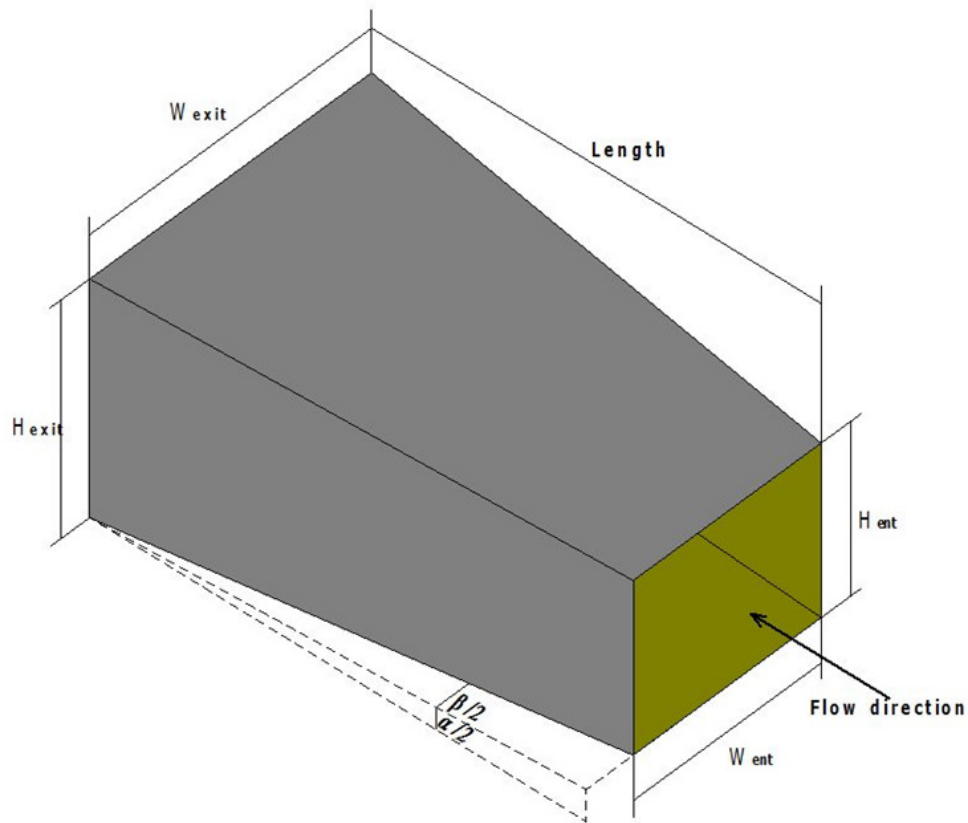


Figure B. 1 Wind Tunnel Diffuser Section [19]

The controlled enlargement or diffuser section is best optimized by keeping the expansion angle, α , below 3.5° . This ensures that the flow does not detach from the sides of the wind tunnel during expansion. However, in the instances where this feature was used (See Figure 3.10: Sections; 4-5 & 21-22) there was not enough length available to follow this guideline. The effect of not adhering to this rule is minimal since neither section takes place within the flow conditioning or measuring area (See Figure 3.10: Sections; 7-21). Instead, the geometry was shaped to best fill the available space and used continuous curves to smooth the transition. The pressure loss was computed using

Equation B - 4. The other relevant variables needed were the area before transition A_1 , and after A_2 as well as the additional loss factor η_f .

Equation B - 6 shows the calculation for a controlled contraction.

Equation B - 6

$$\eta_f = \frac{0.02}{8 \sin \alpha/2} \left[1 - \left(\frac{A_1}{A_2} \right)^2 \right]$$

In the case of a controlled contraction, this experiment used three (See Figure 3.10: Sections; 1-2, 7-8 & 17-18), two were in the conditioning and measurement portions of the wind tunnel. Figure B. 2 shows the concept of a controlled contraction section with angles α and β . Of the two sections within the flow conditioning sections only one could be optimized to have minimal pressure loss.

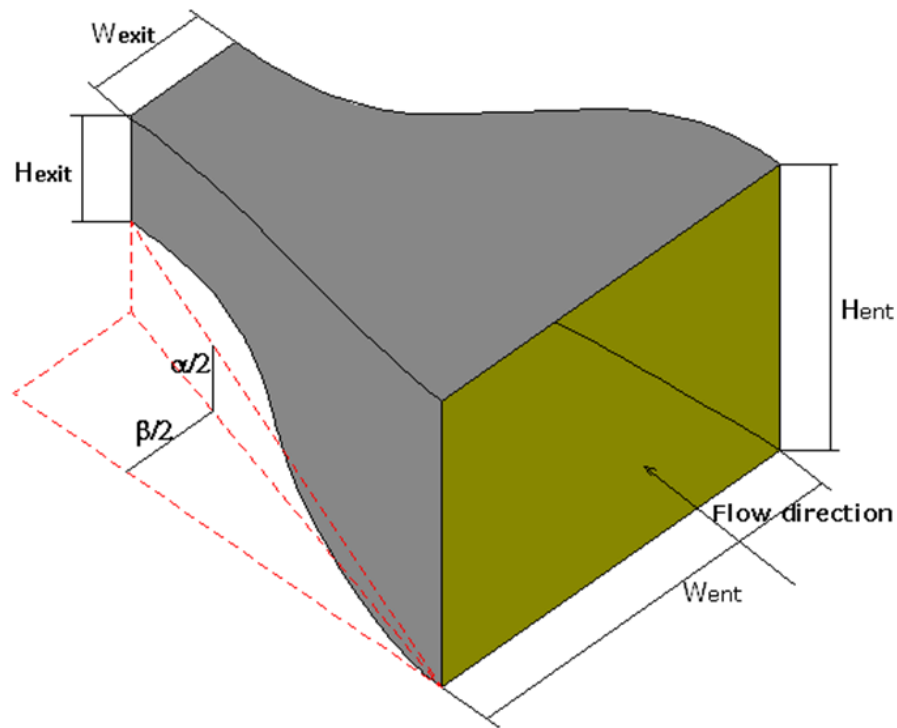


Figure B. 2 Wind Tunnel Contraction Section [19]

This was the section immediately after the fan, Section 7-8. Since the contraction ratio, N , was already fixed the contraction angle could be changed by altering the length over which the contraction takes place.

Once the design of these sections was complete it was time to move on to the other elements of loss inside the wind tunnel. Three corners in total were used for this wind tunnel (See Figure 3.10, Sections; 5-6, 11-12 & 13-14). Several solutions were

considered. Figure B. 3 shows types of ducting bends as classified by *American Society of Heating, Refrigeration, and Air-Conditioning Engineers, Inc* [22].

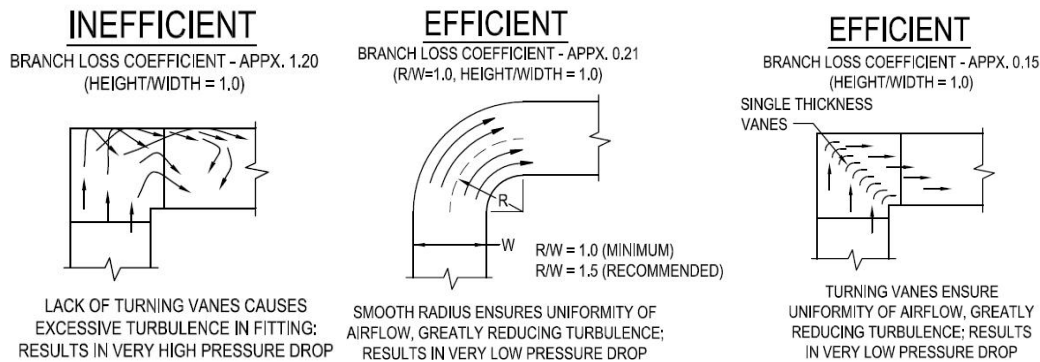


Figure B. 3 (Left) Expanding Corner; (Middle) Constant Diameter Corner; (Right) Expanding Corner with Turning Vanes [22]

Two of these corners result in a comparatively low pressure drop. Both the constant diameter corner and the expanding corner with turning vanes were used within the wind tunnel. However, the expanding corner offers a better method for minimizing the size of the bend, thus allowing for a longer straight section before the Pitot tube measurement. Figure B. 4 shows the concept design of an expanding corner with turning vanes.

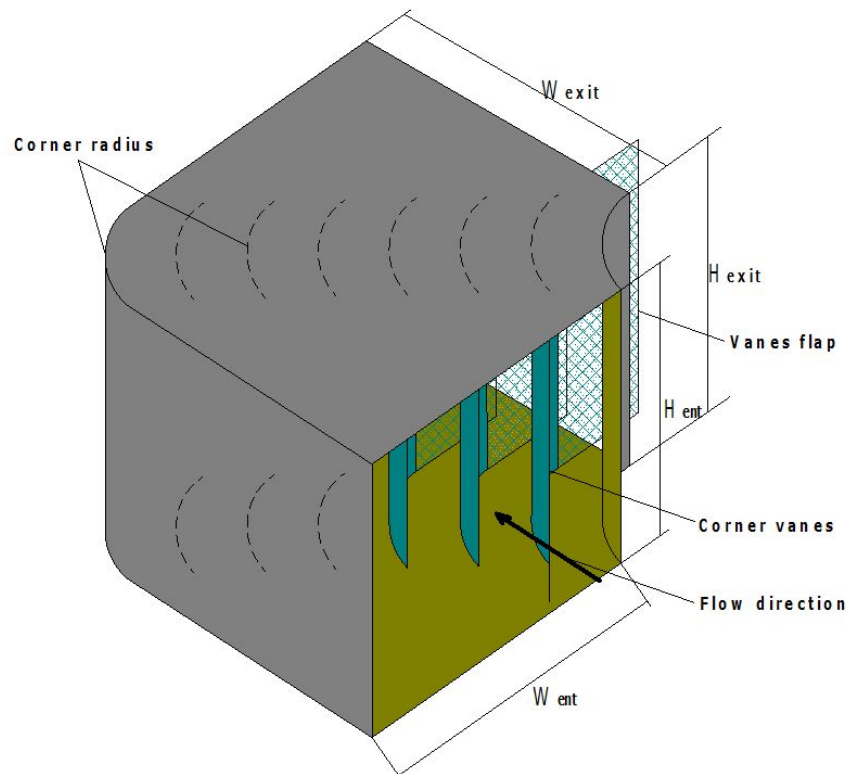


Figure B. 4 Concept Design, Expanding Corner with Turning Vanes.

The relevant dimensions are the corner radius r , entrance width W_{ent} , entrance height H_{ent} , and the number of turning vanes N as well as the size of the vanes. The entrance height and width were identical to the exit height and width, and since these were dependent on the duct size, will both be equal to 2.0". The number of vanes (N) for each corner were found using the following relationship shown in Equation B - 7.

Equation B - 7

$$N = 1.4 \times \frac{d}{c}$$

It was important to have the fewest number of vanes needed to adequately turn the flow, as they added friction losses. The amount of vanes was dependent on the chord length of the vanes c , and the length of the diagonal d . The chord length is dependent on the design of the individual vanes, including their camber. Therefore, it was possible to select the number of vanes based on selecting a corner radius. Figure B. 5 shows how these dimensions were gathered.

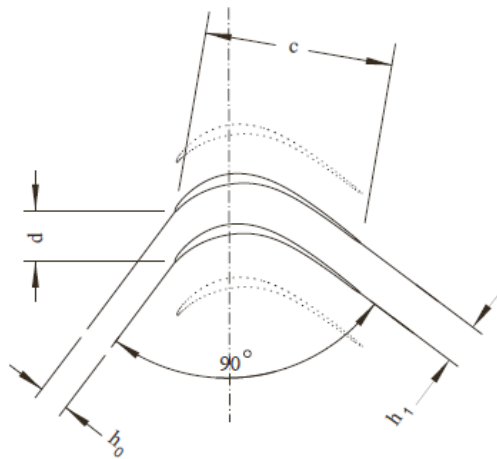


Figure B. 5 Geometry of Guide Vanes to a 90° Expanding Corner [23]

The camber for the corner was chosen to be 0.5 inches as this represented a quarter of the duct width. From this perimeter the number of vanes then becomes four, which allows for the calculation of the pressure loss for the expanding corner.

Equation B - 8 shows the calculation for the loss coefficient associated with an expanding corner, where η_M is an additional loss based on the ratio $\frac{r}{W_{ent}}$, which for 0.25, η_M becomes 0.17 [19].

Equation B - 8

$$\eta = \eta_M + 0.02 + 0.31 \times \frac{r}{W_{ent}}$$

The loss coefficient for the third, constant diameter corner, was found by a less involved process. Not only was this portion of the wind tunnel before the fan and not within the test section it also had the largest hydraulic diameter and therefore the lowest velocity. Because of this, the loss within the corner was low compared to other parts of the duct. Figure B. 6 shows the relationship between the size of the elbow and the pressure dropped by the bend.

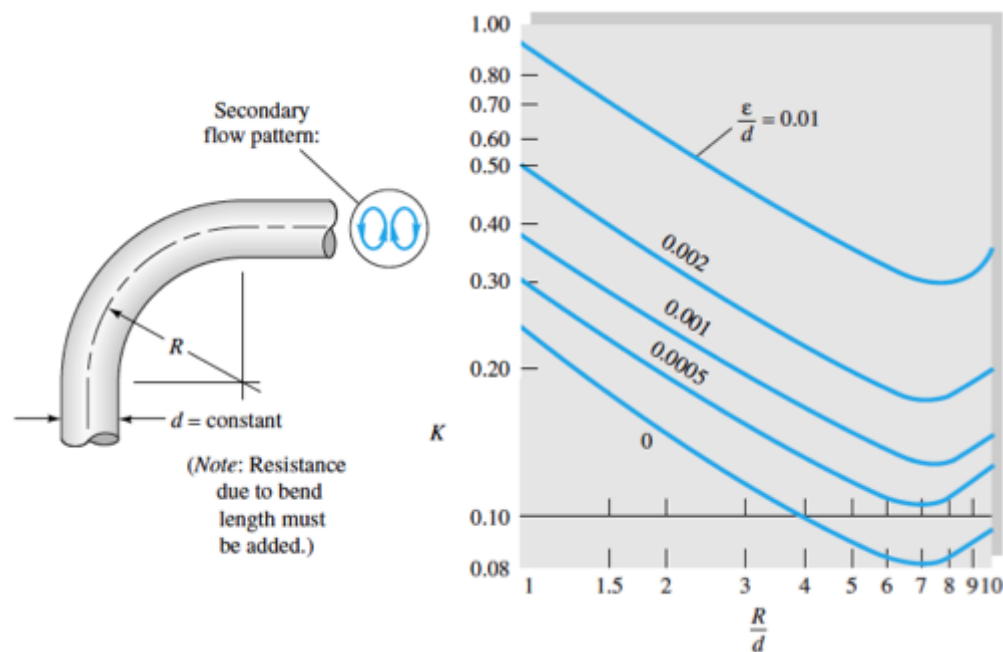


Figure B. 6 Constant Diameter Corner Loss Coefficient Estimation [24]

The multiple curves in Figure B. 6 are for varying surface roughness for the walls inside of the corner. A conservative estimate for the roughness was chosen (0.001) which for an R/d ratio of 1.3 gives a loss coefficient of 0.35.

The next elements of the wind tunnel that needed to be designed and their pressure losses computed were the two honeycomb type flow conditioners (See Figure 3.10, Sections; 9-10 & 15-16). The purpose of these features was to eliminate any large-scale transverse turbulence in the flow and align it with the desired direction within the duct for development [25]. Each of the two flow conditioners served a necessary purpose within this wind tunnel design. The first was to eliminate any rotational motion or 'swirl' imparted onto the flow from the fan before it enters the first corner. The second honeycomb was to eliminate transverse turbulences in the flow after having traveled through two 90° corners. It also helped transition it into a fully developed state necessary for the dynamic pressure measurement by the Pitot tube. The sizing of these elements was based on the diameter of the duct. The pressure loss of the honeycomb was found using the computation for a sudden contraction (Equation B - 2) followed by a sudden enlargement (Equation B - 3).

Figure B. 7 shows a page from the AMCA publication, Laboratory Methods of Testing Fans for Aerodynamic Performance Ratings [15]. It shows the guidelines in selecting the length and cell size for a honeycomb type flow straightener. Thus a honeycomb size that fit the requirements of this duct, a 1.0 in. long honeycomb with 1/8 in. cell size was purchased.

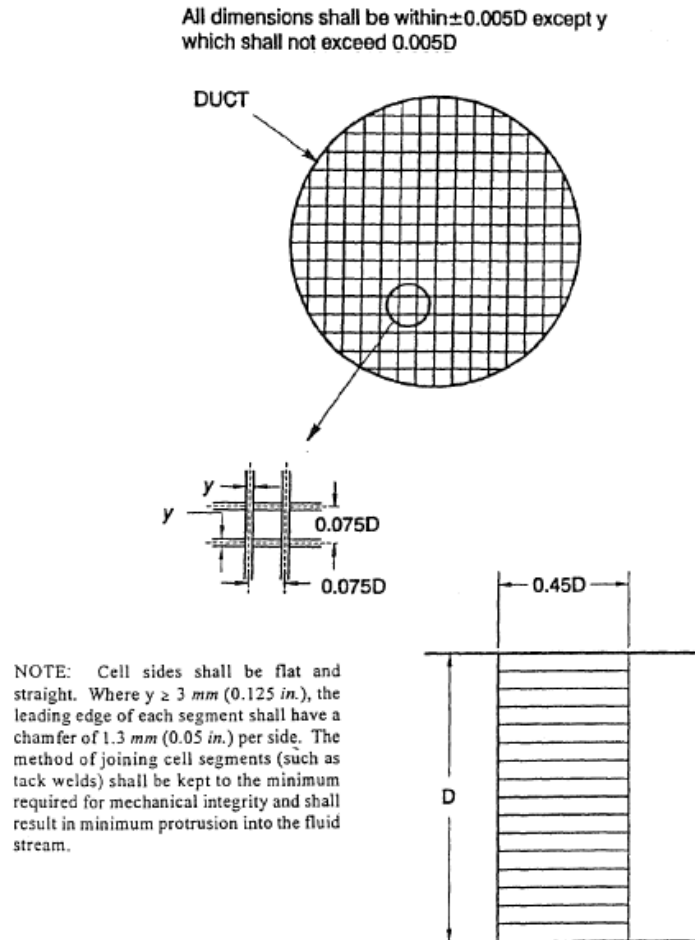


Figure B. 7 Flow Straighter Sizing [15]

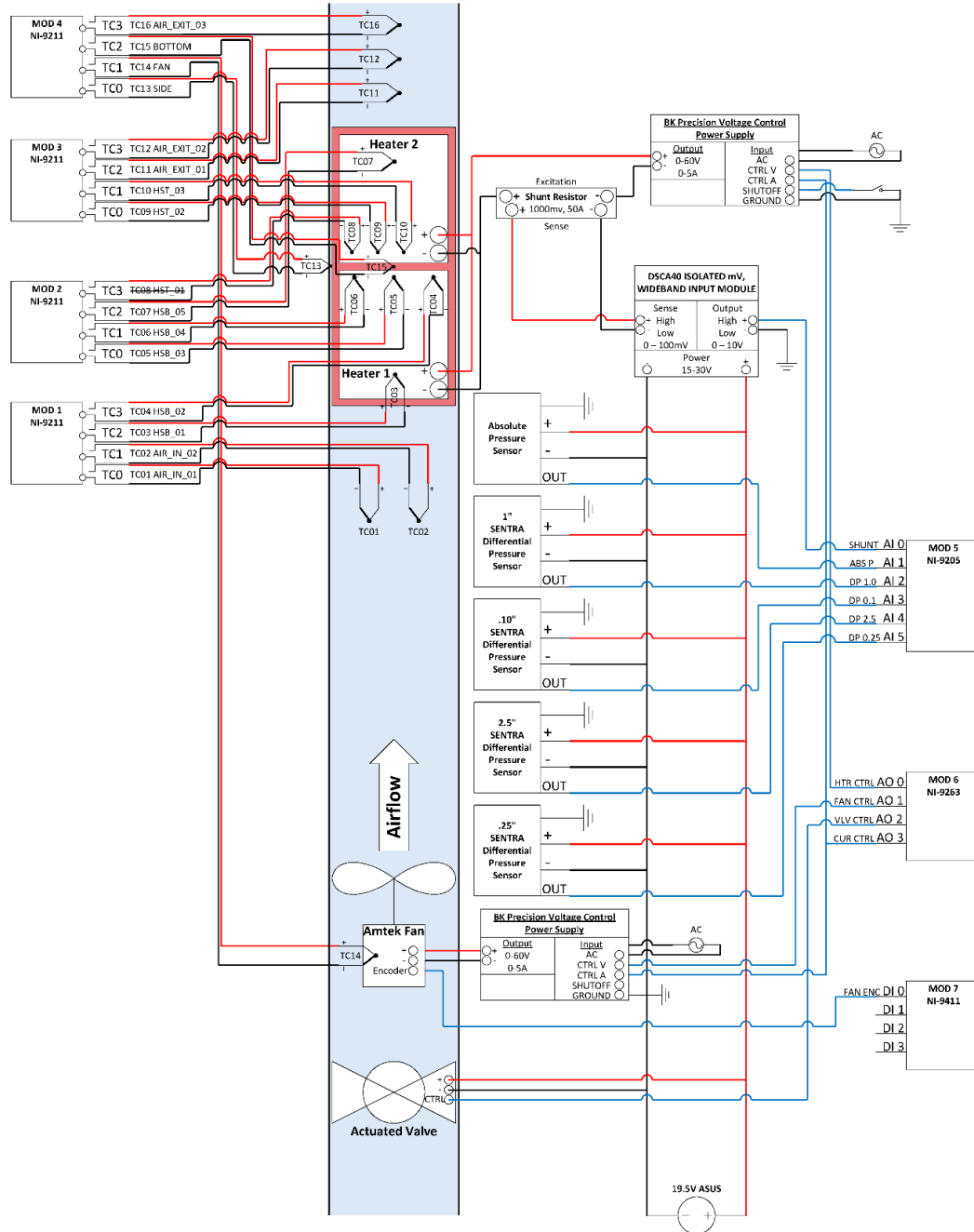
APPENDIX C PRESSURE DROP EXAMPLE

Pressure drop computation for the wind tunnel operating at 0.325 m³/s, 1.2 kg/m³

Section	0	1	2	3	4	5	6	7	8	9	10	11	12	13	14	15	16	17	18	19	20	21	22A	22B-0
Description	Ambient	Venturi Nozzle Inlet	Venturi Nozzle Exit	Valve	Straight Duct from 4	Diffuser 1	Elbow	Fan	Nozzle 1	Honeycomb b 1 Inlet	Honeycomb b 1 Exit	Straight Duct from 10-11	Expanding Duct from Corner 1	Straight Ducting 12-13	Expanding Corner 2	Honeycomb b 2 Inlet	Honeycomb b 2 Exit	Straight Duct from 16-17	Bypass Nozzle	Heat Sink Inlet	Heat Sink Exit	Straight Duct from 20-21	Exit Diffuser	Block Change Exit
Minor	--	Sudden Contraction	Controlled Contraction	--	--	Controlled Enlargement	Constant Radius Corner	--	Controlled Contraction	Sudden Contraction	Sudden Enlargement	--	Expanding Corner	--	Expanding Corner	Sudden Contraction	Sudden Enlargement	--	Controlled Contraction	Sudden Contraction	Sudden Enlargement	--	Controlled Enlargement	Sudden Enlargement
Major (Computed From)	--	--	1-2	2-3	3-4	4-5	5-6	--	7-8	8-9	9-10	10-11	--	12-13	--	14-15	15-16	16-17	17-18	18-19	18-19	20-21	21-22	--
Loss Type		Minor	Minor & Major	Major	Major	Minor & Major	Minor & Major	None	Minor & Major	Minor & Major	Minor & Major	Major	Minor	Major	Minor	Major	Minor & Major	Major	Major	Minor	Minor & Major	Major	Minor	Minor
Length (mm)		0.00	60.45	33.37	33.37	76.20	107.21		101.60	134.62	25.40	108.97		132.08		40.64	25.40	317.50	38.10	25.40	101.60	19.05	31.75	0.00
Height (mm)									50.80	50.80	50.80	50.80	50.80	50.80	50.80	50.80	50.80	50.80	50.80	50.80	50.80	50.80	50.80	
Width (mm)									50.80	50.80	50.80	50.80	50.80	50.80	50.80	50.80	50.80	50.80	50.80	50.80	50.80	50.80	50.80	
Radius (mm)		37.47	19.05	19.05	19.05	38.10	38.10	36.58																
Diameter (mm)		74.93	38.10	38.10	38.10	76.20	76.20	73.15																
Friction Factor									6.28										6.93				8.24	
Angle α/2 (Deg)			16.94			14.04													0.00			0.00		
Angle α/2 (Deg)			16.94			14.04						0.0719												
CSA (m²)	1	0.0044	0.0011	0.0011	0.0011	0.0046	0.0046	0.0042	0.0026	0.0021	0.0026	0.0026	0.0026	0.0026	0.0026	0.0021	0.0026	0.0026	0.0016	0.0009	0.0016	0.0016	0.0026	1
CSA Change Ratio N	226.7768	3.8678	1.0000	1.0000	1.0000	0.2500	1.0000	1.0851	1.6286	1.2346	0.8100	1.0000	1.0000	1.0000	1.0000	1.2346	0.8100	1.0000	1.5873	1.7566	0.9593	1.0000	0.6300	0.0026
Ratio C-rad/HyDia							0.855667																	
Corner Radius (m)							0.0825					0.0102												
Corner Diagonal (m)												0.0719												
Corner Chord Length (m)												0.0234												
Recommended C-rad (m)												0.0127												
Recommended α of Vents											4.31	4.31												
f/W _{max}											0.20	0.20									0.0011			
Coefficient, f _μ											0.2	0.2									0.0012			
Gap Between Fins, B (mm)																				6.34				
Heat Sink Width, W (mm)																				46.05				
Number of Fins, N																				6.00				
Fan Thickness, t (mm)																				2.39				
Height of fins, H (mm)																				24.13				
CSA Change Ratio N ^{1/2} , σ																				0.8889				
Characteristic Length, L*																				0.0000				
Friction Factor, f																				0.0001				
Apparent Friction Factor, f _{app}																				0.0022				
Recommended HC Length (m)										0.3048						0.3048								
Wetted Perimeter P (m)	1	0.235	0.120	0.120	0.120	0.239	0.239	0.230	0.203	0.009	0.203	0.203	0.203	0.203	0.203	0.203	0.3638	0.203	0.166	0.061	0.166	0.166	0.203	1
Hydraulic Diameter D _h (m)	4	0.07493	0.0381	0.0381	0.0381	0.0762	0.0762	0.0732	0.0508	0.0023	0.0508	0.0508	0.0508	0.0508	0.0508	0.0023	0.0508	0.0508	0.0393	0.0100	0.0393	0.0393	0.0508	4.0000
Dynamic viscosity (μ)	1.81E-05																							
Density (kg/m³)	1.2																							
VPR (m/s)	0.325	0.325	0.325	0.325	0.325	0.325	0.325	0.325	0.325	0.325	0.325	0.325	0.325	0.325	0.325	0.325	0.325	0.325	0.325	0.325	0.325	0.325	0.325	0.325
Velocity (m/s)	0.33	73.70	285.06	285.06	285.06	71.27	71.27	77.33	125.94	155.48	125.94	125.94	125.94	125.94	125.94	155.48	125.94	125.94	351.14	199.90	199.90	125.94	0.33	
Friction Coefficient A	0.3507	0.0143	0.0026	0.0026	0.0026	0.0143	0.0143	0.0142	0.0139	0.0258	0.0139	0.0139	0.0139	0.0139	0.0139	0.0258	0.0139	0.0139	0.0134	0.0155	0.0134	0.0134	0.0139	0.0139
Reynolds Number	86990	357518	719246	719246	719246	359623	359623	374607	42671	23537	42671	42671	42671	42671	42671	23537	42671	42671	51941	23349	51941	51941	42671	86990
Minor Loss Coefficient, f _{minor}	3.10	0.500	0.005	0.005	0.005	0.407	0.390		0.010	0.44	0.18	0.226	0.226	0.226	0.226	0.44	0.18	0.18	0.04	0.04	0.04	0.04	0.059	1.000
Minor Loss _{Minor loss} (Pa)	63129.7	1620.04	246.263	246.263	246.263	1241513	1066563		94056	2094954	1715369	2151362	2151362	2151362	2151362	2094954	1715369	1715369	100167	1632524	2402206	565898	951121	951121
Major Loss _{Major loss} (Pa)	19712.0	635721	635721	635721	635721	341864	61336		142625	340971	4153283	383278	343367	343367	343367	106462	4153283	4153283	825403	207339	6703388	155304	152464	152464
Pressure Losses _{Pressure Losses} (Pa)	82841.7	1625.04	528.821	528.821	528.821	1583377	1127899	0.000	236680	2444925	5868552	383278	2352562	343367	343367	1157562	2006066	5868552	825403	283774	16325273	27126613	155304	718862
Percent of total %		2.0%	0.6%	0.8%	0.8%	1.9%	1.4%		0.3%	3.0%	71%	0.3%	2.6%	0.4%	2.6%	2.7%	71%	1.0%	0.3%	20.0%	32.7%	0.2%	0.9%	11.5%

APPENDIX D WIRING DIAGRAM

Experimental Wiring Diagram for Control, Power, and Data Acquisition



APPENDIX E PRESSURE SENSOR CALIBRATION INFO

Sensor Information

Sensor Part Number: 5221015PA2F2BE1S

Serial Number: F033141

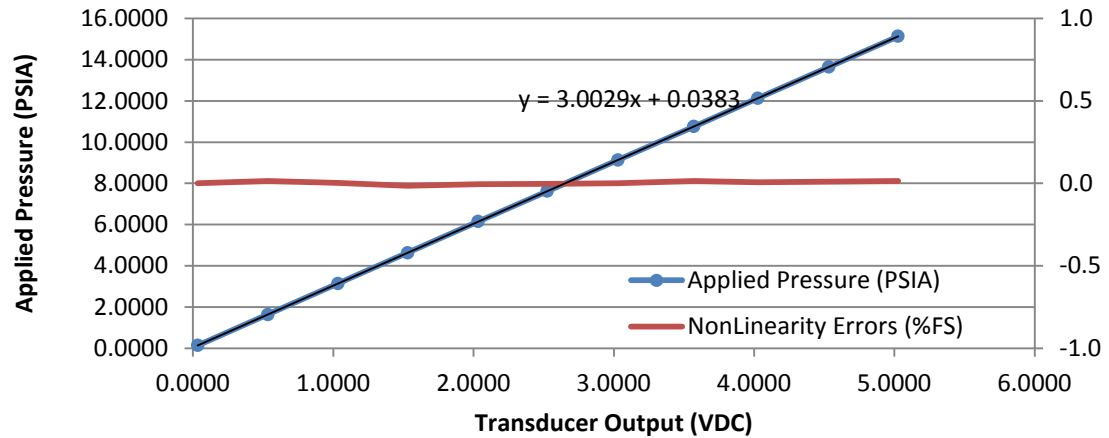
Sensor Range: 0 to 15 PSIA

Output: 0.05-5.0 VDC

Supply Voltage: 24 VDC

Cal Date: 6/16/2015

Calibration Curve For Absolute Sensor 15PSIA



Regression Statistics

Multiple R	0.999999965
R Square	0.999999931
Adjusted R Square	0.999999923
Standard Error	0.001381822
Observations	11
Intercept	0.038272181
X Variable 1	3.00288222

Sensor Information

Sensor Part Number: 26412R5WD2DT1F

Serial Number: 8039682

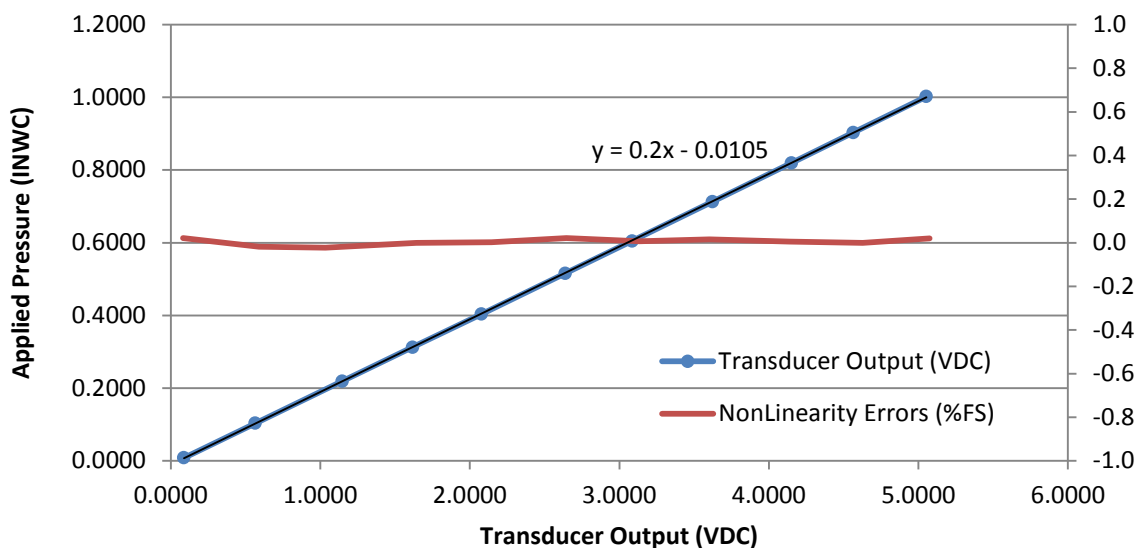
Sensor Range: 0 to 2.5 INWC

Output: 0.05-5.05 VDC

Supply Voltage: 24 VDC

Cal Date: 3/12/2015

Calibration Curve For Sensor Range 0-2.5 INWC



Regression Statistics

Multiple R	0.999999902
R Square	0.999999804
Adjusted R Square	0.999999782
Standard Error	0.000389375
Observations	11
Intercept	-0.02455293
X Variable 1	0.500055114

Sensor Information

Sensor Part Number: 2641001WD2DT1F

Serial Number: 8039683

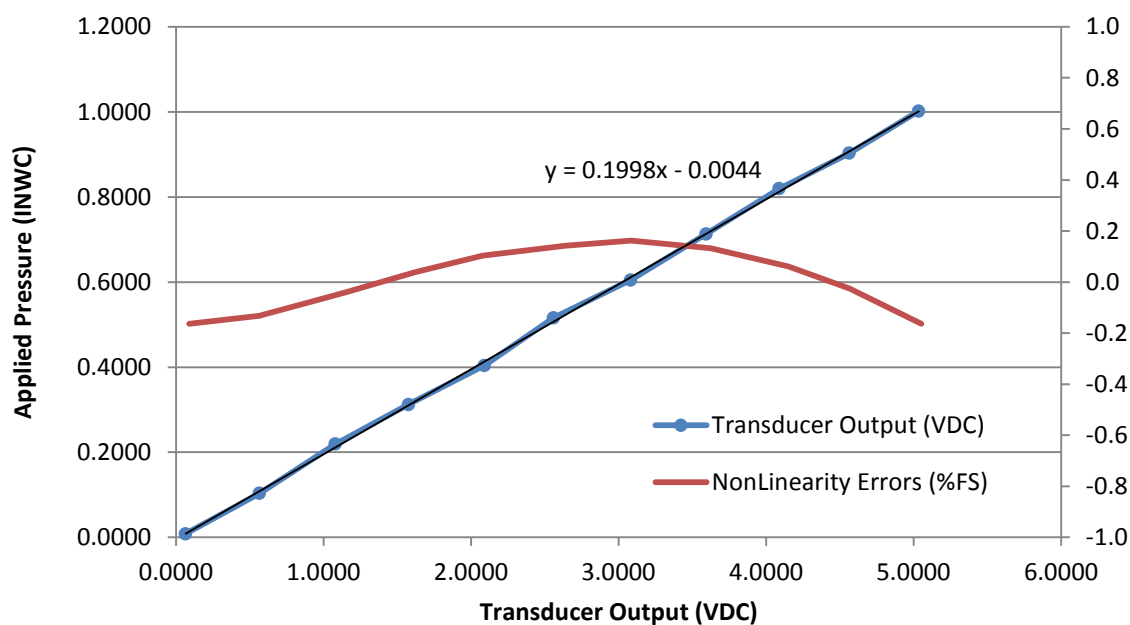
Sensor Range: 0 to 1.0 INWC

Output: 0.05-5.05 VDC

Supply Voltage: 24 VDC

Cal Date: 3/12/2015

Calibration Curve For Sensor Range 0-1.0 INWC



Regression Statistics

Multiple R	0.999993514
R Square	0.999987028
Adjusted R Square	0.999985586
Standard Error	0.001255886
Observations	11
Intercept	-0.01045236
X Variable 1	0.199952322

Sensor Information

Sensor Part Number: 2641R25WD2DT1F

Serial Number: 8039684

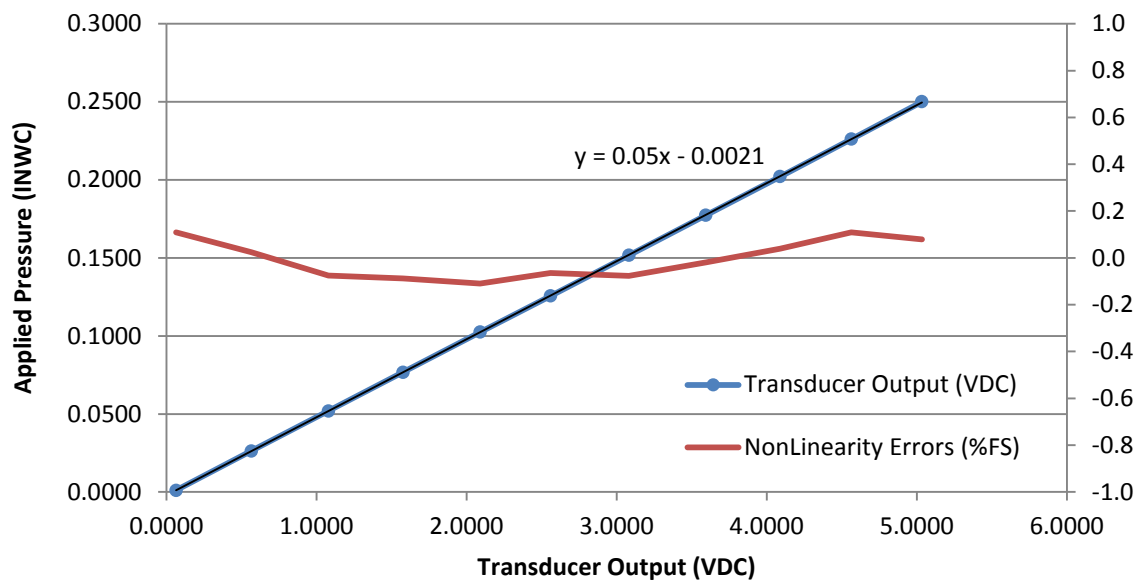
Sensor Range: 0 to 0.25 INWC

Output: 0.05-5.05 VDC

Supply Voltage: 24 VDC

Cal Date: 3/12/2015

Calibration Curve For Sensor Range 0-0.25 INWC



Regression Statistics

Multiple R	0.999996214
R Square	0.999992428
Adjusted R Square	0.999991586
Standard Error	0.000240106
Observations	11
Intercept	-0.00214206
X Variable 1	0.05001017

Sensor Information

Sensor Part Number: 26410R1WD2DT1F

Serial Number: 8039685

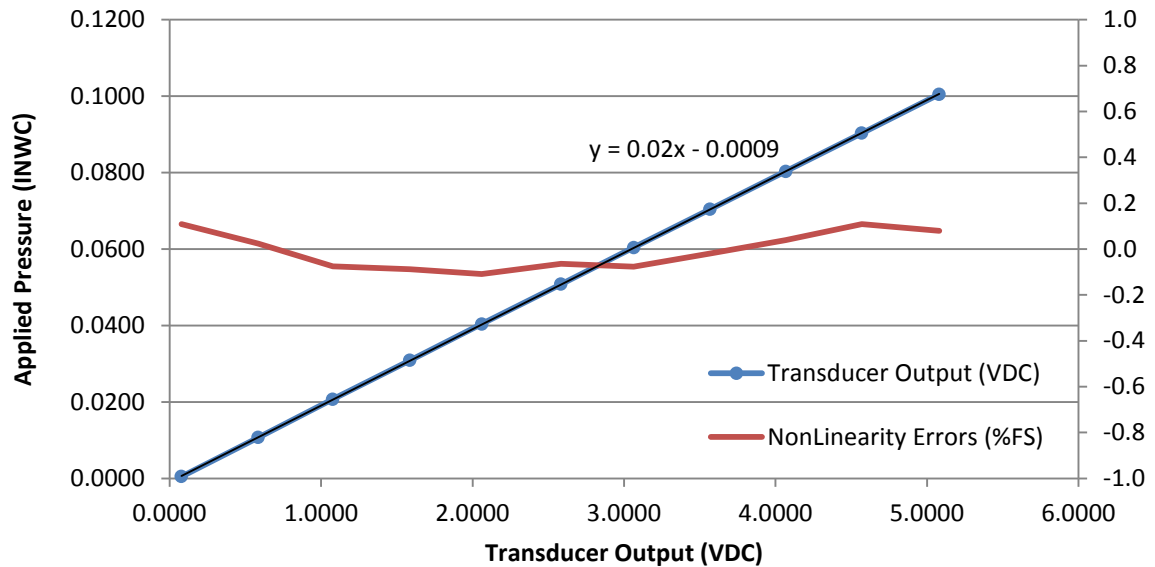
Sensor Range: 0 to 0.10 INWC

Output: 0.05-5.05 VDC

Supply Voltage: 24 VDC

Cal Date: 3/12/2015

Calibration Curve For Sensor Range 0-0.10 INWC



Regression Statistics

Multiple R	0.999995399
R Square	0.999990797
Adjusted R Square	0.999989775
Standard Error	0.000105692
Observations	11

Coefficients

Intercept	-0.00087114
X Variable 1	0.019971059

APPENDIX F

THERMOCOUPLE CALIBRATION PROCEDURE

A total of 16 thermocouples were utilized for this experiment. Their calibrations were conducted prior to their installation within the experimental setup. The process for their calibration was to use a calibrated reference temperature RTD [Hart Scientific 1502A with Hart Scientific 5628 probe (Standard Error, $\pm 0.033^{\circ}\text{C}$)] and a silicone oil bath (Hart Scientific 7320) to control the temperature. The range of temperatures chosen for calibration was 0 - 150°C . To carry out the process of calibration a LabVIEW VI was created to control the bath temperature and record thermocouple measurements via the NI cRIO 9112. Four NI 9211 thermocouple modules, each having four inputs, were used with the cRIO.

The process for calibrating the thermocouples was to secure all of the probe tips close to the RTD tip and submerge them in the fluid. This was to ensure that the temperature at each thermocouple tip was as close to the RTD reference temperature as possible. The probe bundle was then positioned securely in place within the oil and insulation was placed over the opening. Figure F. 1 shows the calibration in progress.

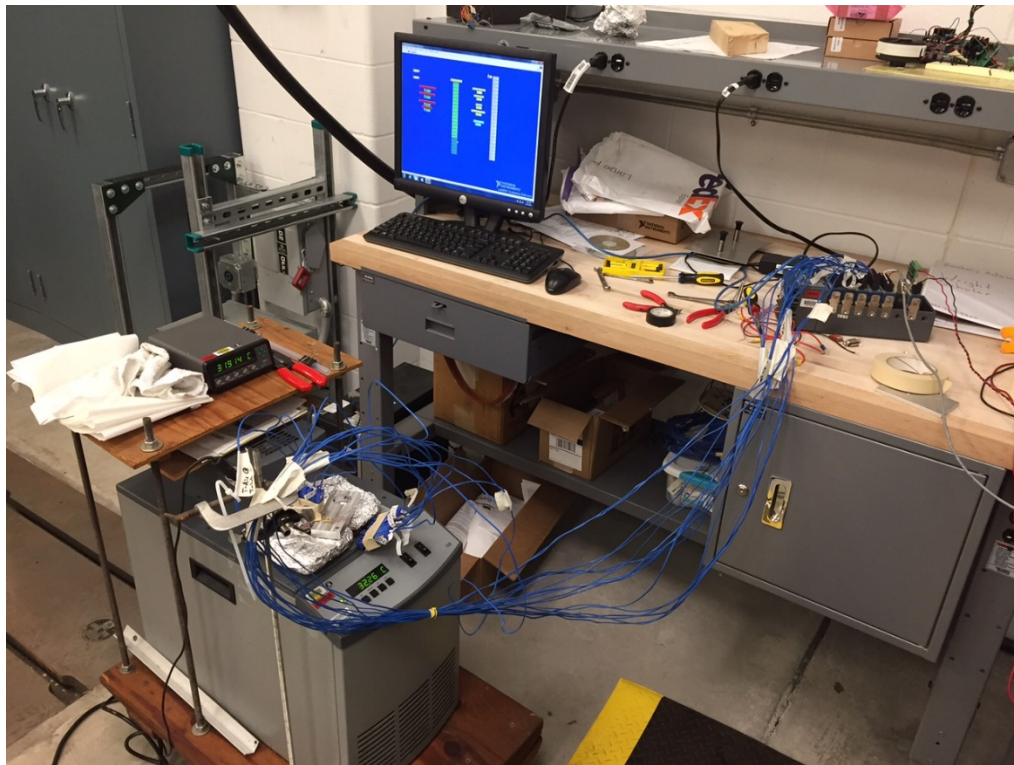


Figure F. 1 Thermocouple Test Setup

Once the setup was completed the LabVIEW program initiated the calibration by commanding the bath to reach and hold a steady temperature. With a range of 0 – 150°C ,

measurements were taken at every 10 °C increment starting at 0 °C climbing to 150 °C then back down to 0 °C. A total of 10 readings were taken at one sample per second, for each temperature increment and averaged. The reading for each temperature point was taken when the standard deviation of the RTD fell under 0.0005 °C. Once recording is finished the VI commands the bath to the next set point and the process repeats. A total of 29 averaged temperature measurements were taken.

It is worth noting that at the time of calibration the bath refrigeration system was not working properly. For temperature points below ambient temperature an ice bath was prepared and used instead of the oil bath. Also worth noting, after the initial calibration four thermocouples were damaged during installation and required a second calibration after they were repaired. The results of the calibration are as follows,

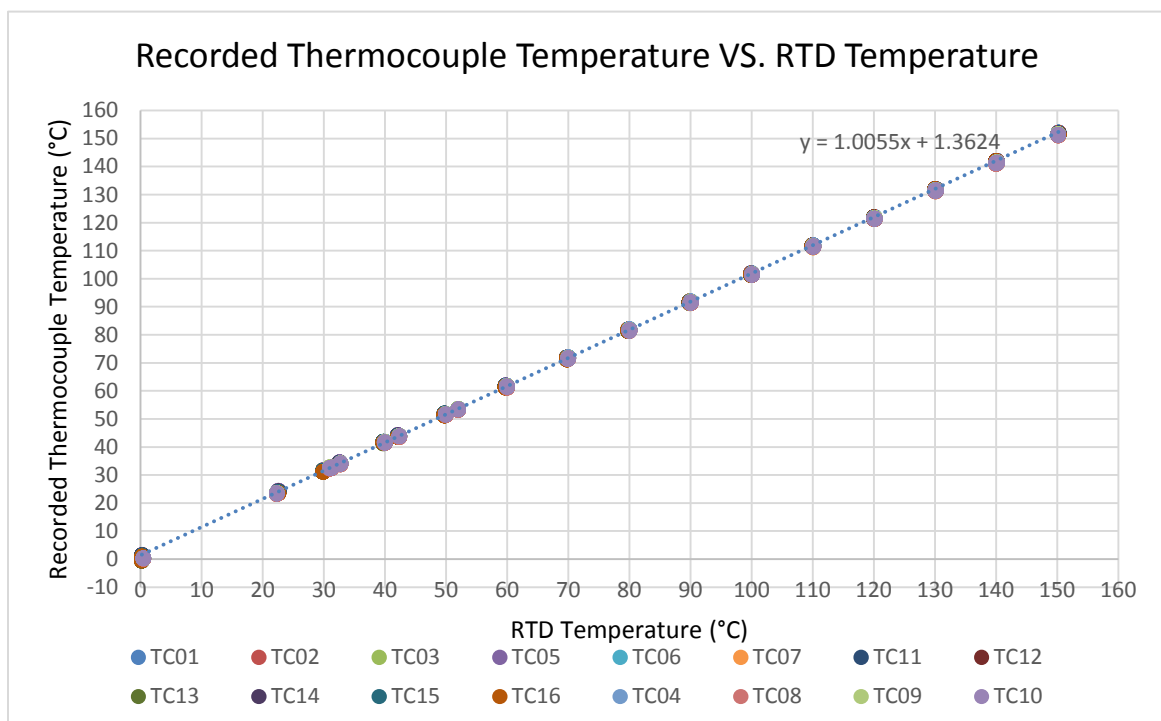


Figure F. 2 Thermocouple Calibration Results

Figure F. 2 shows all of the thermocouple measurements taken for the calibration. It is apparent that the lack of active cooling caused a group of measurements to be taken slightly above room temperature. However, this does not adversely affect the calibration.

Once all the data was recorded the next step was to create a regression equation for each thermocouple. For this a linear best fit regression equation was chosen. Table F - 1 shows the results from the linear regression analysis for the thermocouple temperature vs. the RTD temperature.

Table F - 1 Thermocouple Regression Analysis

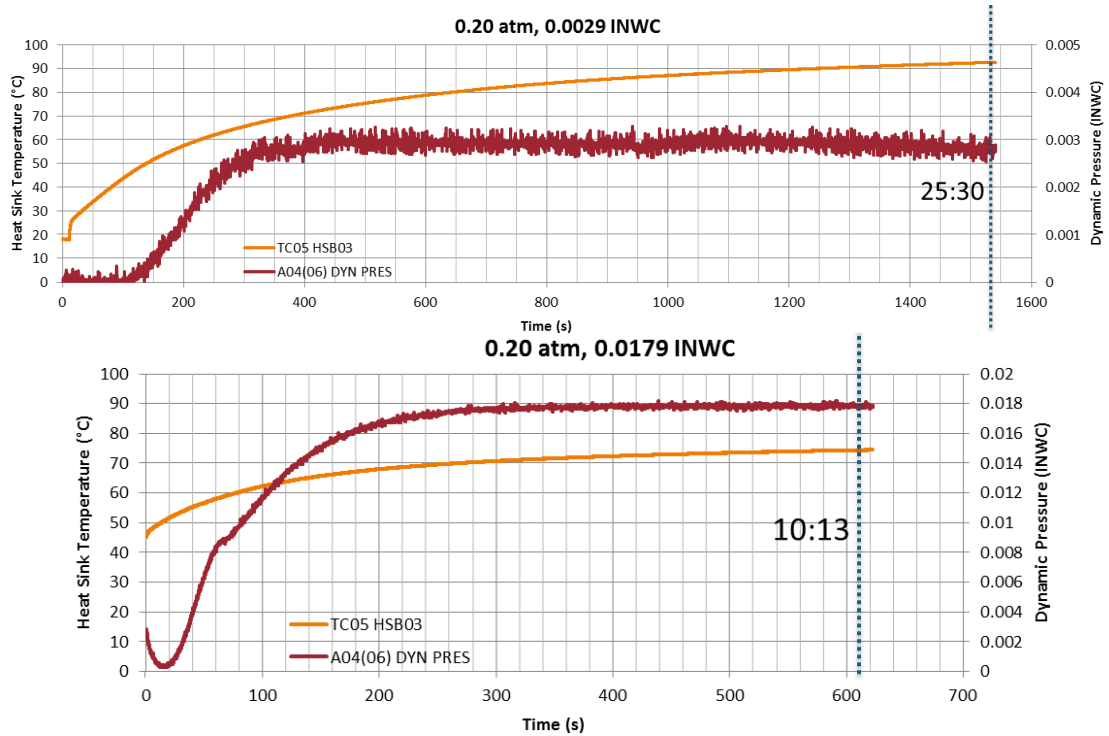
THERMO- COUPLE	SLOPE (°C/°C)	OFFSET (°C)	STANDARD ERROR (±°C)
TC01	0.9945	-1.35	0.4165
TC02	0.9947	-1.32	0.4205
TC03	0.9990	-1.55	0.4083
TC04	0.9972	-1.34	0.3807
TC05	0.9986	-1.55	0.4465
TC06	0.9987	-1.35	0.3982
TC07	0.9987	-1.16	0.3849
TC08	0.9984	-1.00	0.3790
TC09	0.9986	-1.33	0.4239
TC10	0.9988	-1.21	0.4047
TC11	0.9945	-1.13	0.4175
TC12	0.9941	-1.04	0.4172
TC13	0.9954	-0.97	0.3947
TC14	0.9980	-1.41	0.4391
TC15	0.9978	-1.37	0.4705
TC16	0.9945	-0.97	0.4465

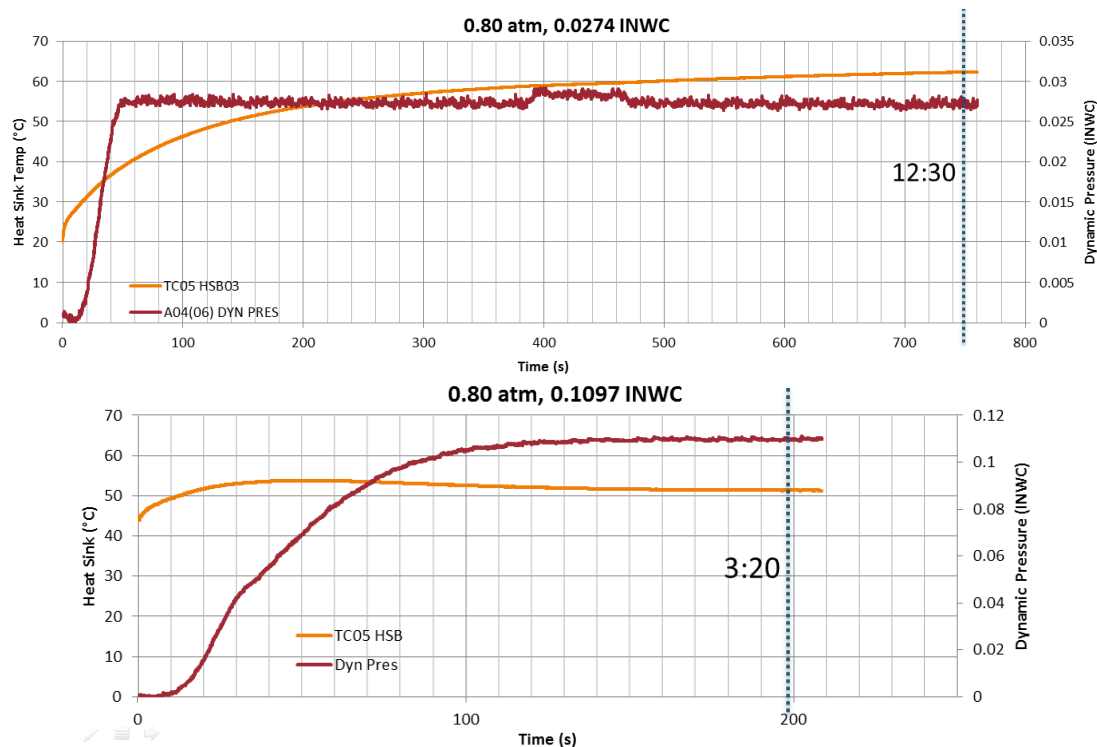
The slope and offset were programed into the experimental LabVIEW VI to make the temperature correction. The Standard Error was later used in the uncertainty analysis.

APPENDIX G

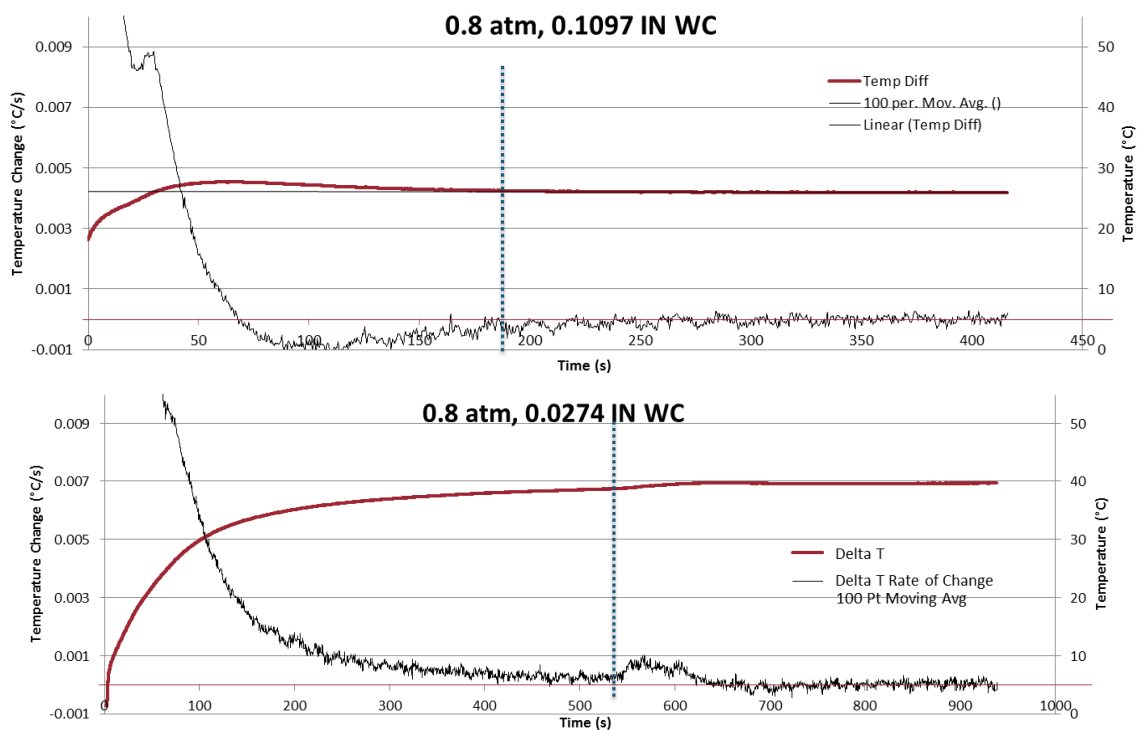
HEAT SINK TEMPERATURE SETTLING TIME

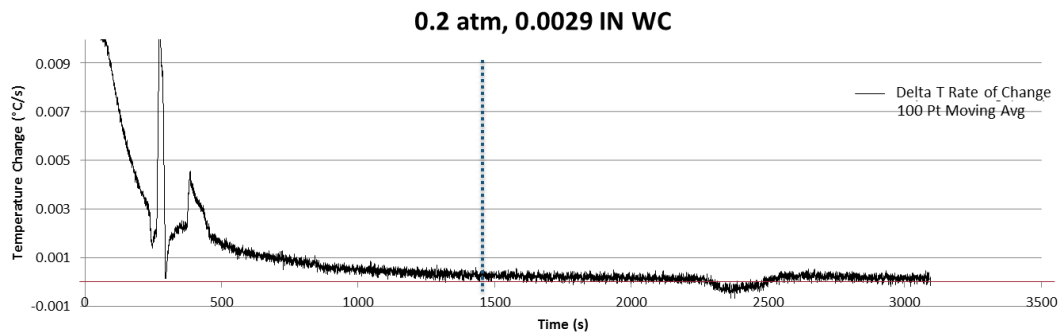
The following figures were produced to investigate the settling time for steady state conditions of the air velocity and heat sink temperature, under varying conditions. The dotted blue line denotes when data recording was triggered.





The following tests were run at extended time to validate the ability of the program to determine steady state. The dotted blue line denotes the time at which normal triggering, to log data, would have occurred.





APPENDIX H

RESULTS UNCERTAINTY ANALYSIS

The uncertainty of the results of this thesis was determined by the method of error propagation through partial derivatives. The standard error of a relationship, $f(x, y, z)$, is represented by the sum of the squares of the product of its partial derivatives $\frac{\partial f(x, y, z)}{\partial x}$, $\frac{\partial f(x, y, z)}{\partial y}$ & $\frac{\partial f(x, y, z)}{\partial z}$ and their individual measurement uncertainties.

$$\sigma_{f(x, y, z)}^2 = \left(\sigma_x \frac{\partial f(x, y, z)}{\partial x} \right)^2 + \left(\sigma_y \frac{\partial f(x, y, z)}{\partial y} \right)^2 + \left(\sigma_z \frac{\partial f(x, y, z)}{\partial z} \right)^2$$

In the above equation, σ_x , σ_y & σ_z are the individual uncertainties for the respective variables x , y , & z . They are determined from measurement uncertainty or propagation of uncertainty through partial derivation.

The measurement uncertainty was determined by the addition of the calibration uncertainty and the standard error of the regression. The calibration uncertainty was taken as the uncertainty of the device used for calibration. The standard error is the product of the curve fitting the calibration results to the best fit equation.

The regression standard error is found by the method of Least Squares.

$$\sigma = \sqrt{\frac{\sum_{i=1}^n \varepsilon_i^2}{N}}$$

where ε_i is the error for each individual measurement and N was the total number of measurements. The results for all the sensors used in this experiment are shown in the table below.

Table H - 1 Measurement Uncertainty

MEASUREMENT	UNITS	CALIBRATED RANGE	UNCERTAINTY NOMENCLATURE	STANDARD ERROR (\pm)	CALIBRATION UNCERTAINTY (\pm)	MEASUREMENT UNCERTAINTY (\pm)
SHUNT CURRENT	Amps	0-5	σ_{I_Shunt}	0.000023	0.0031	0.0031
HEATER RESISTANCE	Ohms	N/A	σ_{R_Heater}	0.000023	N/A	0.000023
DYNAMIC PRESSURE	InH2O	0-0.10	$\sigma_{P_Dyc:0.10}$	0.00004	0.00011	0.00015
DYNAMIC PRESSURE	InH2O	0-0.25	$\sigma_{P_Dyc:0.25}$	0.00010	0.00024	0.00034
STATIC PRESSURE DROP	InH2O	0-1.0	$\sigma_{P_Stc:1.0}$	0.00040	0.00126	0.00166
STATIC PRESSURE DROP	InH2O	0-2.5	$\sigma_{P_Stc:2.5}$	0.00100	0.00039	0.00139
ABSOLUTE PRESSURE	PSI	0-15	$\sigma_{P_ABS:15}$	0.00600	0.00138	0.00738
AIR AT INLET 1	°C	0-150	σ_{TC01}	0.033	0.4165	0.4495
AIR AT INLET 2	°C	0-150	σ_{TC02}	0.033	0.4205	0.4535
HEAT SINK BASE 1	°C	0-150	σ_{TC03}	0.033	0.4083	0.4413
HEAT SINK BASE 2	°C	0-150	σ_{TC04}	0.033	0.3807	0.4137
HEAT SINK BASE 3	°C	0-150	σ_{TC05}	0.033	0.4465	0.4795
HEAT SINK BASE 4	°C	0-150	σ_{TC06}	0.033	0.3982	0.4312
HEAT SINK BASE 5	°C	0-150	σ_{TC07}	0.033	0.3849	0.4179
HEAT SINK TIP 1	°C	0-150	σ_{TC08}	0.033	0.3790	0.4120
HEAT SINK TIP 2	°C	0-150	σ_{TC09}	0.033	0.4239	0.4569
HEAT SINK TIP 3	°C	0-150	σ_{TC10}	0.033	0.4047	0.4377
AIR AT EXIT 1	°C	0-150	σ_{TC11}	0.033	0.4175	0.4505
AIR AT EXIT 2	°C	0-150	σ_{TC12}	0.033	0.4172	0.4502
HOUSING EXTERNAL 1	°C	0-150	σ_{TC13}	0.033	0.3947	0.4277
FAN	°C	0-150	σ_{TC14}	0.033	0.4391	0.4721
HOUSING EXTERNAL 2	°C	0-150	σ_{TC15}	0.033	0.4705	0.5035
AIR AT EXIT 3	°C	0-150	σ_{TC16}	0.033	0.4465	0.4795

Other measurements, such as physical dimensions were also used in the derivation of the experimental uncertainty. Since calibration was not necessary for physical dimensions a standard error was used based on the general tolerance for each specific part (± 0.02 in. for manufactured parts and ± 0.035 in. for 3D printed parts)

- Heat Transfer Coefficient**

Within this thesis the HTC was used to measure the performance of the heat sink. The uncertainty of this measure is a combination of many various measurements of

temperature, power, and pressure. The following is an accounting of the total uncertainty for the HTC. To begin the equation for the measured HTC of the base of the heat sink is as follows,

$$h_{base} = \frac{1}{R_{t,HS} A_{base}}$$

The heat transfer coefficient in its non-dimensional form is the Nusselt Number, Nu_{avg} .

$$Nu_{avg} = h_{base} \frac{L^*}{k_{fluid}}$$

Where L^* is the characteristic length that is computed by,

$$L^* = \sqrt{A_{base}}$$

Using substitution,

$$Nu_{avg} = \frac{1}{R_{t,HS} A_{base}} \frac{\sqrt{A_{base}}}{k_{fluid}} = \frac{1}{R_{t,HS} k_{fluid} A_{base}^{\frac{1}{2}}}$$

The thermal resistance, $R_{t,HS}$, is found with the following equation.

$$R_{t,HS} = \frac{\Delta T_{base}}{Q_{Conv}}$$

So, using substitution again, the equation for the Nusselt number becomes.

$$Nu_{avg} = \frac{Q_{Conv}}{\Delta T_{base} k_{fluid} A_{base}^{\frac{1}{2}}}$$

Form here the three uncertainties contributing to this measurement are: P_{heater} , ΔT_{base} & k_{fluid} . The following derivation was used to determine the total uncertainty propagation for the Nusselt number measurement.

$$\frac{\partial Nu_{avg}}{\partial Q_{Conv}} = \Delta T_{base}^{-1} k_{fluid}^{-1} A_{base}^{-\frac{1}{2}}$$

$$\frac{\partial Nu_{avg}}{\partial \Delta T_{base}} = -Q_{Conv} \Delta T_{base}^{-2} k_{fluid}^{-1} A_{base}^{-\frac{1}{2}}$$

$$\frac{\partial Nu_{avg}}{\partial k_{fluid}} = -Q_{Conv} \Delta T_{base}^{-1} k_{fluid}^{-2} A_{base}^{-\frac{1}{2}}$$

$$\frac{\partial Nu_{avg}}{\partial A_{base}} = -\frac{1}{2} Q_{Conv} \Delta T_{base}^{-1} k_{fluid}^{-1} A_{base}^{-\frac{3}{2}}$$

$$\begin{aligned}
\sigma_{Nu_{avg}}^2 = & \left(\sigma_{Q_{Conv}} \frac{\partial Nu_{avg}}{\partial P_{heater}} \right)^2 + \left(\sigma_{\Delta T_{base}} \frac{\partial Nu_{avg}}{\partial \Delta T_{base}} \right)^2 + \left(\sigma_{k_{fluid}} \frac{\partial Nu_{avg}}{\partial k_{fluid}} \right)^2 + \left(\sigma_{A_{base}} \frac{\partial Nu_{avg}}{\partial A_{base}} \right)^2 \\
\sigma_{Nu_{avg}}^2 = & \left(\sigma_{Q_{Conv}} \left(\Delta T_{base}^{-1} k_{fluid}^{-1} A_{base}^{-\frac{1}{2}} \right) \right)^2 \\
& + \left(\sigma_{\Delta T_{base}} \left(-Q_{Conv} \Delta T_{base}^{-2} k_{fluid}^{-1} A_{base}^{-\frac{1}{2}} \right) \right)^2 \\
& + \left(\sigma_{k_{fluid}} \left(-Q_{Conv} \Delta T_{base}^{-1} k_{fluid}^{-2} A_{base}^{-\frac{1}{2}} \right) \right)^2 \\
& + \left(\sigma_{A_{base}} \left(-\frac{1}{2} Q_{Conv} \Delta T_{base}^{-1} k_{fluid}^{-1} A_{base}^{-\frac{3}{2}} \right) \right)^2
\end{aligned}$$

The uncertainties, $\sigma_{Q_{Conv}}$, $\sigma_{\Delta T_{base}}$, $\sigma_{k_{fluid}}$ & $\sigma_{A_{base}}$ needed to be individually determined. The temperature difference of the base to the air, ΔT_{base} , was found through the following.

$$\Delta T_{base} = (T_{base} - T_{air-in}) = \frac{(TC03+TC04+TC05+TC06+TC07)}{5} - \frac{(TC01+TC02)}{2}$$

The uncertainty of this measurement was determined from the following derivation.

$$\frac{\partial \Delta T_{base}}{\partial TC01} = -\frac{1}{2}; \quad \frac{\partial \Delta T_{base}}{\partial TC02} = -\frac{1}{2}$$

$$\frac{\partial \Delta T_{base}}{\partial TC03} = \frac{1}{5}; \quad \frac{\partial \Delta T_{base}}{\partial TC04} = \frac{1}{5}$$

$$\frac{\partial \Delta T_{base}}{\partial TC05} = \frac{1}{5}; \quad \frac{\partial \Delta T_{base}}{\partial TC06} = \frac{1}{5}$$

$$\frac{\partial \Delta T_{base}}{\partial TC07} = \frac{1}{5}$$

$$\begin{aligned}
\sigma_{\Delta T_{base}}^2 = & \left(\sigma_{TC01} \frac{\partial \Delta T_{base}}{\partial TC01} \right)^2 + \left(\sigma_{TC02} \frac{\partial \Delta T_{base}}{\partial TC02} \right)^2 + \left(\sigma_{TC03} \frac{\partial \Delta T_{base}}{\partial TC03} \right)^2 \\
& + \left(\sigma_{TC04} \frac{\partial \Delta T_{base}}{\partial TC04} \right)^2 + \left(\sigma_{TC05} \frac{\partial \Delta T_{base}}{\partial TC05} \right)^2 + \left(\sigma_{TC06} \frac{\partial \Delta T_{base}}{\partial TC06} \right)^2 \\
& + \left(\sigma_{TC07} \frac{\partial \Delta T_{base}}{\partial TC07} \right)^2
\end{aligned}$$

$$\begin{aligned}
\sigma_{\Delta T_{base}}^2 = & \left(\sigma_{TC01} \left(-\frac{1}{2} \right) \right)^2 + \left(\sigma_{TC02} \left(-\frac{1}{2} \right) \right)^2 + \left(\sigma_{TC03} \left(\frac{1}{5} \right) \right)^2 + \left(\sigma_{TC04} \left(\frac{1}{5} \right) \right)^2 \\
& + \left(\sigma_{TC05} \left(\frac{1}{5} \right) \right)^2 + \left(\sigma_{TC06} \left(\frac{1}{5} \right) \right)^2 + \left(\sigma_{TC07} \left(\frac{1}{5} \right) \right)^2
\end{aligned}$$

For the uncertainty of the power being dissipated through convection by the heat sink, Q_{Conv} , the following equation was used.

$$Q_{Conv} = (I_{Shunt}^2 R_{e,Heater}) - P_{losses}$$

The uncertainty of this measurement was determined from the following derivation.

$$\frac{\partial Q_{Conv}}{\partial I_{Shunt}} = 2I_{Shunt} \times R_{e,Heater}$$

$$\frac{\partial Q_{Conv}}{\partial R_{e,Heater}} = I_{Shunt}^2$$

$$\frac{\partial Q_{Conv}}{\partial Q_{losses}} = -1$$

$$\sigma_{Q_{Conv}}^2 = \left(\sigma_{I_{Shunt}} \frac{\partial Q_{Conv}}{\partial I_{Shunt}} \right)^2 + \left(\sigma_{R_{e,Heater}} \frac{\partial Q_{Conv}}{\partial R_{e,Heater}} \right)^2 + \left(\sigma_{Q_{losses}} \frac{\partial Q_{Conv}}{\partial Q_{losses}} \right)^2$$

$$\sigma_{Q_{Conv}}^2 = \left(\sigma_{I_{Shunt}} (2I_{Shunt} \times R_{e,Heater}) \right)^2 + \left(\sigma_{R_{e,Heater}} (I_{Shunt}^2) \right)^2 + \left(\sigma_{Q_{losses}} (-1) \right)^2$$

Of these the uncertainties, $\sigma_{I_{Shunt}}$ & $\sigma_{R_{e,Heater}}$ are currently known from calibration. However, the uncertainty of the losses due to conduction, $Q_{c,losses}$, and radiation $Q_{r,losses}$ will need to be found.

Q_{losses} , is the sum of the two following variables.

$$Q_{losses} = Q_{c,losses} + Q_{r,losses}$$

Therefore, $\sigma_{Q_{losses}}$ becomes,

$$\sigma_{Q_{losses}}^2 = (\sigma_{Q_{c,losses}})^2 + (\sigma_{Q_{r,losses}})^2$$

The losses through conduction are found by the following equation.

$$Q_{c,losses} = 2 \frac{\Delta T_{Side_HS}}{R_{t,Housing_Side}} + \frac{\Delta T_{Bottom_HS}}{R_{t,Housing_Bottom}}$$

Breaking this down, the uncertainty of this measurement was determined from the following derivation.

$$\frac{\partial Q_{c,losses}}{\partial \Delta T_{Side_HS}} = \frac{2}{R_{t,Housing_Side}}; \quad \frac{\partial Q_{c,losses}}{\partial R_{t,Housing_Side}} = -2\Delta T_{Side_HS} R_{t,Housing_Side}^{-2}$$

$$\frac{\partial Q_{c,losses}}{\partial \Delta T_{Bottom_HS}} = \frac{1}{R_{t,Housing_Bottom}}$$

$$\frac{\partial Q_{c,losses}}{\partial R_{t,Housing_Bottom}} = -\Delta T_{Bottom_HS} R_{t,Housing_Bottom}^{-2}$$

$$\begin{aligned} \sigma_{Q_{c,losses}}^2 &= \left(\sigma_{\Delta T_{Side_HS}} \frac{\partial Q_{c,losses}}{\partial \Delta T_{Side_HS}} \right)^2 + \left(\sigma_{R_{t,Housing_Side}} \frac{\partial Q_{c,losses}}{\partial R_{t,Housing_Side}} \right)^2 \\ &\quad + \left(\sigma_{\Delta T_{Bottom_HS}} \frac{\partial Q_{c,losses}}{\partial \Delta T_{Bottom_HS}} \right)^2 + \left(\sigma_{R_{t,Housing_Bottom}} \frac{\partial Q_{c,losses}}{\partial R_{t,Housing_Bottom}} \right)^2 \\ \sigma_{Q_{c,losses}}^2 &= \left(\sigma_{\Delta T_{Side_HS}} (2R_{t,Housing_Side}^{-1}) \right)^2 \\ &\quad + \left(\sigma_{R_{t,Housing_Side}} (-2\Delta T_{Side_HS} R_{t,Housing_Side}^{-2}) \right)^2 \\ &\quad + \left(\sigma_{\Delta T_{Bottom_HS}} (R_{t,Housing_Bottom}^{-1}) \right)^2 \\ &\quad + \left(\sigma_{R_{t,Housing_Bottom}} (-\Delta T_{Bottom_HS} R_{t,Housing_Bottom}^{-2}) \right)^2 \end{aligned}$$

Of these uncertainties, $\sigma_{R_{t,Housing_Side}}$, $\sigma_{\Delta T_{Side_HS}}$, $\sigma_{R_{t,Housing_Bottom}}$ & $\sigma_{\Delta T_{Bottom_HS}}$ all needed to be determined.

The calculation for $R_{t,Housing_Side}$ is as follows,

$$R_{t,Housing_Side} = \frac{L_{Side}}{K_{PC} A_{HS_Side}} + \frac{1}{h_{c,Side} A_{HS_Side}}$$

The uncertainty of this measurement was determined from the following derivation.

$$\begin{aligned} \frac{\partial R_{t,Housing_Side}}{\partial L_{Side}} &= K_{PC}^{-1} A_{HS_Side}^{-1} \\ \frac{\partial R_{t,Housing_Side}}{\partial K_{PC}} &= -L_{Side} K_{PC}^{-2} A_{HS_Side}^{-1} \\ \frac{\partial R_{t,Housing_Side}}{\partial A_{HS_Side}} &= -A_{HS_Side}^{-2} (L_{Side} K_{PC}^{-1} + h_{c,Side}^{-1}) \\ \frac{\partial R_{t,Housing_Side}}{\partial h_{c,Side}} &= -h_{c,Side}^{-2} A_{HS_Side}^{-1} \\ \sigma_{R_{t,Housing_Side}}^2 &= \left(\sigma_{L_{Side}} \frac{\partial R_{t,Housing_Side}}{\partial L_{Side}} \right)^2 + \left(\sigma_{K_{PC}} \frac{\partial R_{t,Housing_Side}}{\partial K_{PC}} \right)^2 \\ &\quad + \left(\sigma_{A_{HS_Side}} \frac{\partial R_{t,Housing_Side}}{\partial A_{HS_Side}} \right)^2 + \left(\sigma_{h_{c,Side}} \frac{\partial R_{t,Housing_Side}}{\partial h_{c,Side}} \right)^2 \end{aligned}$$

$$\begin{aligned}
\sigma_{R_{t,Housing_Side}}^2 &= \left(\sigma_{L_{Side}} (K_{PC}^{-1} A_{HS_Side}^{-1}) \right)^2 \\
&+ \left(\sigma_{K_{PC}} (-L_{Side} K_{PC}^{-2} A_{HS_Side}^{-1}) \right)^2 \\
&+ \left(\sigma_{A_{HS_Side}} - A_{HS_Side}^{-2} (L_{Side} K_{PC}^{-1} + h_{c,Side}^{-1}) \right)^2 \\
&+ \left(\sigma_{h_{c,Side}} (-h_{c,Side}^{-2} A_{HS_Side}^{-1}) \right)^2
\end{aligned}$$

The uncertainty for the area of the heat sink side, A_{HS_Side} , needed to be found. Using a standard manufacturing tolerance of ± 0.02 in. (± 0.00005 m), the uncertainty $\sigma_{A_{HS_Side}}$ was found through the following derivation.

$$\sigma_{A_{HS_Side}}^2 = \left(\sigma_{H_{HS}} \frac{\partial A_{HS_Side}}{\partial H_{HS}} \right)^2 + \left(\sigma_{W_{HS}} \frac{\partial A_{HS_Side}}{\partial W_{HS}} \right)^2$$

$$\sigma_{H_{HS}} = \sigma_{W_{HS}} = 0.000508m$$

$$\sigma_{A_{HS_Side}}^2 = (0.00005(W_{HS}))^2 + (0.00005(H_{HS}))^2 = 2.92 \times 10^{-9}m^2$$

This is also the same method used to find the uncertainty of the A_{base} (A_{HS_Bottom})

$$\sigma_{A_{base}}^2 = (0.00005(W_{HS}))^2 + (0.00005(B_{HS}))^2 = 3.21 \times 10^{-9}m^2$$

The calculation for ΔT_{Side_HS} was made using the following equation.

$$\Delta T_{Side_HS} = \Delta(T_{avg, HS_side} - TC13) = \frac{1}{2} \left(\left(\frac{\Delta TC04 + \Delta TC06}{2} \right) + \left(\frac{\Delta TC09 + \Delta TC10}{2} \right) \right) - \Delta TC13$$

The uncertainty of this measurement was determined from the following derivation.

$$\begin{aligned}
\frac{\partial \Delta T_{Side_HS}}{\partial TC04} &= \frac{1}{4}; & \frac{\partial \Delta T_{Side_HS}}{\partial TC06} &= \frac{1}{4} \\
\frac{\partial \Delta T_{Side_HS}}{\partial TC09} &= \frac{1}{4}; & \frac{\partial \Delta T_{Side_HS}}{\partial TC10} &= \frac{1}{4} \\
\frac{\partial \Delta T_{Side_HS}}{\partial TC13} &= -1
\end{aligned}$$

$$\begin{aligned}
\sigma_{\Delta T_{Side_HS}}^2 &= \left(\sigma_{TC04} \frac{\partial \Delta T_{Side_HS}}{\partial TC04} \right)^2 + \left(\sigma_{TC06} \frac{\partial \Delta T_{Side_HS}}{\partial TC06} \right)^2 + \left(\sigma_{TC09} \frac{\partial \Delta T_{Side_HS}}{\partial TC09} \right)^2 \\
&+ \left(\sigma_{TC10} \frac{\partial \Delta T_{Side_HS}}{\partial TC10} \right)^2 + \left(\sigma_{TC13} \frac{\partial \Delta T_{Side_HS}}{\partial TC13} \right)^2
\end{aligned}$$

$$\sigma_{\Delta T_{Side_HS}}^2 = \left(\sigma_{TC04} \left(\frac{1}{4} \right) \right)^2 + \left(\sigma_{TC06} \left(\frac{1}{4} \right) \right)^2 + \left(\sigma_{TC09} \left(\frac{1}{4} \right) \right)^2 + \left(\sigma_{TC10} \left(\frac{1}{4} \right) \right)^2 + \left(\sigma_{TC13} (-1) \right)^2$$

To estimate the thermal resistance of the bottom of the housing, $R_{t,Housing_Bottom}$, the following equation was used.

$$R_{t,Housing_Bottom} = 2 \frac{L_{FF}}{K_{FF} A_{HS_Bottom}} + \frac{L_{Bottom}}{K_{PC} A_{HS_Bottom}} + 3 \frac{1}{h_{c,Bottom} A_{HS_Bottom}}$$

Next, the uncertainty becomes,

$$\frac{\partial R_{t,Housing_Bottom}}{\partial L_{FF}} = 2 K_{FF}^{-1} A_{HS_Bottom}^{-1}$$

$$\frac{\partial R_{t,Housing_Bottom}}{\partial K_{FF}} = -2 L_{FF} K_{FF}^{-2} A_{HS_Bottom}^{-1}$$

$$\frac{\partial R_{t,Housing_Bottom}}{\partial A_{HS_Bottom}} = -A_{HS_Bottom}^{-2} (2 L_{FF} K_{FF}^{-1} + L_{Bottom} K_{PC}^{-1} + 3 h_{c,Bottom}^{-1})$$

$$\frac{\partial R_{t,Housing_Bottom}}{\partial L_{Bottom}} = K_{PC}^{-1} A_{HS_Bottom}^{-1}$$

$$\frac{\partial R_{t,Housing_Bottom}}{\partial K_{PC}} = -L_{Bottom} K_{PC}^{-2} A_{HS_Bottom}^{-1}$$

$$\frac{\partial R_{t,Housing_Bottom}}{\partial h_{c,Bottom}} = -3 h_{c,Bottom}^{-2} A_{HS_Bottom}^{-1}$$

$$\begin{aligned} \sigma_{R_{t,Housing_Bottom}}^2 &= \left(\sigma_{L_{FF}} \frac{\partial R_{t,Housing_Bottom}}{\partial L_{FF}} \right)^2 + \left(\sigma_{K_{FF}} \frac{\partial R_{t,Housing_Bottom}}{\partial K_{FF}} \right)^2 \\ &+ \left(\sigma_{A_{HS_Bottom}} \frac{\partial R_{t,Housing_Bottom}}{\partial A_{HS_Bottom}} \right)^2 + \left(\sigma_{L_{Bottom}} \frac{\partial R_{t,Housing_Bottom}}{\partial L_{Bottom}} \right)^2 \\ &+ \left(\sigma_{K_{PC}} \frac{\partial R_{t,Housing_Bottom}}{\partial K_{PC}} \right)^2 + \left(\sigma_{h_{c,Bottom}} \frac{\partial R_{t,Housing_Bottom}}{\partial h_{c,Bottom}} \right)^2 \end{aligned}$$

$$\begin{aligned}
\sigma_{R_{t,Housing_Bottom}}^2 &= \left(\sigma_{L_{FF}} (2K_{FF}^{-1} A_{HS_Bottom}^{-1}) \right)^2 + \left(\sigma_{K_{FF}} (-2L_{FF} K_{FF}^{-2} A_{HS_Bottom}^{-1}) \right)^2 \\
&+ \left(\sigma_{A_{HS_Bottom}} \left(-A_{HS_Bottom}^{-2} (2L_{FF} K_{FF}^{-1} + L_{Bottom} K_{PC}^{-1} \right. \right. \\
&\left. \left. + 3h_{c,Bottom}^{-1}) \right) \right)^2 + \left(\sigma_{L_{Bottom}} (K_{PC}^{-1} A_{HS_Bottom}^{-1}) \right)^2 \\
&+ \left(\sigma_{K_{PC}} (-L_{Bottom} K_{PC}^{-2} A_{HS_Bottom}^{-1}) \right)^2 \\
&+ \left(\sigma_{h_{c,Bottom}} (-3h_{c,Bottom}^{-2} A_{HS_Side}^{-1}) \right)^2
\end{aligned}$$

The calculation for the difference in temperature of the heat sink base and outside the housing bottom is as follows.

$$\Delta T_{Bottom_HS} = (T_{avg,Base} - TC15)$$

The uncertainty of this measurement was determined from the following equation.

$$\sigma_{\Delta T_{Bottom_HS}}^2 = \left(\sigma_{T_{avg,Base}} \frac{\partial \Delta T_{Bottom_HS}}{\partial T_{avg,Base}} \right)^2 + \left(\sigma_{TC15} \frac{\partial \Delta T_{Bottom_HS}}{\partial TC15} \right)^2$$

Since $\sigma_{T_{avg,Base}}$ has been previously calculated, the equation is simplified.

$$\sigma_{\Delta T_{Bottom_HS}}^2 = \left(\sigma_{T_{avg,Base}} (1) \right)^2 + \left(\sigma_{TC15} (-1) \right)^2$$

The next step was to compute the uncertainty of the losses from radiation. The calculation for $Q_{r,loss}$ is shown in the following equation.

$$Q_{r,loss} = N_{f_ch} Q_{1-2} + A_d \sigma \epsilon (T_s^4 - T_{amb}^4)$$

For simplicity this equation was broken into two parts; the front and rear profile radiation ($Q_{r,p}$) and radiation exchange between the surface of the heat sink channels and PC housing ($Q_{r,1-2}$).

$$Q_{r,loss} = Q_{r,1-2} + Q_{r,p}$$

The uncertainty of this measurement was determined from the following derivation.

$$\begin{aligned}
\sigma_{Q_{r,loss}}^2 &= \left(\sigma_{Q_{r,1-2}} \frac{\partial Q_{r,loss}}{\partial Q_{r,1-2}} \right)^2 + \left(\sigma_{Q_{r,p}} \frac{\partial Q_{r,loss}}{\partial Q_{r,p}} \right)^2 \\
\sigma_{Q_{r,loss}}^2 &= \left(\sigma_{Q_{r,1-2}} (1) \right)^2 + \left(\sigma_{Q_{r,p}} (1) \right)^2
\end{aligned}$$

The first uncertainty to be investigated was the profile radiation, $\sigma_{Q_{r,p}}$. The equation for $Q_{r,p}$ is as follows.

$$Q_{r,p} = 2A_p \sigma \varepsilon (T_s^4 - T_{amb}^4)$$

The variables in this equation are as follows.

- A_p = Surface area of heat sink profile
- ε = Emissivity of unfinished aluminum ~0.055 (0.04-0.07)
- σ = Stefan-Boltzmann Constant (no uncertainty)
- T_s = Average heat sink surface temperature
- T_{amb} = Average of air at inlet temperature.

The uncertainty of $Q_{r,p}$ was determined from the following derivation.

$$\frac{\partial Q_{r,p}}{\partial A_p} = 2\sigma \varepsilon (T_s^4 - T_{amb}^4);$$

$$\frac{\partial Q_{r,p}}{\partial \varepsilon} = 2A_p \sigma (T_s^4 - T_{amb}^4);$$

$$\frac{\partial Q_{r,p}}{\partial (T_s^4 - T_{amb}^4)} = 2A_p \sigma \varepsilon$$

$$\sigma_{Q_{r,p}}^2 = \left(\sigma_{A_p} \frac{\partial Q_{r,p}}{\partial A_p} \right)^2 + \left(\sigma_{\varepsilon} \frac{\partial Q_{r,p}}{\partial \varepsilon} \right)^2 + \left(\sigma_{(T_s^4 - T_{amb}^4)} \frac{\partial Q_{r,p}}{\partial (T_s^4 - T_{amb}^4)} \right)^2$$

$$\sigma_{Q_{r,p}}^2 = \left(\sigma_{A_p} (2\sigma \varepsilon (T_s^4 - T_{amb}^4)) \right)^2 + \left(\sigma_{\varepsilon} (2A_p \sigma (T_s^4 - T_{amb}^4)) \right)^2 + \left(\sigma_{(T_s^4 - T_{amb}^4)} (2A_p \sigma \varepsilon) \right)^2$$

From this equation, two uncertainties need to be further described, σ_{A_p} & $\sigma_{(T_s^4 - T_{amb}^4)}$.

First, A_p was found by a direct measurement with the model. Therefore, it was understood as having the same general tolerance applied to other manufactured parts, ± 0.02 in. Its total uncertainty was approximated by the following.

$$\sigma_{A_p}^2 = \left(\sigma_{B_{HS}} \frac{\partial A_p}{\partial H_{HS}} \right)^2 + \left(\sigma_{P_{wet}} \frac{\partial A_p}{\partial P_{wet}} \right)^2$$

$$\sigma_{B_{HS}} = \sigma_{P_{wet}} = 0.000508m$$

$$\sigma_{A_p}^2 = (0.00005(B_{HS}))^2 + (0.00005(P_{wet}))^2 = 2.25 \times 10^{-8} m^2$$

Secondly, the uncertainty $\sigma_{(T_s^4 - T_{amb}^4)}$ is found from the measurements for T_s and T_{amb} , which are the average temperatures of the heat sink surface and air at inlet, in K.

$$\sigma_{(T_s^4 - T_{amb}^4)} = \left(\sigma_{T_s} \left(\frac{\partial(T_s^4 - T_{amb}^4)}{\partial T_s} \right) \right)^2 + \left(\sigma_{T_{amb}} \left(\frac{\partial(T_s^4 - T_{amb}^4)}{\partial T_{amb}} \right) \right)^2$$

$$\sigma_{(T_s^4 - T_{amb}^4)} = \left(\sigma_{T_s} (4T_s^3) \right)^2 + \left(\sigma_{T_{amb}} (-4T_{amb}^3) \right)^2$$

Next the uncertainties, σ_{T_s} & $\sigma_{T_{amb}}$, needed to be individually determined.

The equation for T_s is as follows.

$$T_s = \frac{1}{2} \left(\frac{(TC03 + TC04 + TC05 + TC06 + TC07)}{5} + \frac{(TC09 + TC10)}{2} \right)$$

The uncertainty of this measurement was determined from the following derivation.

$$\frac{\partial T_s}{\partial TC09} = \frac{1}{4}; \quad \frac{\partial T_s}{\partial TC10} = \frac{1}{4}; \quad \frac{\partial T_s}{\partial TC03} = \frac{1}{10}; \quad \frac{\partial T_s}{\partial TC04} = \frac{1}{10};$$

$$\frac{\partial T_s}{\partial TC05} = \frac{1}{10}; \quad \frac{\partial T_s}{\partial TC06} = \frac{1}{10}; \quad \frac{\partial T_s}{\partial TC07} = \frac{1}{10}$$

$$\sigma_{T_s}^2 = \left(\sigma_{TC03} \frac{\partial T_s}{\partial TC03} \right)^2 + \left(\sigma_{TC04} \frac{\partial T_s}{\partial TC04} \right)^2 + \left(\sigma_{TC05} \frac{\partial T_s}{\partial TC05} \right)^2 + \left(\sigma_{TC06} \frac{\partial T_s}{\partial TC06} \right)^2$$

$$+ \left(\sigma_{TC07} \frac{\partial T_s}{\partial TC07} \right)^2 + \left(\sigma_{TC09} \frac{\partial T_s}{\partial TC09} \right)^2 + \left(\sigma_{TC10} \frac{\partial T_s}{\partial TC10} \right)^2$$

$$\sigma_{T_s}^2 = \left(\sigma_{TC03} \left(\frac{1}{10} \right) \right)^2 + \left(\sigma_{TC04} \left(\frac{1}{10} \right) \right)^2 + \left(\sigma_{TC05} \left(\frac{1}{10} \right) \right)^2 + \left(\sigma_{TC06} \left(\frac{1}{10} \right) \right)^2$$

$$+ \left(\sigma_{TC07} \left(\frac{1}{10} \right) \right)^2 + \left(\sigma_{TC09} \left(\frac{1}{4} \right) \right)^2 + \left(\sigma_{TC10} \left(\frac{1}{4} \right) \right)^2$$

The equation for T_{amb} is as follows.

$$T_{amb} = \frac{(TC01 + TC02)}{2}$$

The uncertainty of this measurement was determined from the following derivation.

$$\sigma_{T_{amb}}^2 = \left(\sigma_{TC01} \frac{\partial T_{amb}}{\partial TC01} \right)^2 + \left(\sigma_{TC02} \frac{\partial T_{amb}}{\partial TC02} \right)^2$$

$$\sigma_{T_{amb}}^2 = \left(\sigma_{TC01} \left(\frac{1}{2} \right) \right)^2 + \left(\sigma_{TC02} \left(\frac{1}{2} \right) \right)^2$$

Lastly, the uncertainty for the second term of the radiation losses was found through the following. The equation for estimating the radiation exchange between the heat sink channels and the PC housing is shown below.

$$Q_{r,1-2} = N_{f_ch} Q_{1-2}$$

Where the total radiation loss ($Q_{r,1-2}$) is a product of the loss for a single channel (Q_{1-2}) multiplied by the total number of channels, N_{f_ch} . N_{f_ch} is a constant value representing the total number of heat sink fin channels (5) and has no uncertainty. Therefore, the uncertainty for the total radiation loss from all the heat sink channels simplifies to the following equation.

$$\sigma_{Q_{r,s-s}}^2 = \left(\sigma_{Q_{1-2}}(5) \right)^2$$

$$\sigma_{Q_{r,s-s}} = 5\sigma_{Q_{1-2}}$$

The equation for Q_{1-2} is as follows.

$$Q_{1-2} = \frac{\sigma(T_1^4 - T_2^4)}{\frac{1 - \varepsilon_1}{\varepsilon_1 A_1} + \frac{1}{A_1 F_{1-2}} + \frac{1 - \varepsilon_2}{\varepsilon_2 A_2}}$$

It was desirable to break this equation up into two terms; the temperature difference between the two surfaces ($T_1^4 - T_2^4$), and the surface emissive resistance, R_s . The simplified equation for Q_{1-2} then becomes,

$$Q_{1-2} = \frac{\sigma(T_1^4 - T_2^4)}{R_s}$$

The uncertainty of this measurement was determined from the following derivation.

$$\sigma_{Q_{1-2}}^2 = \left(\sigma_{(T_1^4 - T_2^4)} \frac{\partial Q_{1-2}}{\partial (T_1^4 - T_2^4)} \right)^2 + \left(\sigma_{R_s} \frac{\partial Q_{1-2}}{\partial R_s} \right)^2$$

$$\sigma_{Q_{1-2}}^2 = \left(\sigma_{(T_1^4 - T_2^4)} (\sigma_{R_s}^{-1}) \right)^2 + \left(\sigma_{R_s} (-\sigma(T_1^4 - T_2^4) R_s^{-2}) \right)^2$$

Next the uncertainties $\sigma_{(T_1^4 - T_2^4)}$ and σ_{R_s} needed to be computed. The uncertainty $\sigma_{(T_1^4 - T_2^4)}$ is found from the following derivation.

$$\sigma_{(T_1^4 - T_2^4)} = \left(\sigma_{T_1} \left(\frac{\partial (T_1^4 - T_2^4)}{\partial T_1} \right) \right)^2 + \left(\sigma_{T_2} \left(\frac{\partial (T_1^4 - T_2^4)}{\partial T_2} \right) \right)^2$$

$$\sigma_{(T_1^4 - T_2^4)} = \left(\sigma_{T_1} (4T_1^3) \right)^2 + \left(\sigma_{T_2} (-4T_2^3) \right)^2$$

Since T_1 is the average heat sink surface temperature, its uncertainty (σ_{T_1}) has already been determined, $\sigma_{T_1} = \sigma_{T_s}$. The calculation for the uncertainty of the second surface, T_2 , still needed to be computed. T_2 was found from the following equation.

$$T_2 = \frac{1}{2} \left(\frac{(TC01 + TC02)}{2} + \frac{(TC11 + TC12 + TC16)}{3} \right)$$

The uncertainty of this measurement was determined from the following derivation.

$$\begin{aligned} \sigma_{T_2}^2 &= \left(\sigma_{TC01} \frac{\partial T_2}{\partial TC01} \right)^2 + \left(\sigma_{TC02} \frac{\partial T_2}{\partial TC02} \right)^2 + \left(\sigma_{TC11} \frac{\partial T_2}{\partial TC11} \right)^2 + \left(\sigma_{TC12} \frac{\partial T_2}{\partial TC12} \right)^2 + \left(\sigma_{TC16} \frac{\partial T_2}{\partial TC16} \right)^2 \\ \sigma_{T_2}^2 &= \left(\sigma_{TC01} \left(\frac{1}{4} \right) \right)^2 + \left(\sigma_{TC02} \left(\frac{1}{4} \right) \right)^2 + \left(\sigma_{TC11} \left(\frac{1}{6} \right) \right)^2 + \left(\sigma_{TC12} \left(\frac{1}{6} \right) \right)^2 + \left(\sigma_{TC16} \left(\frac{1}{6} \right) \right)^2 \end{aligned}$$

The surface emissive resistance was found through the following equation.

$$R_s = \frac{1 - \varepsilon_1}{\varepsilon_1 A_1} + \frac{1}{A_2} + \frac{1 - \varepsilon_2}{\varepsilon_2 A_2}$$

The uncertainty of this measurement was determined from the following derivation.

$$\begin{aligned} \frac{\partial R_s}{\partial \varepsilon_1} &= -\varepsilon_1^{-2} A_1^{-1}; & \frac{\partial R_s}{\partial A_1} &= A_1^{-2} (1 - \varepsilon_1^{-1}) \\ \frac{\partial R_s}{\partial \varepsilon_2} &= -\varepsilon_2^{-2} A_2^{-1}; & \frac{\partial R_s}{\partial A_2} &= A_2^{-2} (2 - \varepsilon_2^{-1}) \\ \sigma_{R_s}^2 &= \left(\sigma_{\varepsilon_1} \frac{\partial R_s}{\partial \varepsilon_1} \right)^2 + \left(\sigma_{A_1} \frac{\partial R_s}{\partial A_1} \right)^2 + \left(\sigma_{\varepsilon_2} \frac{\partial R_s}{\partial \varepsilon_2} \right)^2 + \left(\sigma_{A_2} \frac{\partial R_s}{\partial A_2} \right)^2 \\ \sigma_{R_s}^2 &= \left(\sigma_{\varepsilon_1} (-\varepsilon_1^{-2} A_1^{-1}) \right)^2 + \left(\sigma_{A_1} (A_1^{-2} (1 - \varepsilon_1^{-1})) \right)^2 \\ &+ \left(\sigma_{\varepsilon_2} (-\varepsilon_2^{-2} A_2^{-1}) \right)^2 + \left(\sigma_{A_2} (A_2^{-2} (2 - \varepsilon_2^{-1})) \right)^2 \end{aligned}$$

Using the same concept for using a general tolerance of $\pm 0.02''$ to all physical dimensions the following uncertainties, σ_{A_1} and σ_{A_2} were found from the following calculation.

$$\begin{aligned} \sigma_{A_1}^2 &= (0.00005(W_{HS}))^2 + \left(0.00005 \left(\frac{P_{wet}}{5} \right) \right)^2 = 2.67 \times 10^{-9} m^2 \\ \sigma_{A_2}^2 &= (0.00005(W_{HS}))^2 + (0.00005(b))^2 = 2.68 \times 10^{-9} m^2 \end{aligned}$$

- **Pressure Drop**

The pressure loss across the heat sink was represented in the non-dimensional form as the pressure loss coefficient, η . This measurement was determined from the following equation.

$$\eta = \frac{\Delta p_{Stc}}{\left(\frac{1}{2}\rho U_{HS}^2\right)}$$

The uncertainty of this measurement was determined from the following derivation.

$$\begin{aligned}\frac{\partial \eta}{\partial \Delta p_{Stc}} &= 2 \times \rho^{-1} \times U_{HS}^{-2} \\ \frac{\partial \eta}{\partial \rho} &= -2 \times C \Delta p_{Stc} \times \rho^{-2} \times U_{HS}^{-2} \\ \frac{\partial \eta}{\partial U_{HS}} &= -4 \times C \Delta p_{Stc} \times \rho^{-1} \times U_{HS}^{-3} \\ \sigma_{\eta}^2 &= \left(\sigma_{\Delta p_{Stc}} \frac{\partial \eta}{\partial \Delta p_{Stc}}\right)^2 + \left(\sigma_{\rho} \frac{\partial \eta}{\partial \rho}\right)^2 + \left(\sigma_{U_{HS}} \frac{\partial \eta}{\partial U_{HS}}\right)^2 \\ \sigma_{\eta}^2 &= \left(\sigma_{\Delta p_{Stc}} (2 \times \rho^{-1} \times U_{HS}^{-2})\right)^2 + \left(\sigma_{\rho} (-2 \times C \Delta p_{Stc} \times \rho^{-2} \times U_{HS}^{-2})\right)^2 \\ &\quad + \left(\sigma_{U_{HS}} (-4 \times C \Delta p_{Stc} \times \rho^{-1} \times U_{HS}^{-3})\right)^2\end{aligned}$$

The three variables in this derivation are Δp_{Stc} , ρ & U_{HS} . Each of these have propagated uncertainties that will need to be derived, with the exception of Δp_{Stc} . Δp_{Stc} is the measurement for the static pressure difference across the heat sink. It only needed to be multiplied by a conversion factor ($C = 248.84$ Pa/inH2O) to convert it from inH2O to Pa. The other uncertainties, ρ & U_{HS} were then found.

The air density (ρ) was calculated through the following equation.

$$\rho = \frac{cp_{abs}}{\mathcal{R}T_{amb}}$$

where, \mathcal{R} is the gas constant for air and contributes no uncertainty. However, P_{abs} & T_{amb} are measurements and do have added uncertainty. The uncertainty of ρ was determined from the following derivation.

$$\begin{aligned}\frac{\partial \rho}{\partial p_{abs}} &= c \times \mathcal{R}^{-1} \times T_{amb}^{-1} \\ \frac{\partial \rho}{\partial T_{amb}} &= -cp_{abs} \times \mathcal{R}^{-1} \times T_{amb}^{-2}\end{aligned}$$

$$\sigma_{\rho}^2 = \left(\sigma_{p_{abs}} \frac{\partial \rho}{\partial p_{abs}} \right)^2 + \left(\sigma_{T_{amb}} \frac{\partial \rho}{\partial T_{amb}} \right)^2$$

$$\sigma_{\rho}^2 = \left(\sigma_{p_{abs}} (c \times \mathcal{R}^{-1} \times T_{amb}^{-1}) \right)^2 + \left(\sigma_{T_{amb}} (-c p_{abs} \times \mathcal{R}^{-1} \times T_{amb}^{-2}) \right)^2$$

In this derivation, c is the conversion from PSI to Pa ($c = 6894.757 \text{ Pa/PSI}$).

The uncertainty for T_{amb} has been previously computed during the radiation loss uncertainty derivation. $\sigma_{p_{abs}}$ was found from the calibration of the absolute sensor.

The next step was to find the uncertainty of the heat sink velocity. The equation for measuring the heat sink air velocity is shown below.

$$U_{HS} = \frac{A_{Duct}}{A_{HS}} \sqrt{\frac{2Cp_{Dyc}}{\rho}}$$

The uncertainty of this measurement was determined from the following derivation.

$$\frac{\partial U_{HS}}{\partial p_{Dyc}} = \frac{\sqrt{2}}{2} \frac{1}{C} p_{Dyc}^{-1/2} \rho^{-1/2} \frac{A_{Duct}}{A_{HS}}$$

$$\frac{\partial U_{HS}}{\partial \rho} = -\frac{\sqrt{2}}{2} C p_{Dyc}^{1/2} \rho^{-3/2} \frac{A_{Duct}}{A_{HS}}$$

$$\frac{\partial U_{HS}}{\partial A_{Duct}} = \sqrt{2} C p_{Dyc}^{1/2} \rho^{-1/2} A_{HS}^{-1}$$

$$\frac{\partial U_{HS}}{\partial A_{HS}} = -\sqrt{2} C p_{Dyc}^{1/2} \rho^{-1/2} A_{Duct}^1 A_{HS}^{-2}$$

$$\sigma_{U_{HS}}^2 = \left(\sigma_{p_{Dyc}} \frac{\partial U_{HS}}{\partial p_{Dyc}} \right)^2 + \left(\sigma_{\rho} \frac{\partial U_{HS}}{\partial \rho} \right)^2 + \left(\sigma_{A_{Duct}} \frac{\partial U_{HS}}{\partial A_{Duct}} \right)^2 + \left(\sigma_{A_{HS}} \frac{\partial U_{HS}}{\partial A_{HS}} \right)^2$$

$$\sigma_{U_{HS}}^2 = \left(\sigma_{p_{Dyc}} \left(\frac{\sqrt{2}}{2} (C p_{Dyc})^{-1/2} \rho^{-1/2} \frac{A_{Duct}}{A_{HS}} \right) \right)^2 + \left(\sigma_{\rho} \left(-\frac{\sqrt{2}}{2} (C p_{Dyc})^{1/2} \rho^{-3/2} \frac{A_{Duct}}{A_{HS}} \right) \right)^2 +$$

$$\left(\sigma_{A_{Duct}} \left(\sqrt{2} (C p_{Dyc})^{\frac{1}{2}} \rho^{-\frac{1}{2}} A_{HS}^{-1} \right) \right)^2 + \left(\sigma_{A_{HS}} \left(-\sqrt{2} (C p_{Dyc})^{\frac{1}{2}} \rho^{-\frac{1}{2}} A_{Duct}^1 A_{HS}^{-2} \right) \right)^2$$

The remaining uncertainties from this equation are $\sigma_{A_{Duct}}$ & $\sigma_{A_{HS}}$. Using the same approach as previously outlined, the uncertainties for these two measurements is shown below.

$$\sigma_{A_{Duct}}^2 = (0.00005(0.05m))^2 + (0.00005(0.05m))^2 = 1.29 \times 10^{-9} m^2$$

$$\sigma_{A_{HS}}^2 = ((5) \times 0.00005(b))^2 + ((5) \times 0.00005(L))^2 = 4.03 \times 10^{-9} m^2$$

- **Reynolds Number**

The last uncertainty needing computation was that of the Reynolds number. Both the Nusselt number and pressure loss coefficient are dependent on Reynolds number. Because the Reynolds number was not an independent variable its uncertainty was not needed when computing the error of the experiment. However, it was computed for reference.

The equation for the Reynolds number within a heat sink channel is as follows.

$$Re_{HS} = \frac{\rho \times U_{HS} \times D_{H_HS}}{\mu}$$

The uncertainty of this measurement was determined from the following derivation.

$$\begin{aligned}\frac{\partial Re_{HS}}{\partial \rho} &= U_{HS} \times D_{H_HS} \times \mu^{-1} \\ \frac{\partial Re_{HS}}{\partial U_{HS}} &= \rho \times D_{H_HS} \times \mu^{-1} \\ \frac{\partial Re_{HS}}{\partial D_{H_HS}} &= \rho \times U_{HS} \times \mu^{-1} \\ \sigma_{Re_{HS}}^2 &= \left(\sigma_{\rho} \frac{\partial Re_{HS}}{\partial \rho} \right)^2 + \left(\sigma_{U_{HS}} \frac{\partial Re_{HS}}{\partial U_{HS}} \right)^2 + \left(\sigma_{D_{H_HS}} \frac{\partial Re_{HS}}{\partial D_{H_HS}} \right)^2 \\ \sigma_{Re_{HS}}^2 &= \left(\sigma_{\rho} (U_{HS} \times D_{H_HS} \times \mu^{-1}) \right)^2 + \left(\sigma_{U_{HS}} (\rho \times D_{H_HS} \times \mu^{-1}) \right)^2 + \left(\sigma_{D_{H_HS}} (\rho \times U_{HS} \times \mu^{-1}) \right)^2\end{aligned}$$

Of the four uncertainties in this derivation, σ_{ρ} , $\sigma_{U_{HS}}$, $\sigma_{D_{H_HS}}$ & σ_{μ} ; two have been found previously, while the uncertainties of the D_{H_HS} and μ still need to be found. The dynamic viscosity, μ , was determined from the thermo-physical properties of air. For this reason it was constant and considered to have no uncertainty. The equation for the hydraulic diameter of the heat sink channel is shown below.

$$D_{H_HS} = \frac{4 \times A_{HS_Ch}}{P_{wet}}$$

The uncertainty of this measurement was determined from the following derivation.

$$\begin{aligned}\frac{\partial D_{H_HS}}{\partial A_{HS_Ch}} &= 4 \times P_{wet}^{-1} \\ \frac{\partial D_{H_HS}}{\partial P_{wet}} &= -4 \times A_{HS_Ch} \times P_{wet}^{-2} \\ \sigma_{D_{H_HS}}^2 &= \left(\sigma_{A_{HS_Ch}} (4 \times P_{wet}^{-1}) \right)^2 + \left(\sigma_{P_{wet}} (-4 \times A_{HS_Ch} \times P_{wet}^{-2}) \right)^2\end{aligned}$$

The uncertainty of the heat sink wetted area, A_{HS} , has already been derived, but needed to be modified so that it would apply to a single channel, shown below.

$$\sigma_{A_{HS_Ch}}^2 = (0.00005(b))^2 + (0.00005(L))^2 = 1.61 \times 10^{-10} m^2$$

The last uncertainty is for the wetted perimeter of the heat sink. This was simply the perimeter of a single heat sink channel. The equation for P_{wet} is shown below.

$$P_{wet} = 2L + 2b$$

By using the same principal of applying a general tolerance to its dimensions the following uncertainty were derived.

$$\sigma_{P_{wet}}^2 = \left(\sigma_L \frac{\partial P_{wet}}{\partial L} \right)^2 + \left(\sigma_b \frac{\partial P_{wet}}{\partial b} \right)^2$$

$$\sigma_{P_{wet}}^2 = (0.00005(2))^2 + (0.00005(2))^2 = 1.41 \times 10^{-4} m$$

- Results

Table H - 2 Experimental Results and Uncertainty

Testing Parameters			Experimental Results and Uncertainties					
Target Chamber Pressure (atm)	Target Flow (% of Max)	Heater Set point (W)	Heat Sink Reynolds Number Re	Uncertainty of the Reynolds Number (\pm)	Average Nusselt Number	Uncertainty of the Nusselt Number (\pm)	Pressure Loss Coefficient	Uncertainty of the Loss Coefficient (\pm)
			Re _D	$\pm\sigma_{Re}$	Nu	$\pm\sigma_{Nu}$	η	$\pm\sigma_{\eta}$
0.1	100%	20	1223	97	349.8	21.1	2.043	0.025
0.1	90%	20	1072	85	335.7	21.3	2.164	0.031
0.1	75%	20	872	69	302.8	19.9	2.424	0.046
0.1	60%	20	709	56	284.6	18.9	2.731	0.071
0.1	45%	20	472	37	243.6	18.4	3.561	0.150
0.2	100%	20	2815	222	571.1	29.6	1.528	0.009
0.2	80%	20	2193	173	489.7	25.6	1.663	0.014
0.2	60%	20	1636	129	410.8	22.0	1.854	0.025
0.2	40%	20	1053	83	333.3	19.3	2.141	0.060
0.2	30%	20	759	60	294.5	18.7	2.712	0.115
0.3	100%	20	4226	334	734.9	33.5	1.282	0.006
0.3	80%	20	3349	264	598.1	26.9	1.406	0.009
0.3	60%	20	2490	197	506.2	23.2	1.540	0.016
0.3	40%	20	1603	127	396.1	18.9	1.808	0.039
0.3	20%	20	756	60	296.5	16.9	3.878	0.187
0.4	90%	40	6185	488	955.4	30.4	1.202	0.004
0.4	80%	40	5255	415	833.8	26.0	1.218	0.005
0.4	60%	20	4001	316	627.7	22.9	1.312	0.009
0.4	40%	20	2647	209	522.6	24.6	1.529	0.021
0.4	20%	20	1186	94	329.1	19.4	1.937	0.096
0.5	80%	40	7210	569	1063.5	33.1	1.179	0.004
0.5	60%	20	5465	431	808.9	31.5	1.191	0.006
0.5	40%	20	3619	286	645.3	28.8	1.331	0.013
0.5	20%	20	1742	138	419.4	21.3	1.719	0.054
0.6	100%	40	8651	683	1205.0	40.7	1.155	0.003
0.6	80%	40	6950	549	1015.2	34.9	1.177	0.005
0.6	60%	40	5216	412	810.0	28.8	1.212	0.008
0.6	40%	20	3402	269	570.0	25.7	1.353	0.019
0.6	20%	20	1646	130	412.8	25.8	1.803	0.080
0.7	100%	40	9742	769	1315.9	46.2	1.139	0.003
0.7	80%	40	7805	616	1098.1	38.2	1.164	0.004
0.7	60%	40	5855	462	892.4	31.4	1.193	0.008

0.7	40%	40	3849	304	666.4	26.8	1.330	0.017
0.7	20%	20	1871	148	427.2	26.9	1.649	0.071
0.8	100%	40	10985	867	1434.3	50.6	1.127	0.003
0.8	80%	40	8746	691	1188.4	39.8	1.156	0.004
0.8	60%	40	6529	515	974.3	32.6	1.190	0.007
0.8	40%	40	4335	342	741.7	29.1	1.289	0.015
0.8	20%	40	2129	168	456.9	24.6	1.722	0.062
0.9	100%	40	11976	945	1469.1	51.5	1.115	0.003
0.9	80%	40	9569	755	1231.7	41.0	1.138	0.004
0.9	60%	40	7160	565	1010.7	32.9	1.164	0.007
0.9	40%	40	4783	378	775.3	27.1	1.232	0.014
0.9	20%	40	2311	182	480.2	25.3	1.634	0.060
1.0	100%	40	13930	1100	1638.7	48.5	1.110	0.002
1.0	80%	40	11369	898	1397.6	43.4	1.121	0.003
1.0	60%	40	8526	673	1160.6	36.3	1.152	0.005
1.0	40%	40	5699	450	890.7	30.2	1.192	0.011
1.0	30%	40	3464	274	644.2	22.2	1.440	0.028
1.0	20%	40	2741	216	536.8	26.7	1.557	0.045